National Library of Canada | Bibliothèque nationale du Canada | CANADIAN THESES ON MICROFICHE | THÈSES CANADIENNES SUR MICROFICHE

NAME OF AUTHOR/*NOM DE L'AUTEUR* Jeff UI

TITLE OF THESIS/*TITRE DE LA THÈSE* Generation of Second Harmonic Radiation at Mercury Surfaces

UNIVERSITY/*UNIVERSITÉ* Simon Fraser University

DEGREE FOR WHICH THESIS WAS PRESENTED/ *GRADE POUR LEQUEL CETTE THÈSE FUT PRÉSENTÉE* M.Sc.

YEAR THIS DEGREE CONFERRED/*ANNÉE D'OBTENTION DE CE GRADE* ~~1977~~ 1978

NAME OF SUPERVISOR/*NOM DU DIRECTEUR DE THÈSE* Dr. E. D. Crozier

Permission is hereby granted to the NATIONAL LIBRARY OF CANADA to microfilm this thesis and to lend or sell copies of the film.

The author reserves other publication rights, and neither the thesis nor extensive extracts from it may be printed or otherwise reproduced without the author's written permission.

L'autorisation est, par la présente, accordée à la BIBLIOTHÈQUE NATIONALE DU CANADA de microfilmer cette thèse et de prêter ou de vendre des exemplaires du film.

L'auteur se réserve les autres droits de publication; ni la thèse ni de longs extraits de celle-ci ne doivent être imprimés ou autrement reproduits sans l'autorisation écrite de l'auteur.

DATED/*DATÉ* April 24, 1978 SIGNED/*SIGNÉ*

PERMANENT ADDRESS/*RÉSIDENCE FIXÉ* [redacted]

NL-91 (3-74)

NOTICE

The quality of this microfiche is heavily dependent upon the quality of the original thesis submitted for microfilming. Every effort has been made to ensure the highest quality of reproduction possible.

If pages are missing, contact the university which granted the degree.

Some pages may have indistinct print especially if the original pages were typed with a poor typewriter ribbon or if the university sent us a poor photocopy.

Previously copyrighted materials (journal articles, published tests, etc.) are not filmed.

Reproduction in full or in part of this film is governed by the Canadian Copyright Act, R.S.C. 1970, c. C-30. Please read the authorization forms which accompany this thesis.

THIS DISSERTATION
HAS BEEN MICROFILMED
EXACTLY AS RECEIVED

AVIS

La qualité de cette microfiche dépend grandement de la qualité de la thèse soumise au microfilmage. Nous avons tout fait pour assurer une qualité supérieure de reproduction.

S'il manque des pages, veuillez communiquer avec l'université qui a conféré le grade.

La qualité d'impression de certaines pages peut laisser à désirer, surtout si les pages originales ont été dactylographiées à l'aide d'un ruban usé ou si l'université nous a fait parvenir une photocopie de mauvaise qualité.

Les documents qui font déjà l'objet d'un droit d'auteur (articles de revue, examens publiés, etc.) ne sont pas microfilmés.

La reproduction, même partielle, de ce microfilm est soumise à la Loi canadienne sur le droit d'auteur, SRC 1970, c. C-30. Veuillez prendre connaissance des formules d'autorisation qui accompagnent cette thèse.

LA THÈSE A ÉTÉ
MICROFILMÉE TELLE QUE
NOUS L'AVONS REÇUE

SECOND HARMONIC GENERATION BY REFLECTION FROM MERCURY SURFACES

by

Tsukasa Jeff Ui

B.Sc., University of British Columbia, 1973

A THESIS SUBMITTED IN PARTIAL FULFILLMENT OF

THE REQUIREMENTS FOR THE DEGREE OF

MASTER OF SCIENCE

in the Department

of

Physics

SIMON FRASER UNIVERSITY

April 1978

APPROVAL

Name: Tsukasa Jeff Ui

Degree: Master of Science

Title of Thesis: Second Harmonic Generation By Reflection From Hg Surfaces.

Examining Committee:

Chairman: Dr. S. Gygax

Dr. E.D. Crozier
Senior Supervisor

Dr. K.E. Rieckhoff

Dr. R.H. Enns

Dr. J.C. Irwin

Date Approved: 3/4/78

PARTIAL COPYRIGHT LICENSE

I hereby grant to Simon Fraser University the right to lend my thesis or dissertation (the title of which is shown below) to users of the Simon Fraser University Library, and to make partial or single copies only for such users or in response to a request from the library of any other university, or other educational institution, on its own behalf or for one of its users. I further agree that permission for multiple copying of this thesis for scholarly purposes may be granted by me or the Dean of Graduate Studies. It is understood that copying or publication of this thesis for financial gain shall not be allowed without my written permission.

Title of Thesis/Dissertation:

Generation of Second Harmonic Radiation at Mercury Surfaces

Author:

(signature)

Jeff Ui

(name)

April 24, 1978

(date)

ABSTRACT

Linear optical measurements, ellipsometry and reflectivity, have yielded different dielectric constants for liquid Hg. It was suggested by Crozier and Murphy that dielectric constants derived from ellipsometry and reflectivity measurements need not be the same since the methods measure different quantities. The results of Crozier and Murphy were shown to be consistent with the existence of a surface transition layer first proposed by Bloch and Rice.

Second Harmonic Generation (SHG) has been demonstrated to be an useful method for investigating surface effects.

This thesis deals with the SHG investigation of Hg as a function of temperature, angle of incidence, and polarization states of the incident and reflected radiation in the solid and liquid states. The Hg was maintained in an ultrahigh vacuum to minimize surface adsorption of gases.

Due to the extremely low conversion efficiency $\sim 10^{-15}$ obtained by previous investigators of SHG from Ag, a high power passively Q switched and mode

locked Nd glass laser was used as the light source. High gain photomultipliers were used as second harmonic light detectors. The detection system was first tested by generating second harmonic radiation from an Ag surface.

At angles of incidence θ from 60° to 74° and at temperatures between $26^{\circ}C$ and $-131^{\circ}C$, the radiation detected from Hg was found to be dominated by background radiation of broad spectral width. No radiation was detected from liquid Hg surfaces at $\theta=76^{\circ}$ and 78°.

Second harmonic radiation was detected from solid Hg surfaces at $\theta=76^{\circ}$ and 78°. In agreement with SHG theory, at $\theta=76^{\circ}$, I_s, the s component of the second harmonic radiation was less than I_p, the p component for incident beams polarized at $\phi= 0^{\circ}$ and 45° with respect to the plane of incidence. No second harmonic radiation was detected for an incident beam with $\phi= 90^{\circ}$. At $\theta= 78^{\circ}$, I_s was less than I_p when the incident beam was polarized in the plane of incidence. However, contrary to theory, I_s was greater than I_p for incident beams polarized at 45° and 90° with respect to the plane of incidence.

In comparing experiment with theory, two models

of solid Hg were considered. Firstly, the surface and bulk properties were assumed to be described by the reflectivity dielectric constants of solid Hg. Secondly, solid Hg was assumed to consist of a thin surface layer of high conductivity with the bulk having lower conductivity. The use of these models in conjunction with the SHG theory of Rudnick and Stern gave values of I_s/I_p which were several orders of magnitude smaller than the experimentally observed ratios.

From the viewpoint of the main objective of this thesis, the non-observance of second harmonic radiation from liquid Hg was disappointing. The simple model calculations performed for solid Hg may offer a partial explanation. There was a decrease in the total second harmonic intensity for a two layer model when compared with a case without a transition zone. Thus second harmonic radiation would not be experimentally detectable from liquid Hg.

The results of this thesis provide no clarification of the optical response of liquid and solid Hg. The abrupt change in I_s/I_p between $\theta = 76^o$ and 78^o for solid Hg is unexplained and needs further experimental work.

He who is self approving does not shine. He who boasts has no merit. He who exalts himself does not rise high. Judged according to Tao, he is like the remnants of food or a tumor on the body, an object of universal disgust. Therefore one who has Tao will not consort with such persons.

LAO TZU 604 B.C.

It is easy to convince a wise man, but to reason with a fool is a difficult undertaking.

CHINESE PROVERB

Spread out your knowledge and it shall be found shallow.

* * *

The perfect man ignores self.
The divine man ignores wealth.
The true sage ignores reputation.

CHUANG TZU 400 B.C.

When you see a good man, think of emulating him. When you see a bad man, examine your own heart.

CHINESE PROVERB

A learned man once asked a Zen teacher to instruct him. The teacher began to talk, but the learned man persisted in interrupting him, "Oh, yes, I know that already," and "That is of course a part of many philosophies."

At last the Zen master stopped talking and prepared to serve the learned man tea. He filled up his cup and then kept on pouring until it overflowed. "Enough," exclaimed the learned man. "My cup is already full."

"Indeed, so I see," said the teacher. "And if you do not empty your cup first, how can you expect to taste my tea?"

ANCIENT ZEN STORY

"The usefulness of the cup is its emptiness."

BRUCE LEE

Abide by the principle.
Dissolve the principle.
Obey the principle
Without being bound to it.

BRUCE LEE

Young Man.
Seize every minute
Of your time.
The days fly by;
Ere long you too
Will grow old.

TZU YEH

There were three words which
the Master barred from use.
He would have no "shall's,"
no "must's," and certainly
no "I's."

CHINESE PROVERB

ACKNOWLEDGEMENTS

I wish to express my gratitude to Dr. E. D. Crozier for his guidance and financial support throughout the duration of this project.

Grant Sheffer's assistance during the initial stages of research is greatly appreciated.

Many thanks are in order for Rom Federici, Mike Billany, Jim Oxton, Wayne Sievers, the Electronics shop, the Machine shop, and the Glassblowing shop.

I also wish to thank Dr. J. C. Irwin and Tom McMath for the use of their Tektronix 555 oscilloscope.

Thank you, Mie for typing a part of the manuscript.

Thank you, Mom, Dad, and Wai Ching, for your moral support.

TABLE OF CONTENTS

LIST OF TABLES

LIST OF FIGURES

CHAPTER 1

INTRODUCTION

In studies of the optical properties of metals, linear methods recognize the existence of a surface transition zone. Techniques involving transmission of light attempt to bypass the existence of the zone, whereas in ellipsometry and reflectivity measurements, the zone is ignored. The bulk optical constants are assumed to represent the response of solids or liquids in the absence of a surface transition zone.[1] However, evidence exists, particularly in the case of Hg, that optical properties can be influenced by surface effects.

Hg, being the only pure metal to exist in the liquid state at room temperature, has been the subject of many experiments. Linear optical measurements, ellipsometry and reflectivity, have yielded seemingly contradicting results.[2,3] Dielectric constants derived from reflectivity measurements at near normal incidence were found to be closely predicted by the Nearly Free Electron Drude model. Ellipsometry and reflectivity results at oblique angles of incidence on the other hand showed non-Drude behaviour.[4,5] In the extraction of dielectric

constants from the experimental data, the Hg surface was assumed to be a mathematical plane, where the transition to bulk occurred over a distance negligibly small compared with the wavelength of the probing radiation.

Crozier and Murphy[5] suggested that dielectric constants derived from ellipsometry and reflectivity need not be the same since the two methods measure different quantities. In the interaction of electromagnetic waves with a metal, the complex reflection amplitudes are represented by, $r_p = |r_p| e^{i\delta_p}$ and $r_s = |r_s| e^{i\delta_s}$, which define the amplitude and phase change of the reflected wave relative to the incident wave. The subscripts p and s denote field components parallel and perpendicular to the plane of incidence, respectively. Two quantities ρ the ratio of the reflection amplitudes $|r_p|/|r_s|$, and Δ the relative phase change on reflection $\delta_p - \delta_s$ are measured in ellipsometry at each wavelength at a fixed oblique angle of incidence. In the reflectivity measurements of Wilson and Rice,[2] the absolute reflected intensity was measured over the widest possible wavelength range at near normal incidence. The phase change δ was extracted through the use of a Kramers-Kronig dispersion

relation. The ellipsometry and reflectivity measurements of Crozier and Murphy made over the wavelength range 2500 $\mathring{A}$ to 7500 $\mathring{A}$ for the same samples at an angle of incidence 70° were found to be consistent with the existence of a surface transition layer first proposed by Bloch and Rice.[4] It was concluded by Crozier and Murphy that the contradictory results arise because ellipsometry samples the response of Hg to $\underline{E}$ fields both parallel and perpendicular to the surface, whereas reflectivity measurements at near normal incidence examine the response of Hg to $\underline{E}$ fields that are essentially parallel to the surface. If the conductivity parallel to the surface is different from the conductivity perpendicular to the surface, then the deduced dielectric constants need not be the same.

The BR (Bloch and Rice) model is an Epstein profile, introduced by Epstein in a study of the reflection of radio waves from the ionosphere. It is a phenomenological model with which variations of the conductivity as a function of distance into the sample can be approximated by adjusting five

parameters. The actual number of parameters can be greater depending on the version of the BR model used. At a slight distance into the substance, the conductivity reaches a peak value before assuming the bulk value. Qualitative arguments have been given for the enhanced conductivity based on the contracting effect of surface tension.[4] Bloch and Rice obtained the best agreement with data from linear experiments with the peak occurring 0.1 Å into the substance and with the peak conductivity being twelve times that of the bulk value. The effective width of the transition zone, full width at half maximum was ~ 4 A. One of the profiles used in fitting the ellipsometry/reflectivity data is shown in FIG. 1.[5] The imaginary part ε_2 of the dielectric constant is plotted as a function of the distance into the medium for a fixed frequency in the visible spectrum.

Investigations of surface plasmon dispersion in liquid Hg support the existence of a peak in the conductivity. Guidotti and Rice[6] proposed a modified model in which a larger conductivity existed parallel to the surface than normal to the surface, in agreement with Crozier and Murphy.

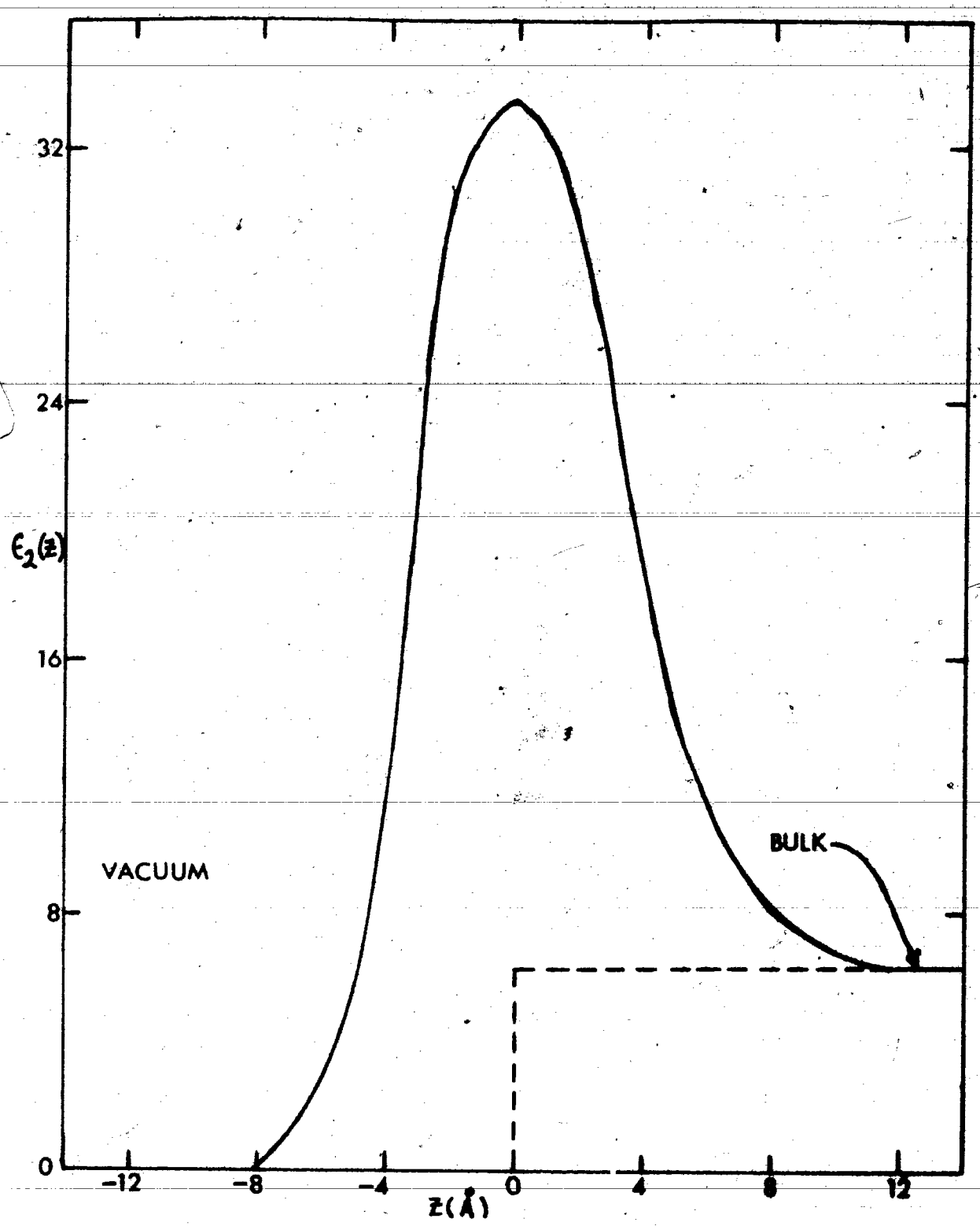

FIG. 1 A plot of the imaginary part of the dielectric constant ϵ_2 vs Z. The dielectric constant can be written as $\epsilon = \epsilon_1 + \epsilon_2$. Z= 0 represents the mathematical boundary of the substance.

In their model, the magnitude of the peak is comparable to the conductivity of polycrystalline Hg. The dc conductivity of solid Hg is 3.7 to 5.0 times that for liquid Hg.[7] The results of GR (Guidotti and Rice) suggest that the outermost two or three atomic layers are more ordered than they would be in the bulk liquid. According to GR, a decrease in the effective mass of the electrons due to band structure effects rather than an increase in electron density may lead to the peak in the conductivity.

There is another method whereby the transition zone can be probed. The SH (second harmonic) radiation generated by reflection from a metal surface is theoretically sensitive to currents induced in the surface by the high amplitude EM fields provided by pulsed lasers. The advent of pulsed lasers with peak output power densities of the order 10^9 W/cm^2 from which $\underline{E}$ fields of the order 10^6 V/cm. are available, has made possible the study of Non Linear Optics, of which SHG (second harmonic generation) is a branch, which deals with terms of second order and higher of the current density $\underline{J}$. Experimentally, the SHG efficiency $|E(2\omega)|^2/|E(\omega)|^2$ from Ag was found to be $\sim 10^{-15}$ when a Q switched ruby laser with

a peak output power 10^6 W was used as the light source[8]. Therefore high amplitude $\underline{E}$ fields are necessary in the probing radiation for SHG to be detected.

An SHG investigation of Hg at 2×10^{-6} torr. was reported earlier by Crozier, Ninnis and Rieckhoff[9], but no definitive statement was made regarding the transition region. At 1×10^{-6} torr., a monolayer of impurities is formed on a surface in ~ 2 seconds. Experiments have shown that SHG is sensitive to surface contamination. Brown and Matsuoka[10] found the SHG efficiency from an Ag surface maintained at 2×10^{-7} torr. to be 4 times greater than the SHG efficiency from an Ag surface maintained at 5×10^{-4} torr., whereas McCardell[11] found the SHG efficiency to be greater from contaminated surfaces than from freshly evaporated Ag surfaces maintained at ~ 10^{-10} torr.

The nature of the transition layer in Hg, requires further study. A technique such as SHG which is extremely sensitive to surface conditions may prove useful in further defining the surface layer and in determining whether for Hg, the layer is a product of surface contamination.

In this thesis, studies of SHG from Hg maintained at ~ 10^{-10} torr. were done as a function of temperature, angle of incidence, and polarization states of the incident and reflected radiation. Following this chapter, several theories of SHG are discussed. In chapter 3, the apparatus is described. Experiments performed in examining the performance characteristics of the Nd glass laser and the electronic detection system, as well as the results of SHG from Ag and Hg are presented in chapter 4.

The results for Ag and Hg are interpreted in chapter 5. The mechanism by which the larger than predicted second harmonic signals polarized perpendicular to the plane of incidence are generated from Ag and solid Hg surfaces, is not known. From liquid Hg surfaces, second harmonic signals could not be distinguished from the background radiation. The inclusion of a surface transition layer for solid Hg in the theoretical calculations failed to account for the large second harmonic signal polarized perpendicular to the plane of incidence.

CHAPTER 2

THEORY

2-1 INTRODUCTION

In section 2-2, a classical hydrodynamical derivation of the second harmonic currend density $\underline{J}(2\omega)$ from which the second harmonic $\underline{E}$ fields can be calculated, is presented.

A long wavelength theory such as the classical hydrodynamical theory, in which the EM fields are considered to be slowly varying with respect to the distance an electron travels in the time $1/\omega$, is approximate when applied to second harmonic generation from metal surfaces. The normal component of $\underline{E}$ is discontinuous across the boundary and changes from the value outside the medium to the value inside in a very short distance. The second harmonic generation theory of Rudnick and Stern in which non-local effects are included by using a wavenumber dependent dielectric constant in the integrals for the second harmonic $\underline{E}$ fields is discussed in section 2-3.

Finally, in section 2-4, the second harmonic radiation is shown to come off the sample surface at the specular angle.

2-2 CLASSICAL HYDRODYNAMICAL THEORY

Early theories of second harmonic generation were long wavelength approximations where the EM fields were assumed to be slowly varying with respect to the distance an electron travels during the time $1/\omega$.[12, 13, 14]

In the classical hydrodynamical theory, the nonlinear response of an electron gas is described by the hydrodynamical equation of motion for an average velocity $\underline{V}$,[14, 15]

$$\frac{\partial \underline{V}}{\partial t} + (\underline{V} \cdot \nabla \underline{V}) = e/m \quad (\underline{E} + \underline{V}/c \times \underline{H}) \qquad (2.1)$$

and the equation of continuity for a number density n of the electrons.

$$\frac{\partial n}{\partial t} + \nabla \cdot (n\underline{v}) = 0 \qquad (2.2)$$

The fields $\underline{E}$ and $\underline{H}$ are connected with $\underline{V}$ and n through the Maxwell equations

$$\nabla \cdot E = 4\pi\rho \qquad \text{and} \qquad \nabla \times \underline{H} - \frac{1}{c}\frac{\partial \underline{E}}{\partial t} = \frac{4\pi}{c}\underline{J}$$

where $\rho = n(\underline{r}) - n_o(\underline{r})$. n_o is the density of the electrons in the absence of the EM fields. $n(\underline{r})$ represents the departure from equilibrium of the electron density. $\underline{J}$ is the current density.

The second harmonic current density $\underline{J}(2\omega) = e(n_o V_2 + n_1 V_1)$ can be calculated by expanding $\underline{E}$, $\underline{H}$, $\underline{V}$, and n.

$$\underline{E} = \underline{E}(\omega)\, e^{-i\omega t} + \underline{E}(2\omega)\, e^{-i2\omega t} \qquad (2.3)$$

$$\underline{H} = \underline{H}(\omega)\, e^{-i\omega t} + \underline{H}(2\omega)\, e^{-i2\ t} \qquad (2.4)$$

$$\underline{V} = \underline{V}_1\, e^{-i\omega t} + \underline{V}_2\, e^{-i2\omega t} \qquad (2.5)$$

$$n = n_o(\underline{r}) + n_1 e^{-i\omega t} + n_2 e^{-i2\omega t} \qquad (2.6)$$

where $|\underline{E}(\omega)| >> |\underline{E}(2\omega)|$, $|\underline{H}(\omega)| >> |\underline{H}(2\omega)|$, and $|n_o| >> |n_1| >> |n_2|$.

The gas is assumed to be at rest initially. $\underline{V}$ and n represent departures from equilibrium.

An expression for $\underline{V}_1$ can be obtained by substituting equation 2.5 into the equation of motion and collecting terms with $e^{-i\omega t}$.

$$\frac{\partial \underline{V}}{\partial t} = \frac{e\underline{E}}{m}\omega = i\omega \underline{V}_1 \tag{2.7}$$

or

$$\underline{V}_1 = \frac{ie}{m\omega}\underline{E}(\omega) \tag{2.8}$$

$\underline{V}_2$ can be expressed in terms of $\underline{V}_1$ by collecting terms with $e^{-i2\omega t}$ and equating the coefficients.

$$-2i\omega \underline{V}_2 + (\underline{V}_1 \cdot \nabla)\underline{V}_1 = \frac{e}{mc}\underline{V}_1 \times \underline{H}(\omega) \tag{2.9}$$

The second order term due to $\underline{E}(2\omega)$ was omitted since $|\underline{E}(2\omega)| << |(\underline{V}_1/c) \times \underline{H}(\omega)|$. This can be seen from the following calculation. The peak output power density of the simultaneously Q switched and mode-locked Nd glass laser is $\sim 10^9$ W/cm.^{2} [16] which corresponds to $|\underline{E}(\omega)| = 8.67 \times 10^5$ V/cm. and $|\underline{H}(\omega)| = 2.89 \times 10^3$ gauss. The experimental SHG efficiency has been calculated to be 10^{-13}. Therefore, $|\underline{E}(2\omega)|$ is found to be 2.74×10^{-1} V/cm. which is smaller than $|(\underline{V}_1/c) \times \underline{H}(\omega)| = 2.47 \times 10$ V/cm. and can be neglected. Faraday's law for non magnetic media is

$$\nabla \times \underline{E} = -\frac{1}{c}\frac{\partial \underline{H}}{\partial t} \tag{2.10}$$

$$= \frac{i\omega}{c}\underline{H}(\omega) \tag{2.11}$$

Equation 2.11 can be rewritten as

$$\underline{H}(\omega) = \frac{c}{i}(\nabla \times \underline{E}(\omega)) \qquad (2.12)$$

Substituting 2.12 into 2.9 and multiplying each side by m gives

$$-2im\omega\underline{V}_2 + m(\underline{V}_1\cdot\nabla)\underline{V}_1 = \frac{e}{c}\underline{V}_1 \times \left(\frac{c}{i\omega}\nabla \times \underline{E}(\omega)\right) \qquad (2.13)$$

Solving for $\underline{V}_2$ and eliminating $\underline{V}_1$ by substituting 2.8 gives

$$\underline{V}_2 = \frac{ie^2}{2m^2\omega^3}((\underline{E}(\omega)\cdot\nabla)\underline{E}(\omega) + \underline{E}(\omega) \times (\nabla \times \underline{E}(\omega)) \qquad (2.14)$$

Equation 2.14 can be simplified further by using the following vector identity.

$$\frac{1}{2}\nabla(\underline{A}\cdot\underline{A}) + (\underline{A}\cdot\nabla)\underline{A} + \underline{A} \times (\nabla \times \underline{A}) \qquad (2.15)$$

Therefore

$$\underline{V}_2 = \frac{ie^2}{4m^2\omega^3}\nabla(\underline{E}(\omega)\cdot\underline{E}(\omega)) = \frac{-e^2}{i4m^2\omega^3}\nabla(\underline{E}(\omega)\cdot\underline{E}(\omega)) \qquad (2.16)$$

From the equation of continuity, n_1 is solved in terms of n_o by retaining only terms to first order

$$\frac{\partial n}{\partial t} + \nabla(n\underline{V}) = 0$$

$$= i\omega n_1 + \nabla\cdot(n_o(\underline{r})\,\underline{V}_1) \qquad (2.17)$$

or

$$i\omega n_1 = \nabla\cdot(n_o(\underline{r})\ \underline{V}_1) \qquad (2.18)$$

Therefore

$$n_1 = \frac{-i}{\omega}\ \nabla\cdot(n_o(\underline{r})\ \underline{V}_1) \qquad (2.19)$$

Substituting for $\underline{V}_1$ by using 2.8 gives

$$n_1 = \frac{e}{m\omega^2}\ (\nabla\cdot n_o(\underline{r})\ \underline{E}(\omega)) \qquad (2.20)$$

By using 2.20, 2.16, and 2.8, the second harmonic current density is calculated to be

$$\underline{J}(2\omega) = e(n_o\underline{V}_2 + n_1\underline{V}_1)$$

$$= \frac{-e^3}{im^2\omega^3}\ \frac{(n_o(r)\ \nabla(\underline{E}(\omega)\cdot\underline{E}(\omega))}{4}$$

$$+ \underline{E}(\omega)\ (\nabla\cdot n_o(\underline{r})\ \underline{E}(\omega))) \qquad (2.21)$$

To show more clearly the separate contributions of the bulk and surface terms, an alternate form of $\underline{J}(2\omega)$ is obtained by substituting equation 2.8 directly into equation 2.9. The change in the velocity of the electrons to second order is

$$\underline{V}_2 = - \frac{e^2}{2m^2\omega^2 c} (\underline{E}(\omega) \times \underline{H}(\omega)) - \frac{e^2}{i2m^2\omega^3} (\underline{E}(\omega) \cdot \nabla)\underline{E}(\omega) \tag{2.22}$$

By using 2.22, 2.20, and 2.8, the second harmonic current density is calculated to be

$$\underline{J}(2\omega) = e(n_o \underline{V}_1 + n_1 \underline{V}_1)$$

$$= - \frac{n_o(\underline{r})e^3}{2i\omega^3 m^2} (\underline{E}(\omega) \cdot \nabla)\underline{E}(\omega) - \frac{e^3 \underline{E}(\omega)}{im^2\omega^3} (\nabla \cdot n_o(\underline{r})\underline{E}(\omega))$$

$$- \frac{n_o(\underline{r})e^3}{2m^2\omega^2 c} (\underline{E}(\omega) \times \underline{H}(\omega)) \tag{2.23}$$

In 2.23, ($\underline{E}(\omega)$ X $\underline{H}(\omega)$) is the second harmonic current density term due to the Lorentz force and receives contributions to within the penetration depth $\sim$ 300 Å for Hg at λ= 1062.3 nm. Therefore ($\underline{E}(\omega)$ X $H(\omega)$) is called the bulk term and is independent of the polarization state of the incident fields as illustrated in FIG. 2.1. A beam oscillating at an angle ϕ with respect to the plane of incidence is incident on a sample, at angle of incidence θ. The ($\underline{E}(\omega)$ X $\underline{H}(\omega)$) term is longitudinal and therefore cannot be the source term of a transverse EM wave unless a boundary is present.

The first two terms of equation 2.23 are called surface terms since they are significant near the surface only. The $(\underline{E}(\omega) \cdot \nabla)\underline{E}(\omega)$ term arises because of the breakdown in inversion symmetry at the surface. Both $(\underline{E}(\omega)\cdot\nabla)\underline{E}(\omega)$ and $(\nabla\cdot n_o(\underline{r})\underline{E}(\omega))$ contain the gradient of the electric field. From electromagnetic theory, we know that E_n, the component of the electric field normal to the metal surface is discontinuous across the boundary. E_n changes from its value outside the metal to a very small value inside the metal within one or two atomic layers of the surface.[4] Thus the

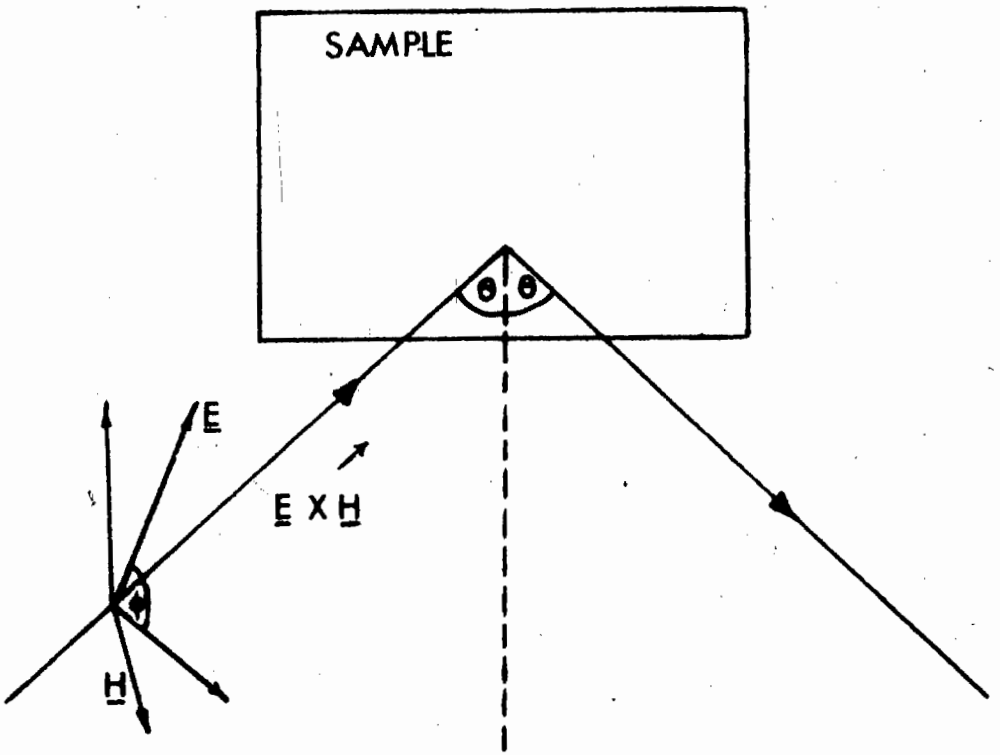

FIG. 2.1 Diagram to illustrate that $\underline{E} \times \underline{H}$ is polarized in the plane of incidence regardless of the polarization state of the incident beam. A fundamental beam polarized at an angle ϕ with respect to the plane of incidence is incident at angle θ on a sample surface.

terms involving $(\underline{E}(\omega)\cdot\nabla)\underline{E}(\omega)$ and $(\nabla\cdot n_o(\underline{r})\underline{E}(\omega))$ are large at the surface region where there is a large gradient of E_n.

The polarization state of the second harmonic radiation as a function of the polarization state of the incident beam can be determined by examining equation 2.23 for the second harmonic current density $\underline{J}(2\omega)$.

Consider FIGS. 2.2 in which the plane of incidence is the Y=0 plane. The light is reflected from plane boundary $X \geq 0$. In (a) the incident beam has both a p and an s component. The surface terms given by the first two terms of equation 2.23 are nonzero since the normal component of $\underline{E}(\omega)$ is discontinuous across the boundary. The non-zero term of $(\underline{E}\cdot\nabla)\underline{E}$ is $E_x\nabla_x E_x$ which contributes to the second harmonic $\underline{E}$ field normal to the surface given by equation 34 in section 2-3.

$\nabla\cdot n_o(\underline{r})\underline{E}$ can be rewritten as $n_o(\underline{r})\ (\nabla\cdot\underline{E})$ $+\ \underline{E}\cdot\nabla n_o(\underline{r})$. $\nabla\cdot n_o(\underline{r})$ is negligible when compared with $\nabla\cdot\underline{E}$. For simplicity, the $\underline{r}$ dependence of $n_o(\underline{r})$ has been neglected. Therefore the non-zero surface terms of $\underline{E}(\nabla\cdot\underline{E})$ are $E_x\nabla_x E_x$, $E_y\nabla_x E_x$, $E_z\nabla_x E_x$. The SH $\underline{E}$ field due to $E_z\nabla_x E_x$ is given by equation A21a. $E_y\nabla_x E_x$ is polarized perpendicular to the

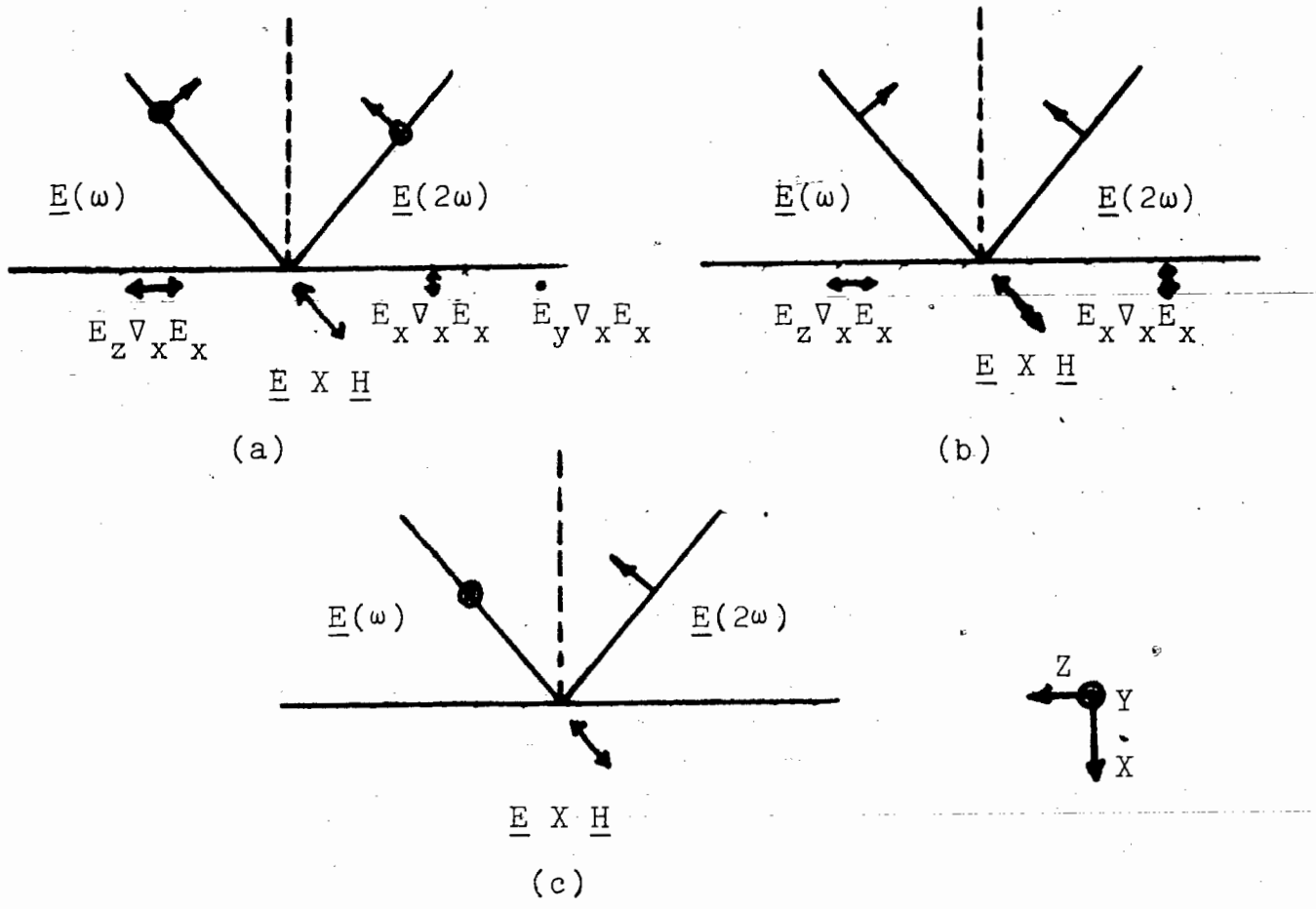

FIG. 2.2 Illustration of the polarization dependence of the second harmonic radiation as predicted by the Classical Hydrodynamical Theory.

plane of incidence and its corresponding $\underline{E}$ field is given by equation A22a for $E_{\parallel s}$.

In FIG. 2.2 (b), the incident beam is polarized in the plane of incidence. The resulting SH $\underline{E}$ field is due to $\underline{E} \times \underline{H}$, $E_x \nabla_x E_x$, and $E_z \nabla_x E_x$. No radiation which is polarized perpendicular to the plane of incidence is generated since E_y is zero.

$\nabla_x E_x$ vanishes when the incident radiation is polarized perpendicular to the plane of incidence as in FIG. 2.2 (c). Therefore no surface currents are generated. The second harmonic radiation generated is due entirely to the $\underline{E} \times \underline{H}$ term.

2-3 SHG THEORY OF RUDNICK AND STERN

A long wavelength calculation of SHG from metals such as the Classical Hydrodynamical Theory, requires that the variation in the EM fields take place over a distance large compared to the Fermi wavelength of the metal. The long wavelength approximation is valid where $\underline{H}$ and the tangential component of $\underline{E}$ are involved, since they are continuous across the boundary. However, the normal component of $\underline{E}$ suffers a discontinuity at the boundary and undergoes a rapid variation. Therefore, a quantum mechanical calculation of the SH fields is necessary.

Rudnick and Stern[1 5] have performed a quantum mechanical calculation for the second order response of an isotropic electron gas. Nonlocal effects were included by using a wavenumber dependent dielectric function. The boundary was replaced by a current sheet, so that all EM fields were considered to be interior. Surface structure effects were neglected since the electron gas was assumed to be isotropic. The long wavelength approximation was found to be valid for the SH $\underline{E}$ fields excited by parallel surface currents, and not valid for the SH $\underline{E}$ field due to

normal surface currents.

Scattering effects due to surface roughness were included by using phenomenological parameters a and b. a is the strength of the nonlinearity in $\underline{E}$ normal to the surface and has been calculated by McCardell[11] to be from 4.8 to 9.46 for SHG from Ag surfaces maintained at $\sim 10^{-10}$ torr. b is the strength of the parallel surface currents. If the surface is flat so that momentum transverse to it is conserved, $|b| = 1$. However, if the boundary is not flat so that the current flowing parallel to it can be scattered, $|b| < 1$, since $\underline{V}_1$ of equation 2.8 and thus the parallel current density will be decreased.

The published equations of Rudnick and Stern for the amplitudes of the second harmonic $\underline{E}$ fields contain typographical errors. My corrected equations and their corresponding numbers in the paper of Rudnick and Stern[15] are presented below.

$$E_{\perp p} = \frac{4ae\omega_p^2 \varepsilon(2\omega) E^2(\omega) \cos^2\phi \sin^3\theta \cos^2\theta}{mc^4[\varepsilon(\omega)k(\omega)+k'(\omega)]^2[\varepsilon(2\omega)k(2\omega)+k'(2\omega)]} \quad (34)$$

$$\frac{E_{\parallel p}}{E_{\pi/2}} = 2b(c/\omega)^2 k'(\omega)k'(2\omega)\cos^2\phi G^{-2}(\omega) \qquad \text{(A21a)}$$

$$\frac{E_{Bp}}{E_{\pi/2}} = \varepsilon(\omega)G^{-2}(\omega)\cos^2\phi + \sin^2\phi \qquad \text{(A21b)}$$

$$E_{\pi/2} = \frac{(2e\omega_p^2/mc^4)\sin\theta\ \cos^2\theta\ E^2(\omega)}{[\varepsilon(2\omega)k(2\omega)+k'(2\omega)][k(\omega)+k'(\omega)]^2} \qquad \text{(A21c)}$$

$$\frac{E_{\parallel s}}{E_{\pi/2}} = -\ 4bG(2\omega)G^{-1}(\omega)\ \cos\phi\ \sin\phi \qquad \text{(A22a)}$$

ϕ is the polarization angle of the incident beam, θ is the angle of incidence as shown in FIG. 2.1, and

$$K(\omega) = -\frac{i\omega}{c}\cos\theta$$

$$K'(\omega) = \frac{-\omega}{c}[\sin^2\theta - \varepsilon(\omega)]^{1/2}$$

$$K'(2\omega) = \frac{-2\omega}{c}[\sin^2\theta - \varepsilon(2\omega)]^{1/2}$$

$$G(\omega) = \frac{\varepsilon(\omega)\ K(\omega) + K'(\omega)}{K(\omega) + K'(\omega)}$$

$E_{\perp p}$ is the amplitude of the electric field normal to the surface and polarized in the plane of incidence. $E_{\parallel p}$ and $E_{\parallel s}$ are the SH $\underline{E}$ fields due to surface currents oscillating parallel and perpendicular to the plane of incidence, respectively. The bulk contributions are given by E_{Bp} which is also p polarized or polarized in the plane of incidence. $E_{\pi/2}$ is the SH $\underline{E}$ field generated when the incident beam is s polarized or polarized perpendicular to the plane of incidence.

The relative second harmonic intensity $|\underline{E}(2\omega)|^2/|\underline{E}(\omega)|^2$ for the surface and bulk terms is plotted as a function of the angle of incidence for $\phi=45^\circ$ in FIG. 2.2. For $\phi=0^\circ$, the curves are similar to those for $\phi=45^\circ$ with respect to θ, but are displaced upwards because of the $\cos^4\phi$ factor. $|\underline{E}_s(2\omega)|^2$ disappears since $\sin 0^\circ$ is zero. For an s polarized incident beam ($\phi=90^\circ$), all terms except $|E_{Bp}(2\omega)|^2 = |\underline{E}_{\pi/2}(2\omega)|^2$ are zero. The θ dependence of $|\underline{E}_{\pi/2}(2\omega)|^2/|\underline{E}(\omega)|^2$ which is defined only for $\phi=90^\circ$, is shown in FIG. 2.2 (f).

The curves in FIG. 2.2 were generated by substituting the dielectric constants of single crystal solid Hg into the equations of Rudnick and Stern.

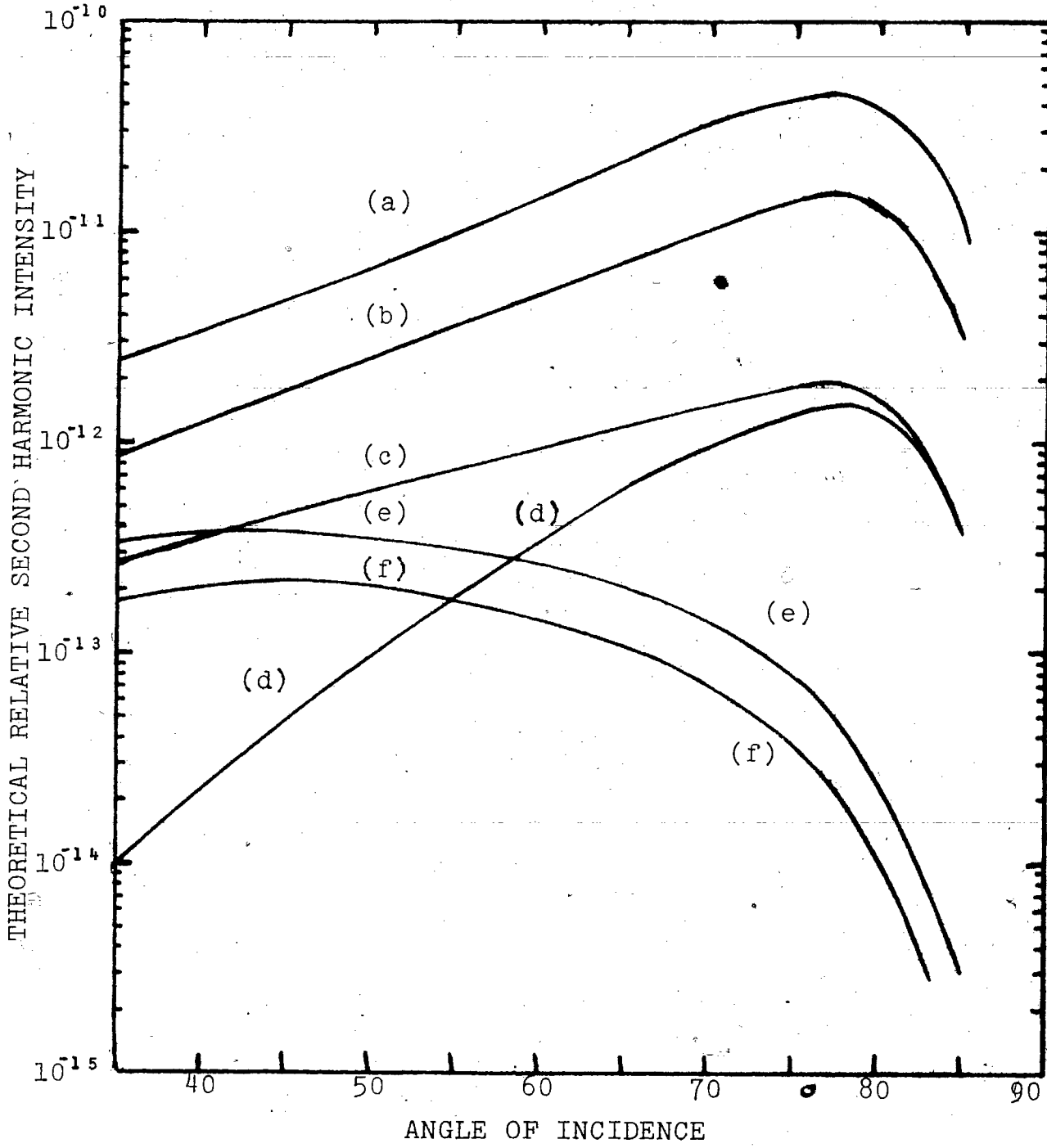

FIG. 2.3 Theoretical intensities of the SH components from the equations of Rudnick and Stern. The relative intensity $|\underline{E}(2\omega)|^2/|\underline{E}(\omega)|^2$ is plotted as a function of angle of incidence. ϕ was taken to be 45 and $|E(\omega)| = 3 \times 10^5$ V/cm. (a) $|E_p(2\omega)|^2/|E(\omega)|^2$ total p component; (b) $|E_{pp}(2\omega)|^2/|E(\omega)|^2$; (c) $|E_{sp}(2\omega)|^2/|E(\omega)|^2$ (d) $|E_{ss}(2\omega)|^2/|E(\omega)|^2$; (e) $|E_{ps}(2\omega)|^2/|E(\omega)|^2$ (f) $|E_{\pi/2}(2\omega)|^2/|E(\omega)|^2$. In the equations of Rudnick and Stern, a and b were taken to be 1. The dielectric constants used were those for single crystal solid Hg.[17]

Similar curves were obtained when the dielectric constants derived from reflectivity and ellipsometry measurements from liquid Hg[4,5] were used. The magnitudes of the SH fields were of the same order as the corresponding fields in FIG. 2.2.

In both cases, the solid and liquid Hg conductivity profiles were assumed to be constant. When a model for Hg in which there was a thin transition layer of high conductivity with a characteristic dielectric constant ε_s followed by the bulk with a characteristic dielectric constant ε_B was considered, the surface SH $\underline{E}$ fields were found to be smaller in magnitude. The results are shown in FIG. 2.3. $\varepsilon_B(\omega)$ and $\varepsilon_B(2\omega)$ were assigned the values used to generate FIG 2.2. The surface dielectric constant was assigned a value 4 times that of the bulk dielectric constant. The intensity of the total p component is smaller by an order of magnitude and its peak shifts from $\theta = 77^\circ$ to $\theta = 79^\circ$. The introduction of a thin transition layer of high conductivity lowers the intensity of the s component relative to the intensity

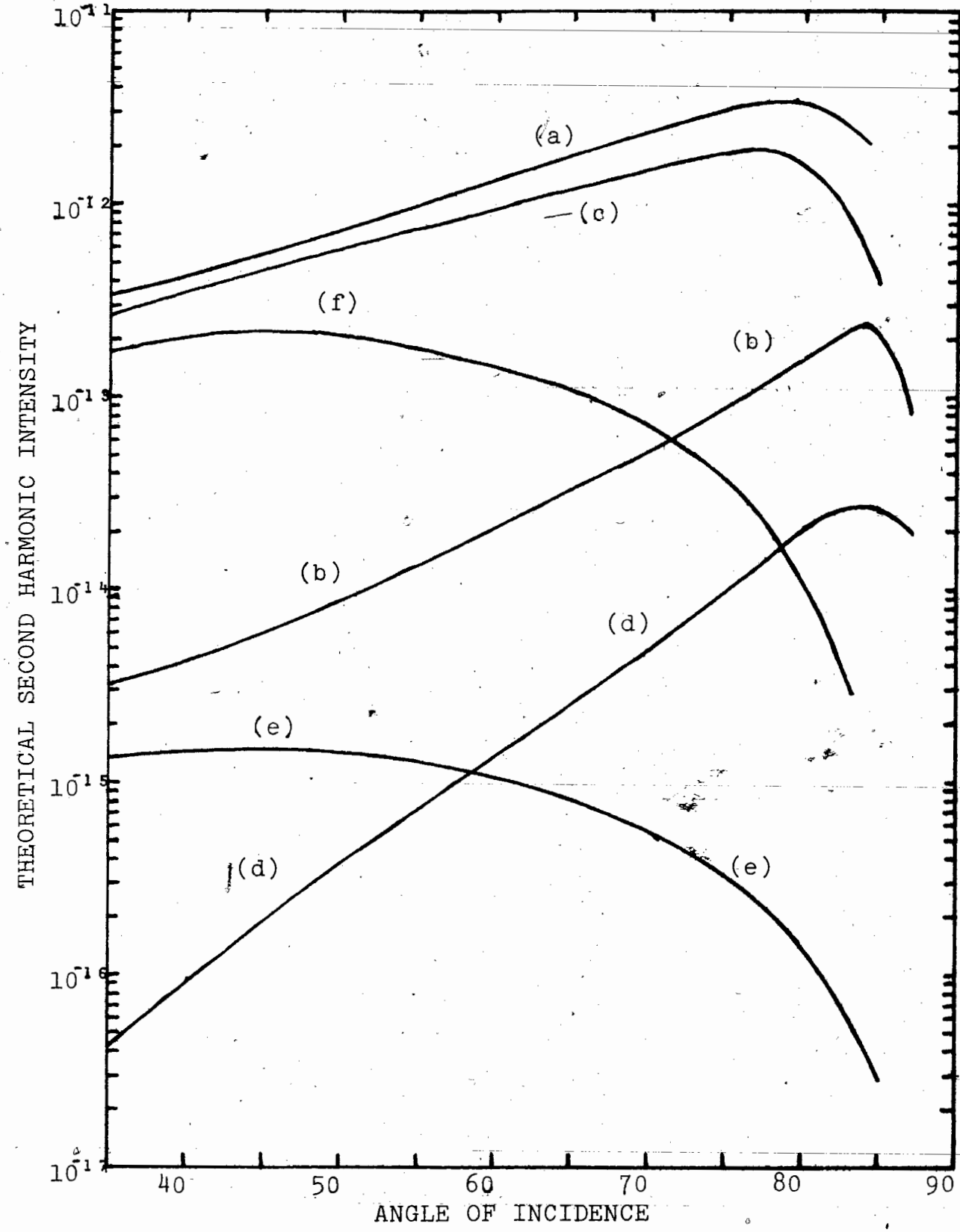

FIG. 2.4 Theoretical SH intensities as a function of angle of incidence for the two layer model of Hg. $\varepsilon = 4\varepsilon$ (a) $|E_{PTOT}|^2/|E(\omega)|^2$ (b) $|E_{\parallel P}|^2/|E(\omega)|^2$ (c) $|E_{BP}|^2/|E(\omega)|^2$ (d) $|E_{\perp P}|^2/|E(\omega)|^2$ (e) $|E_{\parallel S}|^2/|E(\omega)|^2$ (f) $|E_{\pi/2}|^2/|E(\omega)|^2$. From (a) to (e), $\phi=45°$ and (e) $\phi=90°$.

of the total p component. In this particular case, at $\theta = 78^{\circ}$, $|E_{11s}|/|E_{ptotal}| \sim 10^{-4}$ whereas the ratio is $\sim 10^{-3}$ when no transition layer is introduced.

Although the curves in FIGS. 2.2 and 2.3 were generated by using the dielectric constants for solid Hg, the results are indicative of liquid Hg. The results of FIG. 2.3 suggest that for liquid Hg to which a surface transition zone has been attributed, second harmonic radiation is dominated by E_{Bp} of equation A21b. The generation efficiency decreases when a transition zone is introduced. The decrease in generation efficiency is most apparent for the s component of the SH radiation where at $\theta = 78^{\circ}$, $|E_{11s}|^2/|E_{ptot}|^2$ is $\sim 10^{-4}$. Therefore, it is unlikely that s polarized radiation will be detected for angles of incidence around 78°.

It is also apparent from FIGS. 2.5 and 2.6 that at $\theta = 78^{\circ}$, the SH radiation should be p polarized. In FIGS. 2.5 and 2.6, the intensities of the SH fields are plotted against the polarization angle ϕ of the incident beam. The transition zone

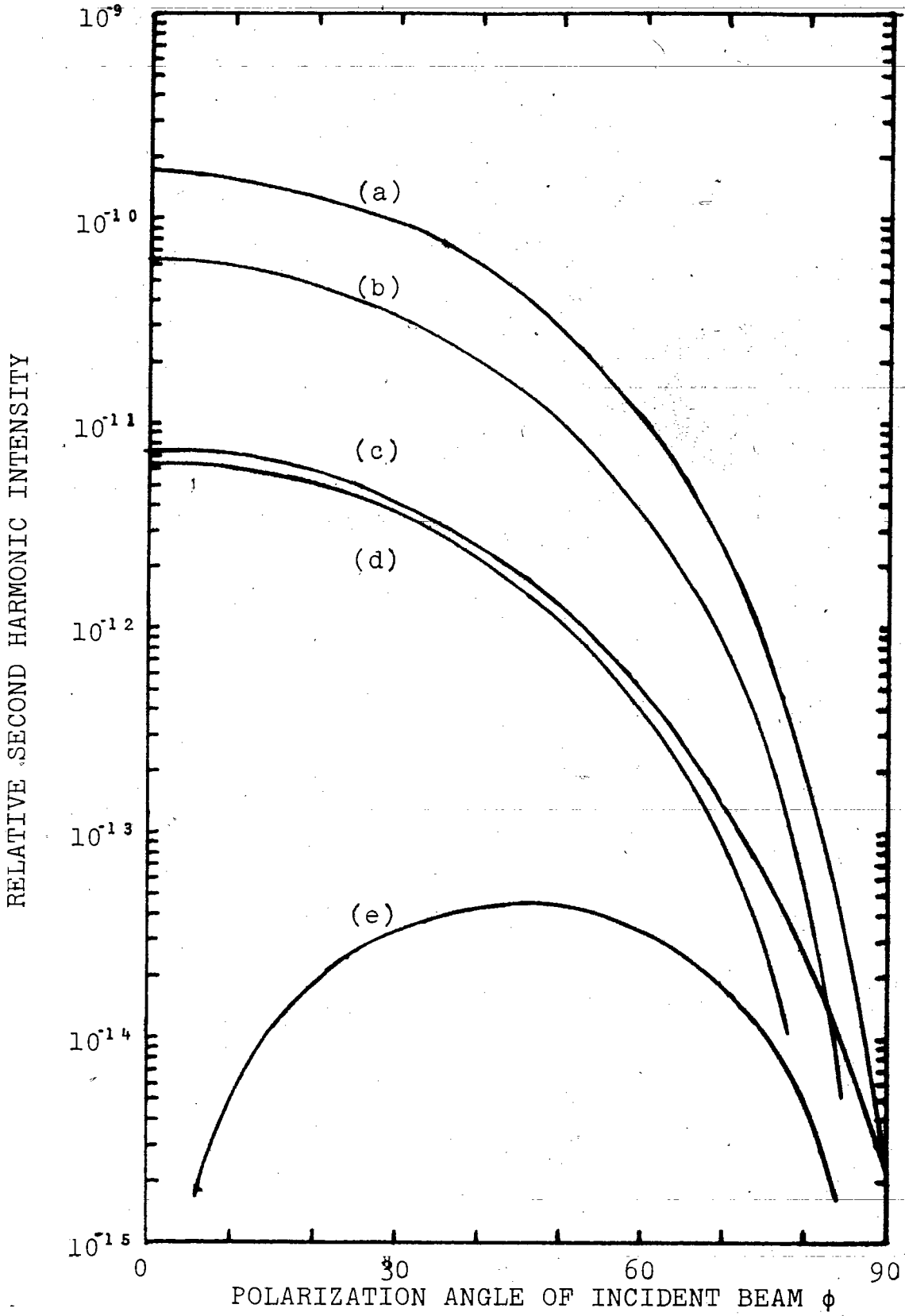

FIG. 2.5 SH intensity as a function of ϕ at $\theta=78^{\circ}$. (a) $|E_{PTOT}(2\omega)|^2/|E(\omega)|^2$ (b) $|E_{\parallel P}(2\omega)|^2/|E(\omega)|^2$ (c) $|E_{BP}(2\omega)|^2/|E(\omega)|^2$ (d) $|E_{\perp P}(2\omega)|^2/|E(\omega)|^2$ (e) $|E_{\parallel S}(2\omega)|^2/|E(\omega)|^2$. phenomenological parameters a=1, b=1.

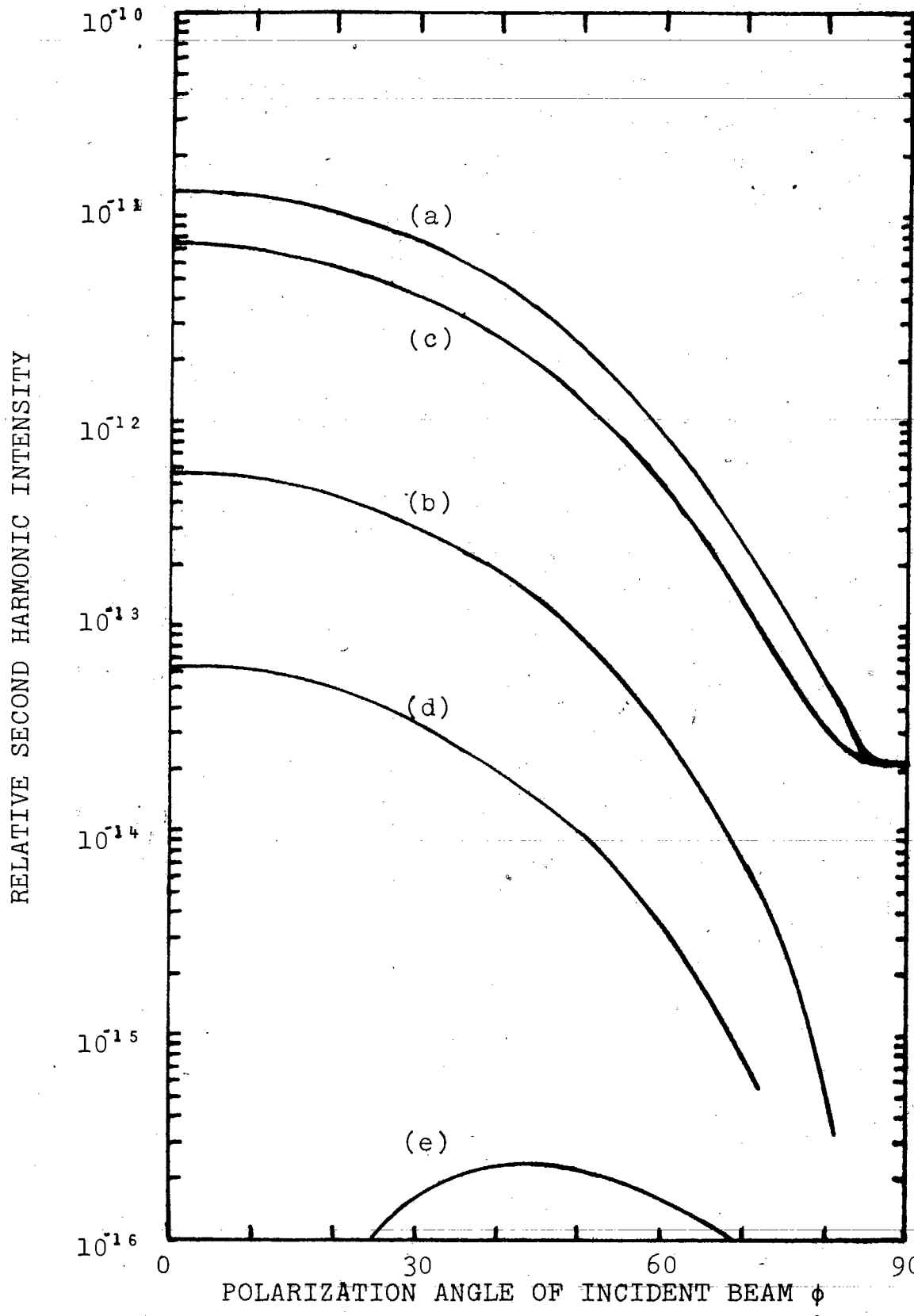

FIG. 2.6 SH intensity as a function of ϕ at $\theta=78^{o}$. (a) $|E_{PTOT}|^2/|E(\omega)|^2$ (b) $|E_{11P}|^2/|E(\omega)|^2$ (c) $|E_{BP}|^2/|E(\omega)|^2$ (d) $|E_{LP}|^2/|E(\omega)|^2$ (e) $|E_{11S}|^2/|E(\omega)|^2$. SH curves for the two layer model of Hg. $\varepsilon_S = 4\varepsilon_B$

was introduced in FIG. 2.6 only. At $\phi=0^{o}$ and 90^{o}, the SH radiation is entirely p polarized. The SH radiation at $\phi=90^{o}$ is due entirely to E_{Bp}. As stated earlier, the SH radiation should be p polarized.

2-4 ANGLE OF REFLECTION OF SH RADIATION

For the purpose of detecting SH radiation, it is essential to know the angle through which the SH radiation is generated.

Bloembergen and Pershan[18] have shown that the SH radiation is generated through the same angle as the fundamental ray.

Consider FIG. 2.6 in which a monochromatic plane wave of frequency ω_1 is incident on a plane boundary. The boundary is given by Z=0 and the plane of incidence by Y=0. The superscripts i and R denote the incident and reflected rays, respectively. The superscript T is used to denote the fields which exist within the metal. An SH current density $\underline{J}\ (2\omega)$ is excited by the fundamental fields. Since the SH current density is dependent on fundamental fields with phase and time factors $\exp(i(\underline{k}_1^T \cdot \underline{X} - \omega_1 t))$, the SH phase and time dependence is $[\exp(i(\underline{k}_1^T \cdot \underline{X} - \omega_1 t))]\ [\exp(i(\underline{k}_1^T \cdot \underline{X} - \omega_1 t))]$

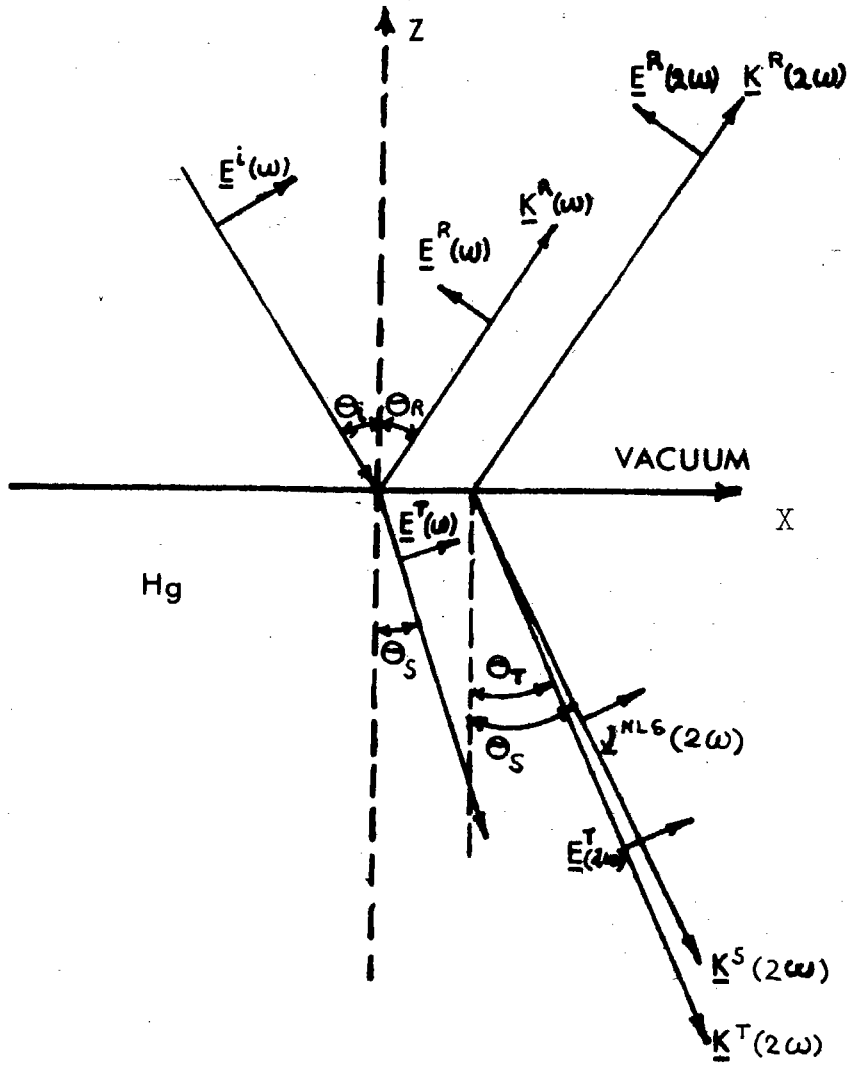

FIG. 2.7 Diagram to illustrate the angle of generation of the second harmonic radiation. R denotes the reflected waves and i denotes the incident beam. $\underline{J}$ is the nonlinear source current density.

which is $\exp(i(2\underline{k}_1^T \cdot \underline{X} - 2\omega_1 t))$.

The existence of boundary conditions at Z=0 which must be satisfied everywhere on the boundary at all times requires that the spatial and time variations of all fields must be the same at Z=0. Therefore

$$(\underline{k}_1^i \cdot \underline{X})_{z=0} = (\underline{k}_1^R \cdot X)_{z=0} = (\underline{k}_1^T \cdot X)_{z=0}$$

or

$$|\underline{k}_1^i| \sin\theta_1^i = |\underline{k}_1^R| \sin\theta_1^R = |\underline{k}_1^T| \sin\theta_1^T \qquad (2.24)$$

For the second harmonic fields, the equivalent equations are

$$|\underline{k}_2^R| \sin\theta_2^R = |\underline{k}_2^T| \sin\theta_2^T = |\underline{k}_2^S| \sin\theta_2^S = 2|\underline{k}_1^T| \sin\theta_1^T \qquad (2.25)$$

$|\underline{k}_2^S|$ is the magnitude of the wavevector of the SH source current density and is equal to $2|\underline{k}_1^T|$.

From equation 2.24, we have for $\sin\theta_1^T$

$$\sin\theta_1^T = \frac{|\underline{k}_1^i|}{|\underline{k}_1^T|} \sin\theta_1^i \qquad (2.26)$$

Similarly, from equation 2.25 we have

$$\sin\theta_1^T = \frac{1}{2}\frac{|\underline{k}_2^R|}{|\underline{k}_1^T|} \sin\theta_2^R \qquad (2.27)$$

Equating 2.26 and 2.27 gives

$$\frac{1}{2} |\underline{k}_2^R| \sin \theta_2^R = |\underline{k}_1^i| \sin \theta_1^i$$

For nonmagnetic media, $|\underline{k}(\omega)| = |\varepsilon^{1/2}(\omega)| (\omega/c)$ where ε is the dielectric constant and c is the speed of light. In the vacuum

$$|\underline{k}(\omega)| = \frac{\omega}{c} \tag{2.29}$$

Substituting 2.29 into 2.28 gives

$$\frac{1}{2} \times \frac{2\omega}{c} \sin \theta_2^R = \frac{\omega}{c} \sin \theta_1^i$$

or

$$\sin \theta_2^R = \sin \theta_1^i \tag{2.30}$$

From the law of reflection, we know that $\theta_1^i = \theta_1^R$. Therefore, equation 2.30 implies that

$$\theta_1^i = \theta_1^R = \theta_2^R \tag{2.31}$$

The second harmonic radiation is generated through the same angle as the fundamental ray.

CHAPTER 3

APPARATUS

3-1 INTRODUCTION

A pasively Q switched and mode locked Nd glass laser was used as the light source. A description of the laser is presented in section 3-2. Passive Q switching and mode locking are discussed in section 3-3. The optical arrangement used in detecting the SH signals is described in section 3-4. In the final section, a description of the ultrahigh vacuum system which was used to contain the Hg is presented.

3-2 NEODYMIUM GLASS LASER

In the initial investigations, the Nd glass laser constructed by R. Ninnis was used.[19] The flashlamp was linear, and heat damage to the Nd^{3+} doped glass rod was prevented by pumping cooling water from a reservoir through the laser head containing the glass rod. However, the laser output is important for applications where a single pulse is to be selected from the mode locked train. A commercial laser (Korad, Hadron Co.) was substituted. An Owens-Illinois ED-2 lithium aluminum silicate glass rod, 29.2 cm. in length and 1.0 cm.

in diameter was used. The rod ends were cut at Brewster angle so that the laser output was linearly polarized. The front exit mirror was 65% reflecting and the rear mirror was 100% reflecting at the laser wavelength of 1062.3 nm. Unlike the laser of Ninnis, optical pumping of the laser amplifying medium (glass rod) was achieved with a helical flashlamp. Since the lamp electrodes came into direct contact with the cooling water, de-ionized water was used in order to prevent the lamp from shorting. For prolonged operation of the laser, it was necessary to maintain the cooling water reservoir in an ice bath. The optical path length of the cavity was 112 cm. which corresponded to a cavity round trip time of 7.5 nanoseconds.

The helical flashlamp provided a more uniform optical pumping of the Nd glass rod, than the linear flashlamp. Single mode TEM_{oo} operation of the laser with a Gaussiam energy distribution in the output was readily attainable, whereas the linear flashlamp assembly of Ninnis, resulted in multimode polaroid burn patterns. Helical flashlamps have larger wall arears and arc lengths per linear centimeter and, therefore, can deliver much higher pulse energies

to a given size laser rod than a single linear flashlamp. Hence, in cases where high peak power is desired, helical flashlamps are used, whereas linear flashlamps find favour with high average power or high repetition rate lasers since a cooling liquid is more readily circulated.

The 65% reflecting exit mirror was manufactured by Valpey Corp. Two types of 100% reflecting mirrors (Valpey Corp. and Optikon) were tried. Although the Optikon mirror was listed as being able to withstand power densities of 2 Gw/cm^2, its useful lifetime ($\sim$ 2 days) was found to be about the same as for the Valpey mirror. Therefore, realignment of the mirrors and the optics of the SH detection system, was necessary on the average, every two days. The method used in readjusting the mirrors is described by Ninnis.[19]

No satisfactory method was found for cleaning the mirrors and other optical components. Liquid cleaning was found to promote damage rather than hinder it. There are two possible sources of damage. Firstly, incomplete drying of the liquid can lead to absorption by the optical surfaces. Miniature

explosions are produced when laser pulses strike the absorbed liquid. In particular, the laser rod ends were pitted after liquid cleaning. Secondly, cleaning residue may have been melted onto the surfaces and left indentations after being dislodged by subsequent laser pulses. The Optikon mirror was found to be extremely sensitive to cleaning by volatile liquids such as methanol and acetone. The drying of the liquid was accompanied by the peeling of the dielectric coating from the quartz substrate. Eventually, damage to the optical components was minimized by reducing the frequency of liquid cleaning and the amount of liquid used. Dust was eliminated from the working area by spraying compressed air.

The image of the He-Ne alignment laser beam was seen to expand and fade, and return to normal with each firing of the Nd glass laser. This effect is known as thermal lensing, in which the heating and cooling of the glass rod leads to a nonuniform temperature of the rod, which leads to a temperature and stress dependent variation of the index of refraction. Thermal lensing also affects the output power of lasers. In order to take advantage of this effect, the laser

was fired once every 15 seconds when the output power was near the maximum value. In addition, when operated in the thermal lensing mode, the fine tuning of the passively Q switched and mode locked laser was facilitated, with an improvement in the reproducibility of the mode locked pulses.

The maximum voltage availabe from the power supply was 10 kv. In the passively Q switched and mode locked operation of the Nd glass laser, a typical operating voltage was 5.3 kv., corresponding to an input energy of 1.4×10^3 joules. The charge was contained in a 100 microfarad capacitor.

3-3 PASSIVE Q SWITCHING AND MODE LOCKING

Q switching is a mode of laser operation employed for the generation of high pulse power. The optical Q, which is the ratio of the energy stored in the cavity to the energy loss per cycle is altered in Q switching. Energy is stored in the amplifying medium by optical pumping while the quality factor Q is lowered to prevent laser emission. As a result, the population inversion reaches a level far above the threshold. When the optical Q is increased, the stored energy is released as a short pulse of light.

The switch in Q may be achieved in two ways. In active Q switching, an active modulator (eg. electrooptic shutter) is driven externally. In the passive method (eg. saturable dye absorber) the switch in Q is achieved internally.

Experiments to decide the most suitable saturable absorber were conducted and are described in 4-2.

A brief description of passive mode locking follows. For detailed descriptions see references 16 and 19.

When two or more longitudinal modes begin oscillating, the interaction between $\underline{E}$ fields of the modes and the nonlinear saturable absorber leads to a periodic amplitude fluctuation at the difference frequency $\Delta\nu = c/2L$, where c is the speed of light and L is the optical cavity length. Since higher amplitude $\underline{E}$ fields are transmitted more readily than the $\underline{E}$ fields lower in amplitude, the initially sinusoidal waveform is distorted on passage through the absorber. Pulse narrowing occurs because the wings of the pulse are more strongly absorbed than the peak. The interaction between the modes and the saturable absorber which behaves as an amplitude modulator, excites additional sidebands within the laser bandwidth. Since the sidebands represent other modes oscillating with a definite phase relationship, the laser output consists of a series of sharp spikes separated in time by the cavity round trip time. Therefore, in order for a saturable absorber to mode lock the laser output, the recovery time from the saturated state of the dye must be less than the cavity round trip time. In addition,

the dye must have an absorbing transition at the laser frequency and a bandwidth greater than or equal to the laser line width.

3-4 OPTICAL ARRANGEMENT

Due to the extremely low conversion efficiency $|\underline{E}(2\omega)|^2/|\underline{E}(\omega)|^2 \sim 10^{-15}$ of the fundamental beam into Sh radiation,[8] a high peak power Nd glass laser was used as the light source and high gain EMI 9526 B photomultipliers (Baytronix Ltd.) were used to detect the SH signals.

The optical arrangement is shown in FIG. 3.1. The electronic detection system shown in FIG. 3.1 will be discussed in 4-5.

A part of the Nd glass laser beam was reflected by a beam splitter for detection by the ultrafast photodiode. The beam splitter was placed close to the Brewster angle to maximize transmission. The resulting pulse wad displayed on the Tektronix 519 oscilloscope. The 519 scope has a risetime of 0.5 nanosecond and was used to monitor mode locking in the laser wavetrain.

In order to eliminate errors due to shot to shot fluctuations in laser output, a normalizing technique was used by passing a portion of the

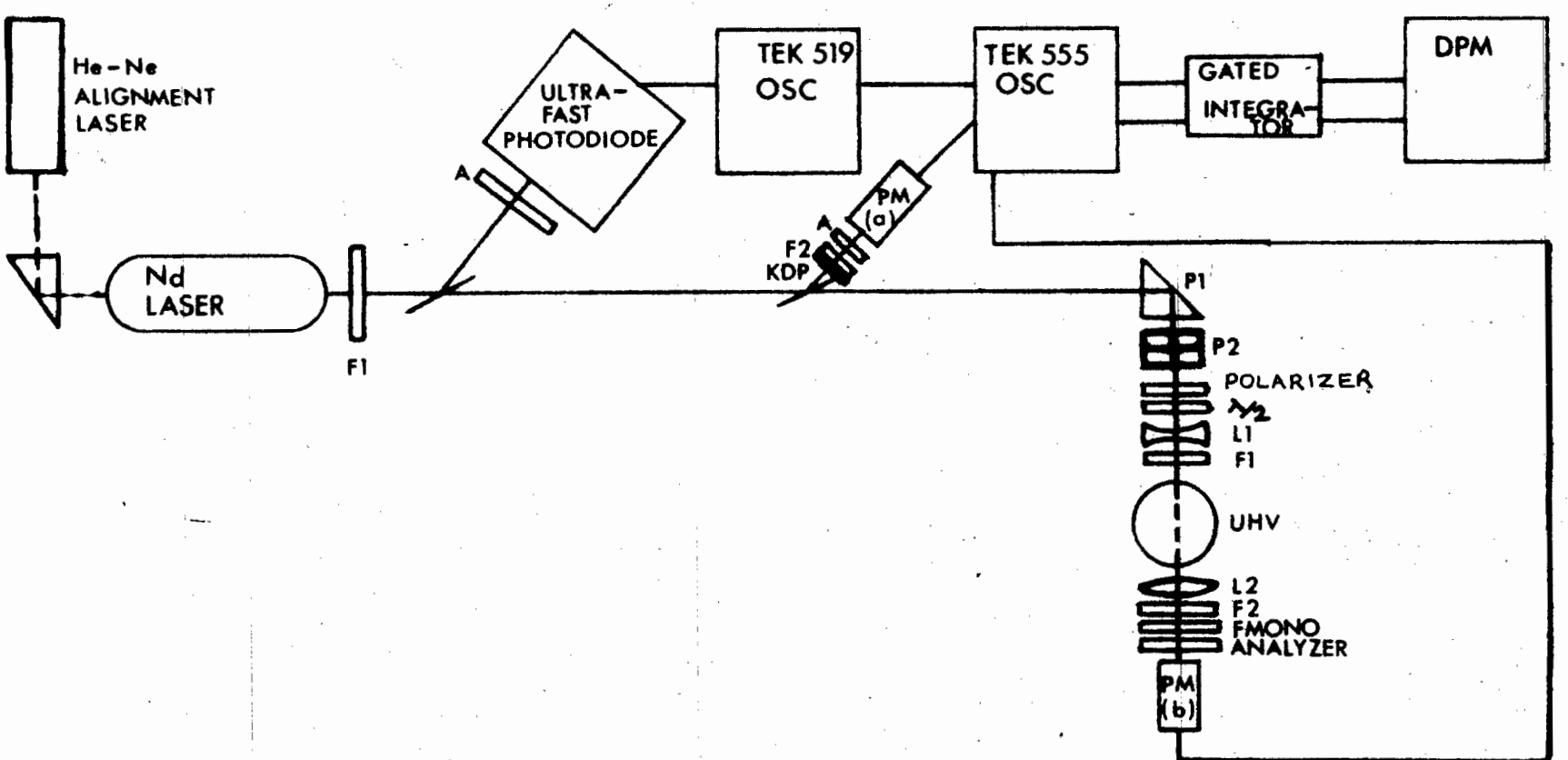

FIG. 3.1 Optical arrangement of the SH detection apparatus. A, neutral density filter; KDP, potassium dihydrogen phosphate; F1, 1062.3 nm pass and 531.2 nm stop filter; F2, 531.2 nm pass and 1062.3 nm stop filter; PM, EMI 9526 B photomultiplier; P1 and P2, right angle prisms; polarizer and analyzer, Glan-Thompson prisms; $\lambda/2$, half wave plate; L1, expanding lens; L2, collecting lens; UHV, ultrahigh vacuum system with Pyrex vacuum housing; FMONO, Monopass narrow bandpass filter; DPM, Digital Panel Meter.

laser beam through KDP (potassium dihydrogen phosphate) powder to generate a reference second harmonic signal. The KDP powder was sandwiched between two microscope glass slides. The thickness of the powder was $\sim$ 1 mm.

Neutral density filters were used to attenuate the reference second harmonic signal to a level appropriate for detection by a photomultiplier. The signal was then read on the digital panel meter (DPM) after being amplified by the Tektronix 555 oscilloscope and integrated by the gated integrator.

The direction of the laser beam was altered in the horizontal plane by total internal reflection in the right angle prism P1. A second right angle prism P2 was used to direct the laser beam onto the horizontal surface of the liquid samples. The angle of incidence was determined to within $\pm$ 1^{o} by measurements made with a He-Ne laser beam which was adjusted to be collinear with the Nd glass laser beam at the Hg surface. The angle was calculated by measuring the positions of the He-Ne laser beam when

the right angle prism P2 was absent from the optical arrangement and when P2 was present.

The polarization state of the radiation incident on the sample was varied with a Glan-Thompson prism and a quartz $\lambda/2$ plate for 1060 nm. The transmission plane of the prism was set in the plane of polarization of the incident beam to within $\pm 1^{o}$. Once this was accomplished, the polarization of the radiation incident on the sample within the vacuum system was changed by varying only the orientation of the $\lambda/2$ plate. The transmission axes of the polarizer and analyzer, and the fast and slow axes of the $\lambda/2$ plate were deduced from photometric measurements of the intensity of a He-Ne laser beam transmitted by the polarizer, analyzer and waveplate positioned at different settings.

Lens L1 was used to expand the cross sectional area of the beam incident on the sample. This was necessary to minimize plasma generation. Lens L2 was used to collect the light from the sample and to focus it on PM (b), the photomultiplier.

F1 and F2 are optical bandpass filters. F1, Corning filter CS-264, was the fundamental pass filter, transmitting radiation in the range 640 nm. to 4500 nm. F2, Corning CS-494, was the SH pass filter, trans-

mitting radiation in the range 330 nm. to 640 nm.

Two methods were used to determine the spectral distribution of the radiation from the sample within the ultrahigh vacuum system. In preliminary tests, a Jarrel-Ash monochromator was found to be unsuitable. The necessity of varying the angle of incidence made the alignment too difficult. As a result, Monopass narrow bandpass filters (FMONO) with λ_p, the peak transmittance wavelength in the range 438 nm. to 591 nm. were used. Luminescence was not observed. The typical peak transmittance of the filters was $\sim$ 35% and the full width at half maximum (FWHM) $\sim$ 15 nm.

3-5 ULTRAHIGH VACUUM SYSTEM

In order to investigate SHG from clean Hg surfaces, the Hg was distilled into an ultrahigh vacuum system (UHV). A schematic diagram of the UHV is shown in FIG. 3.2.

A rotary vane-type mechanical pump was used as the forepump to reduce the pressure of the vacuum system to $\sim 10^{-3}$ torr., at which the high vacuum oil diffusion pump (NRC HS-II) was switched on. The diffusion pump oil used was NRC 705.

The molecular sieve minimized backstreaming of the oil from the mechanical pump into the bulk of

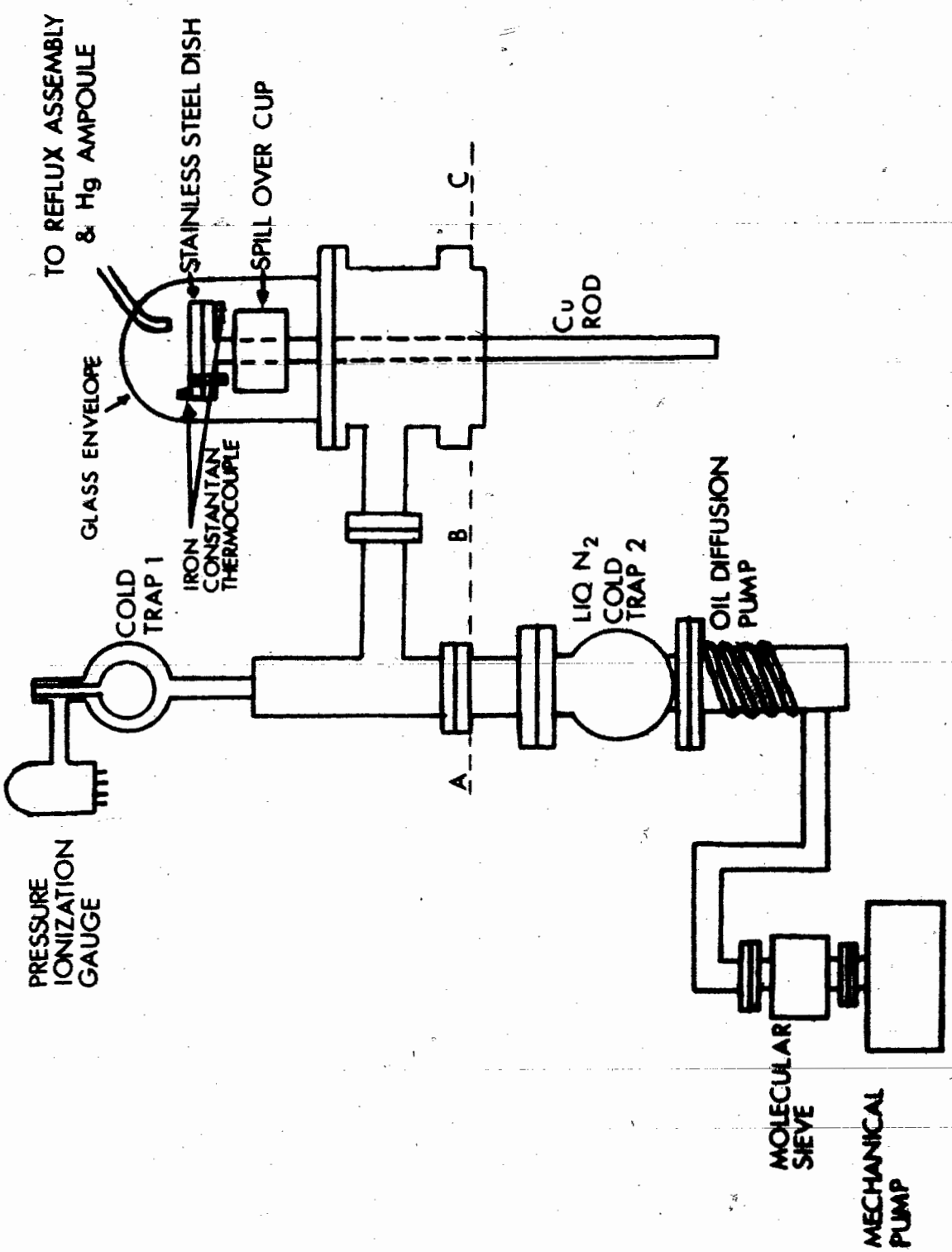

FIG. 3.2 ULTRAHIGH VACUUM SYSTEM

the system.

Ultrahigh vacuum conditions were maintained by filling cold trap 2 (Granville Phillips) every 6 hours with liquid N_2. The refill frequency was increased to 8 times a day or once every 3 hours during bake out. The bake out procedure will be discussed in section 4-6. Cold trap 1 was installed in order that pressure readings could be taken after the distillation of Hg into the stainless steel dish. The vapour pressure of Hg at 20°C is $\sim 10^{-3}$ torr. Fresh surfaces were obtained by distilling Hg into the stainless steel dish (SS 316) until the Hg spilled over into the spill over cup.

The Hg was contained in an ampoule, separated from the rest of the vacuum system by a glass seal. The seal was broken by dropping a magnetic rod while the system was maintained at ~~ultra~~high vacuum conditions. The 99.9% pure Hg was prepared by refluxing for several hours in a vacuum system maintained at 10^{-6} torr., and then distilled into an ampoule.

Hg temperatures from 26°C to -131°C were obtained by varying the level of immersion of the Cu rod attached to the stainless steel dish, in a

dewar filled with liquid N_2. Iron Constantan thermocouples were used to measure the temperature of the Hg.

The vacuum system, excluding the mechanical pump and the molecular sieve, was mounted on a table, which could be adjusted to the proper height for a particular angle of incidence.

The dotted line A-B-C indicates the level of the table surface. In the bake out procedure, to be described in section 4-6, only the portion of the system above the dotted line was heated.

CHAPTER 4

EXPERIMENTAL METHODS AND RESULTS

4-1 INTRODUCTION

In this chapter, the preliminary work performed in bringing the apparatus to a condition suitable for the detection of SHG from Hg, is discussed. The results from the investigations of SHG from Hg surfaces are also presented.

Although theoretical analyses of passive mode locking have been presented,[20, 21] there is not yet a prescription by which a reproducible mode locked pulse of specified characteristics may be generated. The mode locked output suffers from the excitation of multiple pulse trains, incomplete mode locking, multiple pulsing due to the incomplete bleaching of the saturable dye, and variations in the intensity. In attempts to improve the performance of the mode locked laser, experiments were conducted with different dyes (4-2), different cell designs (4-4), and different positions of the dye cell (4-3) within the cavity.

The electronic instrumentation is described in 4-5. As reported earlier, the bake out procedure

is discussed in 4-6. The SHG results for Ag are presented in 4-7. The results for liquid Hg and solid Hg are discussed in sections 4-8 and 4-9 respectively.

4-2 TESTS FOR BEST DYE

In order to determine the dye best suited for use with the Nd glass laser, two saturable dyes, EK (Eastman Kodak) 9860, and EK 14015 were examined. The former is a standard dye for use with Nd glass lasers. However, it has the disadvantage of being sensitive to ultraviolet light. When exposed to ultraviolet radiation (eg. from the laser flashlamp), the dye decomposes.

Recently, a new dye EK 14015 was introduced by Drexhage and Reynolds[22] for use with Nd glass lasers. They indicated the dye to be highly stable in use and in storage. When dissolved in the EK 9860 solvent, 1,2 dichloroethane, the dye was found to Q switch but not mode lock the laser pulses. This was attributed to the relatively long recovery time $\sim 10^{-9}$ sec., of the dye solution from the saturated state. An output which is Q switched but not mode locked, appears as a single giant pulse instead of a series

of sharp spikes as in the mode locked case. EK 14015 has the attractive feature that the recovery time from the saturated state can be varied from $\sim 10^{-9}$ sec. to $\sim 10^{-12}$ sec. with suitable substitutions and concentrations of the solvents. It is possible to investigate the influence of the recovery time of a saturable absorber on the mode locking behaviour of a solid state laser. Mode locked pulses were observed by DR (Drexhage and Reynolds) involving sulfoxides, sulfides, pyridine derivatives and iodoethane as solvents. In the present study, ethyl sulfide, pyridine, iodoethane and 1,2 dichloroethane were used. In agreement with DR, when EK 14015 was dissolved 1,2 dichloroethane, the laser output was Q switched but not mode locked. Mode locking did not occur reliably with ethyl sulfide and pyridine. The toxic nature of ethyl sulfide makes it undesirable as a solvent. In contrast to the reported work of DR, EK 14015 was found to be highly unstable when dissolved in pure pyridine as well as in mixtures of 1,2 dichloroethane and pyridine. The degradation of the dye occurred over storage periods as short as 24 hours, although the dye solution was kept in light-tight containers. Iodoethane as the solvent

yielded the best results. However, the useful lifetime of the dye solution was found to be ∿50 laser shots.

In an attempt to lengthen the storage lifetimes, the EK 9860 solution and EK 14015 dissolved in iodoethane were stored at 4°C. After six months, the two dyes were not able to mode lock the Nd glass laser reliably. When stored at room temperature, the lifetime of EK 9860 was ∿ six months. Subsequent heating of the EK 9860 solution did not improve its mode locking properties. It was concluded that the degradation of the EK 9860 solution was due to chemical decomposition and not due to precipitation of the dye solid.

Eventually, it was decided to use EK 9860 as the saturable absorber.

4-3 DIFFERENT DYE CELL POSITIONS

According to Drexhage and Reynolds, mode locking occurred most reliably with the dye cell in the optical center. The position of the dye cell within the laser cavity was varied in order to observe the performance characteristics of the laser as a function of cell position.

The distance L/m, of the cell, from the 100% reflecting back mirror was varied. L is the optical

length of the laser cavity which is ∿ 112 cm, and m is a positive non-zero integer. A value of one for m corresponds to the cell being placed immediately next to the rear mirror. m equal to two corresponds to the cell being placed at optical center, and so on. Hand reproduced diagrams of the results are shown in FIG. 4.1. When m was one, the output normally consisted of a series of sharp spikes separated in time by the cavity round trip time T equal to 7.5 nanoseconds, as shown in FIG. 4.1 (a). With the cell at the optical center, the spikes were separated by the half the round trip time. In contrast with the results of Drexhage and Reynolds, no improvement in mode locking reliability was observed over the previous case with the cell next to the rear mirror. Pulse quality suffered greatly for m greater than two. FIG. 4.1 (c) shows the laser output for m equal to three. The pulses were separated by the cavity round trip time divided by three. As observed by Harrach and Kachen[2,3] the pulses followed a sequence of one large spike and two small spikes. The output was not mode locked for larger values of m.

For the SHG tests, the cell was placed immediately next to the 100% reflecting mirror.

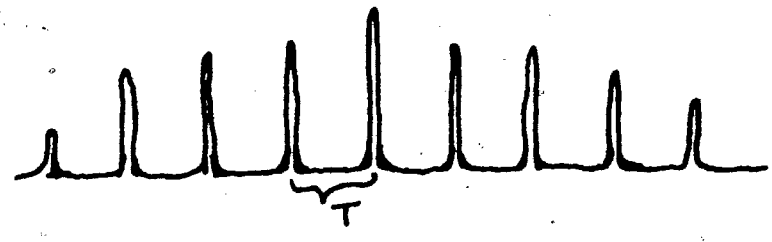

(a)

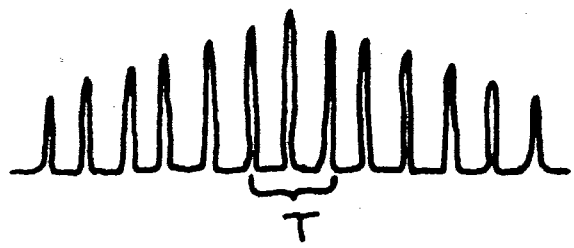

(b)

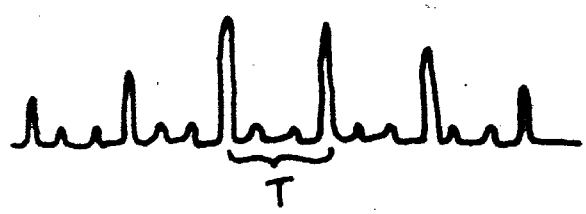

(c)

FIG. 4.1 The effect of the dye cell position on the laser output. In (a) d=L; (b) d=L/2; and (c) d=L/3. T is the cavity round trip time.

4-4 DIFFERENT CELL DESIGNS

Two dye cells with path lengths of 1.65 mm. and 10 mm. were examined in order to determine the cell from which the more reliable mode locking could be obtained. A laser is said to be reliably mode locked when outputs of the type depicted in FIG. 4.1 (a) are consistently produced.

The EK 6088 liquid Q switch cell is commonly used to contain saturable absorbers for Nd glass lasers. Antireflection coated windows eliminate the need to place the cell at the Brewster angle with respect to the laser beam to minimize reflection losses. A path length of 1.65 mm. is provided by a teflon spacer. A typical dye concentration used was 3.6% by volume of EK 9860 Q switch solution in 1,2 dichloroethane.

Rentzepis (private communication) has obtained reliable mode locking with the EK 9860 dye in a cell with ordinary pyrex glass windows separated by a 10 mm. thick teflon spacer, placed at the Brewster angle within the laser cavity.

In the present study, the better results were obtained with EK 6088 cell. Mode locked pulses similar to those depicted in FIG. 4.1 (a) were

obtained regularly. However, when a cell similar to that of Rentzepis was used, the laser output tended to assume the behaviour shown in the hand reproduced diagrams of FIG. 4.2. A partially mode locked pulse is shown in FIG. 4.2 (a). Parts (b) and (c) show examples of multiple pulsing and the excitation of multiple pulse trains respectively. In addition, the performance of the laser was found to be extremely sensitive to the concentration of the dye. At 0.8% by volume of the EK 9860 solution in 1,2 dichloroethane, the laser could not be fired, whereas at 0.4% by volume, evidence of mode locking was seen. There is another disadvantage to using a cell similar to that of Rentzepis. Thicker cells are inherently inferior due to a lens effect called self-trapping, which can greatly increase the light power density in the dye and reduce its useful lifetime![16]

Consequently, all the results reported in chapter 4 were obtained with the EK 6088 liquid switch cell.

(a)

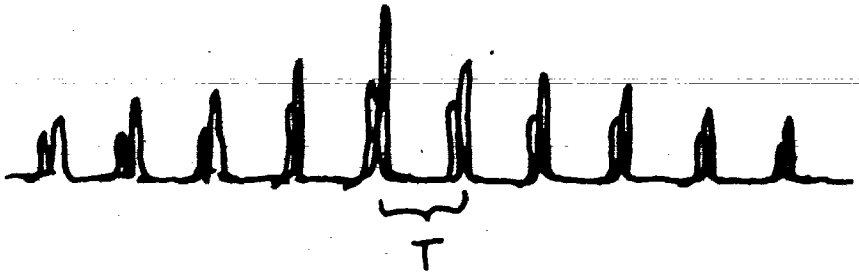

(b)

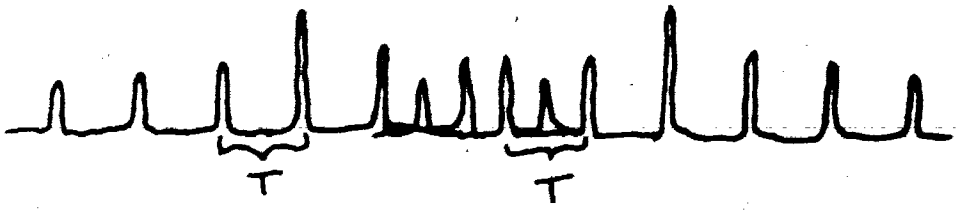

(c)

FIG. 4.2 Nd glass laser output with a cell similar to that of Rentzepis. In (a) there is partial mode locking, (b) multiple pulsing, and (c) excitation of multiple pulse trains.

4-5 ELECTRONIC INSTRUMENTATION

The electronic instrumentation shown in FIG. 3.1 was obtained commercially, with the exception of the gated integrator and associated control circuits which were designed by L. E. Groberman. The integrator was designed with a variable gate to permit integration over the interval 50 nanoseconds to 1 microsecond. For the work in this thesis the gate interval was $\sim$ 320 nanoseconds. The gate was necessary to minimize the high drift rate characteristics of the nanosecond rise time circuitry used in the integrator. The gating function also permitted discrimination against spurious transient voltages. Also, contributions due to the dark current output from the photomultipliers were minimized. Because the time at which a mode locked pulse is produced is unknown to $\sim$ 1 microsecond, it is interesting to note the triggering sequence necessary to ensure that the voltage pulses from the photomultipliers arrive at the gated integrator when the gate is open. A time sequence flow chart is illustrated in FIG. 4.3.

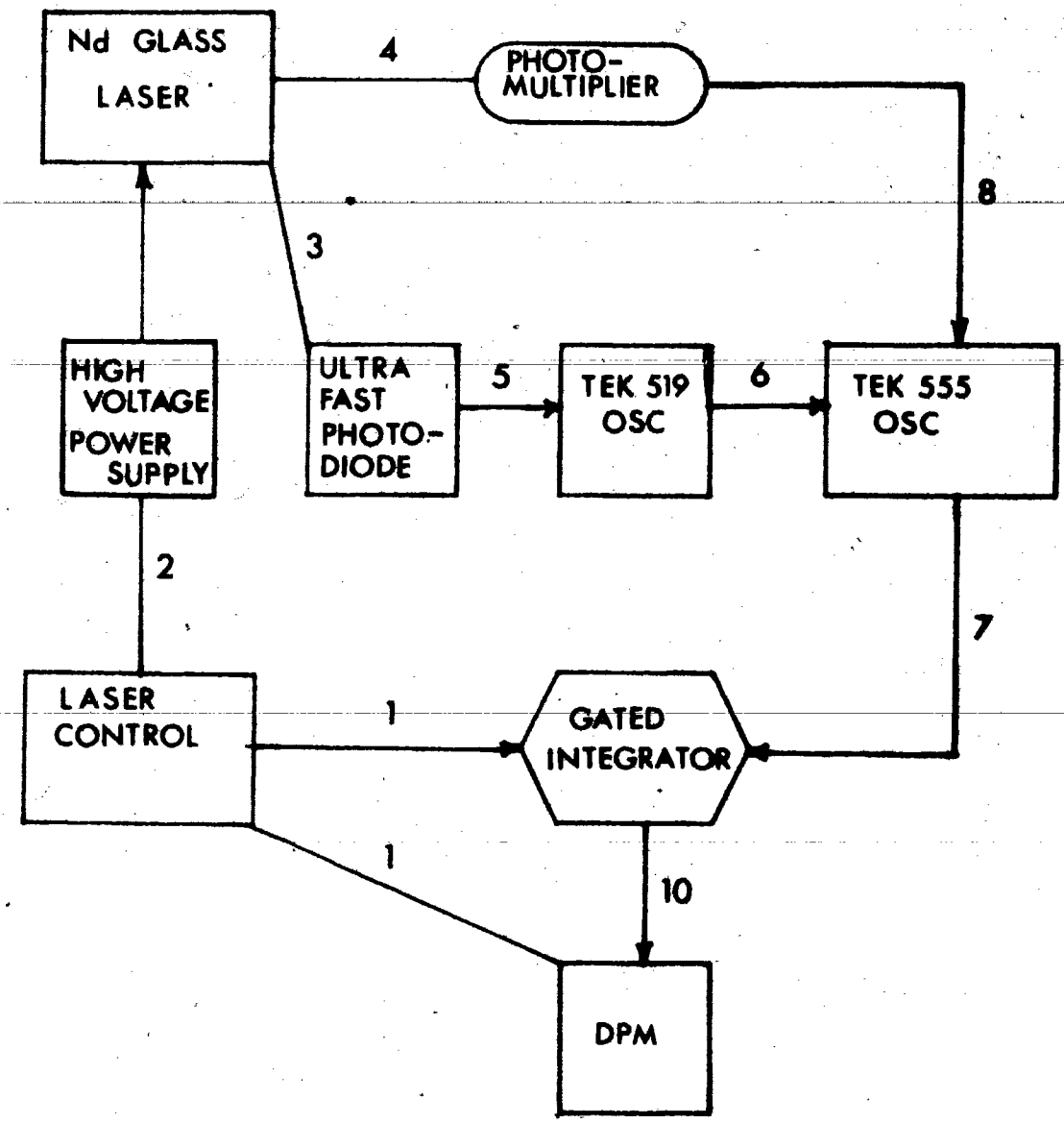

FIG. 4.3 Time sequence flow chart of the electronics.

1. A pulse from the timer in the laser control module sets to zero, the gated integrator and activates read on the DPM. The DPM is a continuous read voltmeter which displays the applied voltage until a hold signal is received.
2. A pulse from the timer in the laser control module initiates the trigger in the high voltage power supply, which results in the discharge of the flashlamp in the laser head.
3. The resulting laser pulse is detected by the ultrafast photodiode.
4. Approximately 3 nanoseconds later, the second harmonic pulse is detected by the photomultiplier.
5. The textronix 519 scope is triggered by the ultrafast photodiode and the simultaneously Q switched and mode locked laser pulse is displayed.
6. The textronix 555 scope is triggered by the 519 scope.
7. A gate pulse from the 555 is used to open the gate of the gated integrator, which may then integrate any signal applied to it. The time

during which the gate remains open is specified by a timer in the integrator which is activated by the gate pulse from the 555.

8. The integrator is reset by the timer.
9. The signal amplified by the 555 is integrated.
10. The gate is closed and the DPM is switched to the hold mode. The integrated signal is then read off the digital panel meter. At the conclusion of the hold mode, step 1 recommences.

The behaviour of the electronics was investigated first by testing the linearity of the integrator and second by examining the spectral characteristics of the two matched EMI 9526 B photomultipliers in conjunction with the integrator.

Firstly, to examine the behaviour of the integrator with respect to pulse size, a Tektronix 115 variable pulse generator and a F-34 function generator were substituted for the Neodymium laser assembly. The F-34 function generator controlled the repetition rate.

The experimental set up is depicted in FIG. 4.4.

Pulses of variable height and width are available from the 115 generator. By recording the DPM (digital panel meter) readings and the corresponding pulse sizes displayed on the Tektronix 555 oscilloscope, one is able to determine if the integrator behaves linearly. The sizes of the pulses were read from the grid of the 555 scope. One square of a pulse within the integrator gate equals one square on the 555 grid.

A typical result is presented in FIG. 4.5. Least squares fits were performed on the data. Each point represents 20 firings. The error bars are not shown in FIG. 4.5. Typically, the error for

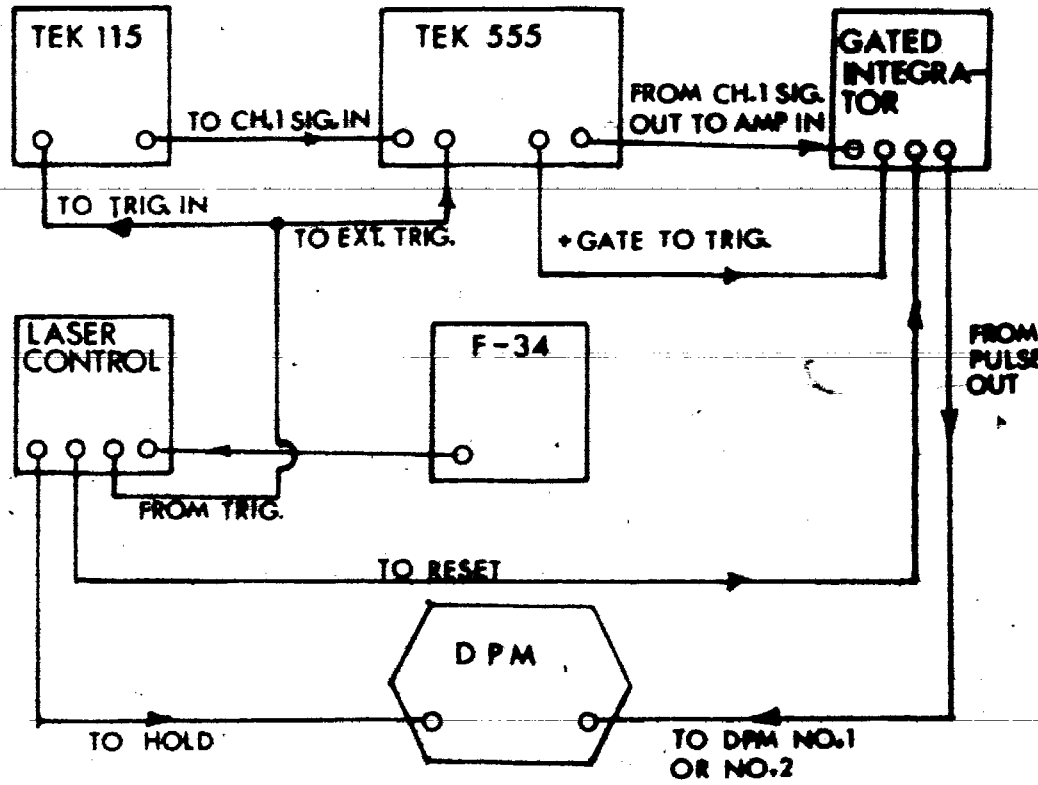

FIG. 4.4 The experimental arrangement for testing the linearity of the electronics.

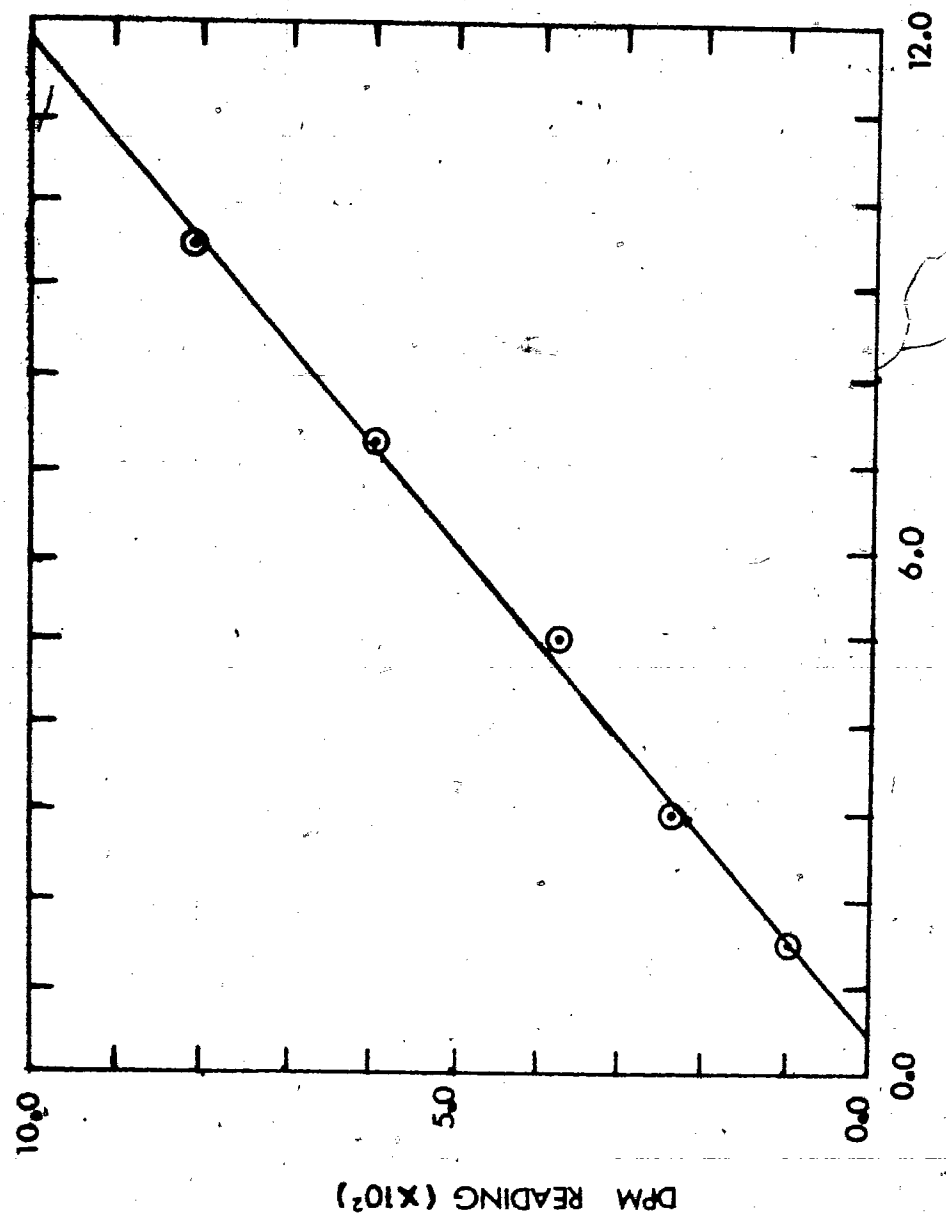

FIG. 4.5 Linearity check of the electronics.
slope= 88.4, y intercept= -41, r^2= 0.99
vertical sensitivity of Tek 555= 0.02 V/cm.

each point was $\pm$ 1%. Final results are tabulated in table 1.

After determining that the integrator integrated linearly with respect to the pulse size, the photomultipliers were inserted into the set up to determine the best photomultiplier operating voltages. A Monsanto MV-5253 green light emitting diode with a peak emitting wavelength of 555 nm. was used as the light source. Neutral density filters were used to vary the intensity. The experimental set up used was the same as for the linearity check, with the only difference being the connecting of the Tek 115 output to the light emitting diode instead of to the Tek 555 oscilloscope. The results for both PM (a) and PM (b) are shown in FIG. 4.6 and FIG. 4.7 which display the DPM reading versus the relative % intensity. The operating voltage at which the output varied linearly with respect to the intensity was the same for both photomultipliers, namely 1050 volts. The error bars are not shown in FIGS. 4.6 and 4.7. Typically, the error for each point was $\sim \pm$ 6%.

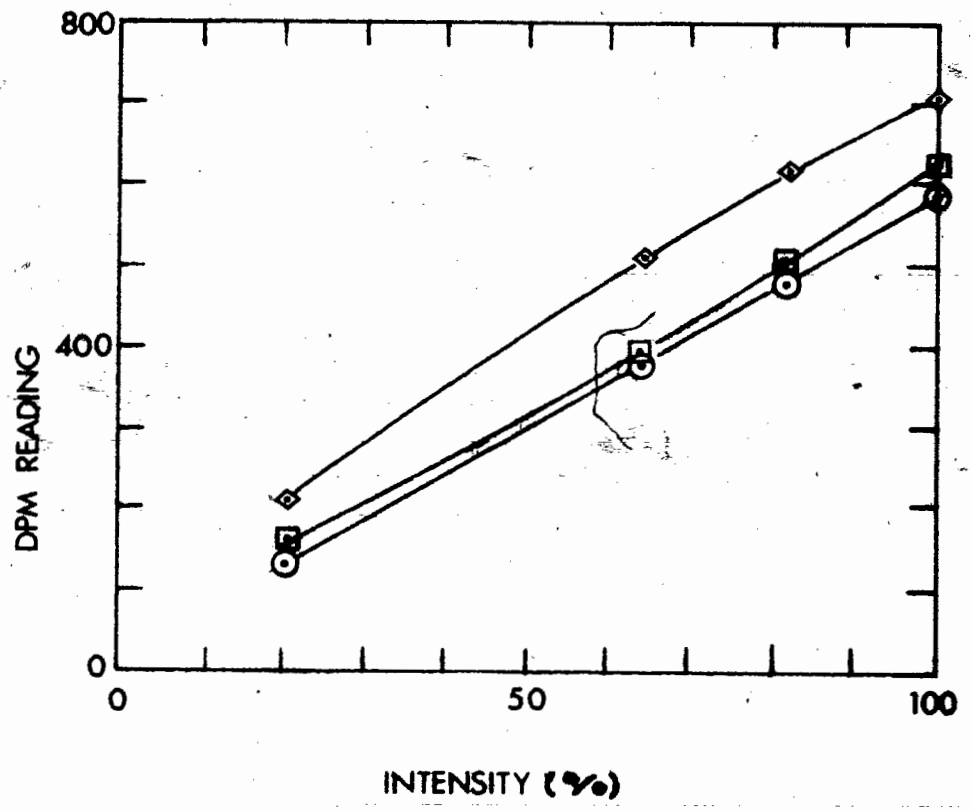

FIG. 4.6 Best operating voltage for PM (a).
◈ 1070 V; ⊡ 1040 V; ⊙ 1050 V.
Vertical sensitivity of Tek 555= 0.01 V/cm.

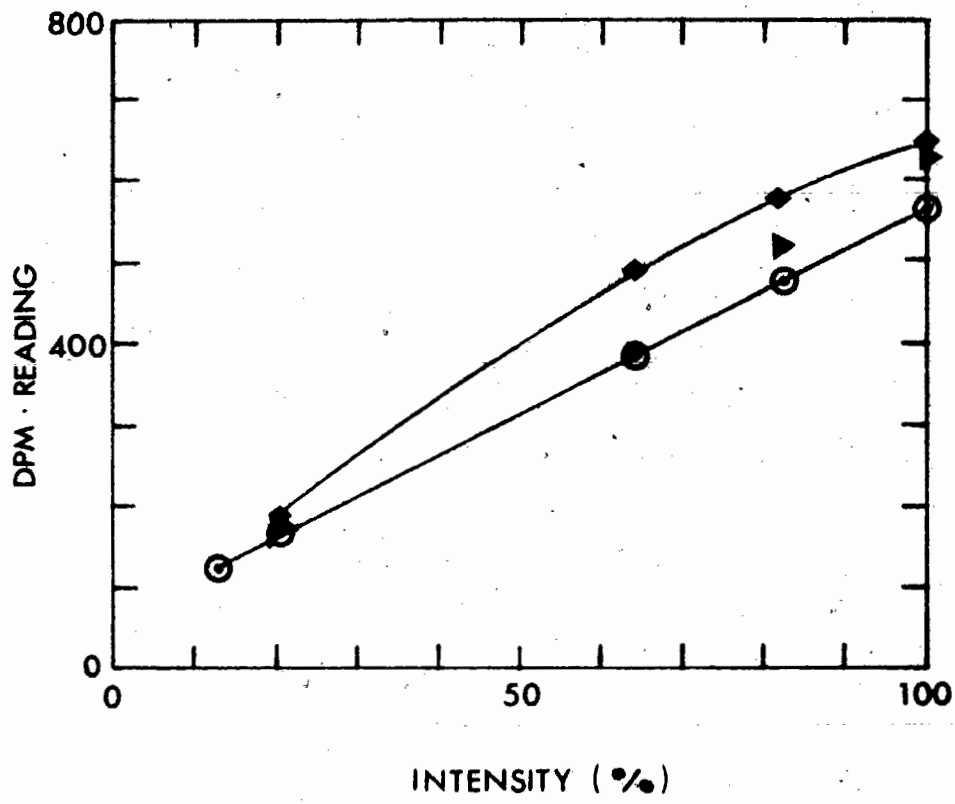

FIG. 4.7 Best operating voltage for PM (b).
◆ 1070 V; ▶ 1020 V; ⊙ 1050 V.
Vertical sensitivity of Tek 555= 0.01 V/cm.

Further testing of the apparatus was made to check the validity of the previous method by generating a SH signal by passing a part of the laser beam through KDP powder to be detected by the photomultiplier. The sizes of the individual pulses displayed on the Tek 555 oscilloscope were measured and the corresponding DPM readings were recorded. Measurements were made for Tek 555 scope vertical amplifier sensitivities of 0.005 V/cm., 0.01 V/cm., and 0.02 V/cm. A typical result is shown in FIG. 4.8. Final results are tabulated in table I, which also includes the data from the linearity check, when the Tek 115 variable pulse generator output was fed directly to the Tek 555 oscilloscope.

These tests provided convincing evidence that the reading of the DPM was linearly proportional to the intensity of the radiation incident on the photomultiplier.

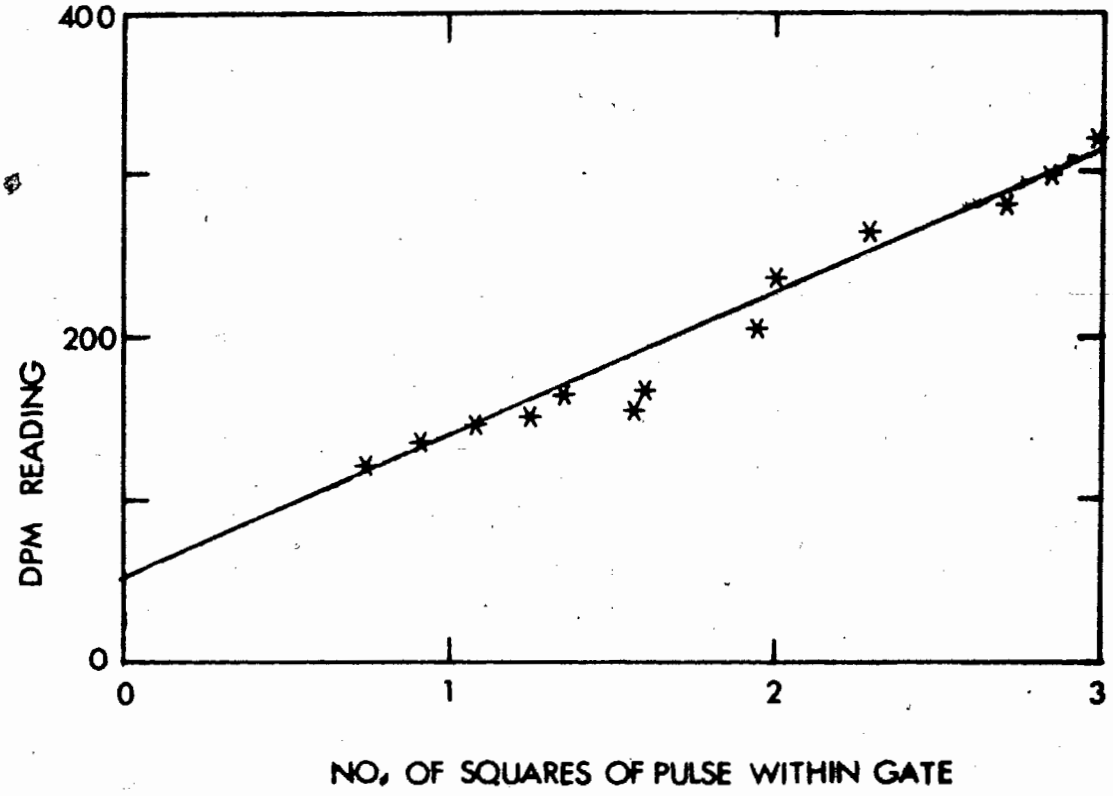

FIG. 4.8 Experimental calibration of integrator using SH signal from KDP powder. Each point represents a single shot. slope=87.9, background=50, r^2=0.98 vertical sensitivity of Tek 555=0.02 V/cm. The solid line represents the least squares fit line.

	PM (b)		PM (a)	
	KDP	115	KDP	115
V.A.S. V/cm.	0.005		0.005	
BG	53		19	
SLOPE	89.9	96.3	87.6	85.6
r^2	0.98		0.98	
V.A.S. V/cm.	0.01		0.01	
BG	62		13	
SLOPE	87.5	89.9	80.6	84.3
r^2	0.99		0.97	
V.A.S. V/cm.	0.02		0.02	
BG	50		8	
SLOPE	87.9	88.4	71.1	86.3
r^2	0.98		0.87	

Table I Results from the linearity check and the KDP (potassium dihydrogen phosphate) powder test. V.A.S. represents the vertical sensitivity of the Tek 555. BG is the background; and r^2 is a measure of the goodness of the least squares fit.

4-6 BAKE OUT PROCEDURE

In order to eliminate adsorbed gases which raise the ultimate pressure, the vacuum system was heated in an asbestos oven. The bake out process lasted five days. The temperature of 200°C was reached 19 hours into the bake out. Nine hours later, the air temperature within the oven was 300°C. The oven was maintained at 370°C or above for 8 hours and at its highest temperature of 395°C for 4 hours on the third day of bake out. The stainless steel dish into which the Hg was eventually distilled, reached a maximum temperature of 250°C. The pressure of the vacuum system before the Hg was distilled was 2.4×10^{-9} torr. Since the expletive deleted vacuum system was determined to be leak proof with a helium gas mass spectrometer leak tester and since previous bake outs had yielded pressures of $\sim 5 \times 10^{-10}$ torr. on two ionization gauges located at different positions in the system, the ionization gauge was thought to be faulty.

4-7 SHG FROM Ag SURFACES

The apparatus was first tested by examining the radiation reflected from Ag and Cu surfaces. Films of Ag and Cu 3000 Å thick were evaporated onto a glass slide. The slide was then inserted

into the vacuum system which was subsequently pumped down without bake out, to a pressure of 2×10^{-7} torr. The transfer procedure, during which the Ag and Cu samples were exposed to the atmosphere, lasted approximately 4 hours. By inserting Monopass narrow band-pass filters, with peak transmittance wavelengths near and away from 531 nm., the second harmonic wavelength, the radiation reflected from Ag was found to be SH radiation. No background radiation was detected. Tests for SH radiation were not made for Cu.

The SHG efficiency was calculated from the experimental data to be $\sim 10^{-13}$, in the following manner. In order to obtain the SH conversion efficiency, the number of SH photons, N_{PM}, incident on the sample photomultiplier was calculated.

$N_{PM}=(N_e)/[(QE)(G)]$

QE is the quantum efficiency of the photomultiplier $\sim 9\%$ at the second harmonic wavelength. G is the gain $\sim 10^6$ of the photomultiplier. N_e is the number of electrons detected and was calculated from

$N_e = Q/e$

where $Q = \int i\, dt = (V/R)\, \Delta t$ and e is the electron charge. The typical operating voltage sensitivity of the

tektronix 555 oscilloscope was 0.01 V/cm. The termination resistance R, leading to the 555 input was 50 Ω. The duration of the integrator gate equal to 320 nsec. was taken to be Δt. Therefore

$$N_{PM} = \frac{(0.01)(320 \times 10^{-9})}{(50)(1.6 \times 10^{-19})(10^{6})(0.09)} = 4.4 \times 10^{3}$$

The number of SH photons produced were

$$N_{SH} = \frac{N_{PM}}{F} = \frac{4.4 \times 10^{3}}{0.032} = 1.4 \times 10^{5}$$

F is the attenuation factor due to the filters used. The number of fundamental photons incident on the sample was

$$N_{F} = \frac{\text{no. of individual pulses X energy per pulse}}{\text{energy per photon}}$$

The number of individual pulses was estimated to be the duration of the integrator gate divided by the cavity round trip time. The energy per pulse was calculated to be the peak power $\sim 1 \times 10^{9}$ watt times the temporal width $\sim 5 \times 10^{-12}$ sec.[16] of the pulses. An error in the peak power or the temporal width of the pulses by an order of magnitude would not affect the results because of the normalization technique used by generating a reference SH signal.

The energy of a photon at the fundamental wavelength 1062.3 nm. is 1.88×10^{-19} joule. Therefore

$$N_F = \frac{(320 \times 10^{-9})(5 \times 10^{-12})(10^9)}{(7.5 \times 10^{-9})(1.88 \times 10^{-19})} = 1.13 \times 10^{18}$$

The SH conversion efficiency was

$$CE = \frac{N_{SH}}{N_F} = \frac{1.4 \times 10^5}{1.13 \times 10^{18}} = 1.2 \times 10^{-13} \sim 10^{-13}$$

The polarization dependence of the radiation reflected from the Ag and Cu surfaces was investigated at angles of incidence 70° and 60°, and three polarization angles of the incident beam 0°, 45°, and 90° with respect to the plane of incidence. The results for Ag are presented in FIGS. 4.9.

In FIG. 4.9 (a), the R.S.H.I. (relative second harmonic intensity) is plotted as a function of the analyzer angle for an angle of incidence $\theta = 70^\circ$. The incident beam was polarized in the plane of incidence ($\phi = 0^\circ$). The R.S.H.I. was calculated from

$$\text{R.S.H.I.} = \frac{DPM(b)}{DPM(a)} \times \frac{555\ SENS(b)}{555\ SENS(a)} \times \frac{SLOPE(b)}{SLOPE(a)} \times \frac{FIL(a)}{FIL(b)}$$

DPM(a) and DPM(b) are the digital panel meter readings minus the backgrounds. The letters a and b denote the reference and sample SH radiation respectively. SENS is the vertical sensitivity of the amplifier of the 555 oscilloscope to which a SH signal was fed. SLOPE represents the slope of the SH detection system for a particular 555 vertical sensitivity determined earlier in section 4-4, and FIL is the attenuation

factor due to the filters used. The instrumental contribution to error in R.S.H.I. is 20% and is not included in the error bars indicated in FIG. 4.9 (a) and subsequent graphs. Including the instrumental contribution, the error for each point was typically $\pm$ 21%. Each point represents the average of at least 15 shots. The error bar indicates σ_m, the standard error in the mean which is given by

$$\sigma_m \sim S/n^{1/2} \quad (24)$$

where n is the number of measurements made and S is the adjusted root mean square deviation given by

$$S = (n/n-1)^{1/2} \sigma_{rms}$$

where σ_{rms} is the root mean square deviation. For example, for the typical result indicated in FIG. 4.9 (a), S= $\pm$ 21%, n=15, and σ_m= $\pm$ 5%. Since the number of SH photons incident on the sample photomultiplier was calculated to be greater than 10^3, the fluctuations due to the performance of the photomultipliers were small. The relative magnitude of the rms deviation to the mean decreases as $n^{-1/2}$.(25) For n= 4.4 X 10^3, $n^{1/2}$ is 0.02. The large values of S indicate that in the 15 sec. interval between shots, the Ag surface maintained at 2 X 10^{-7} torr. may have changed in a non-reproducible fashion due to adsorbed

gases. Although the incident power density was high, no visual evidence of damage to the Ag and Cu surfaces was observed.

As discussed in chapter 2, the p component of the SH radiation which corresponds to an analyzer setting of 0° or 180°, is expected to be larger than the s component, which corresponds to an analyzer angle of 90°, for all angles of incidence and polarization angles of the incident beam. Therefore the functional dependence of the curve for the SH light exiting from the polarizer/analyzer configuration was seen to be correct in FIG. 4.9 (a). However, contrary to theory, the s component was non-zero. Preventive measures were taken so that the non-zero reading at the analyzer angle of 90° was not due to a light leak. Moreover, the determinations of the orientations relative to the sample surface, of the transmission axes of the polarizer and analyzer, and the fast and slow axes of the quartz $\lambda/2$ plate were sufficiently accurate not to produce the observed effect.

Least squares fits were performed on the data. The solid lines in FIGS. 4.9 represent least squares fit lines. See appendix 1.

$I_p \propto E_p^2$, which is the p component of the detected

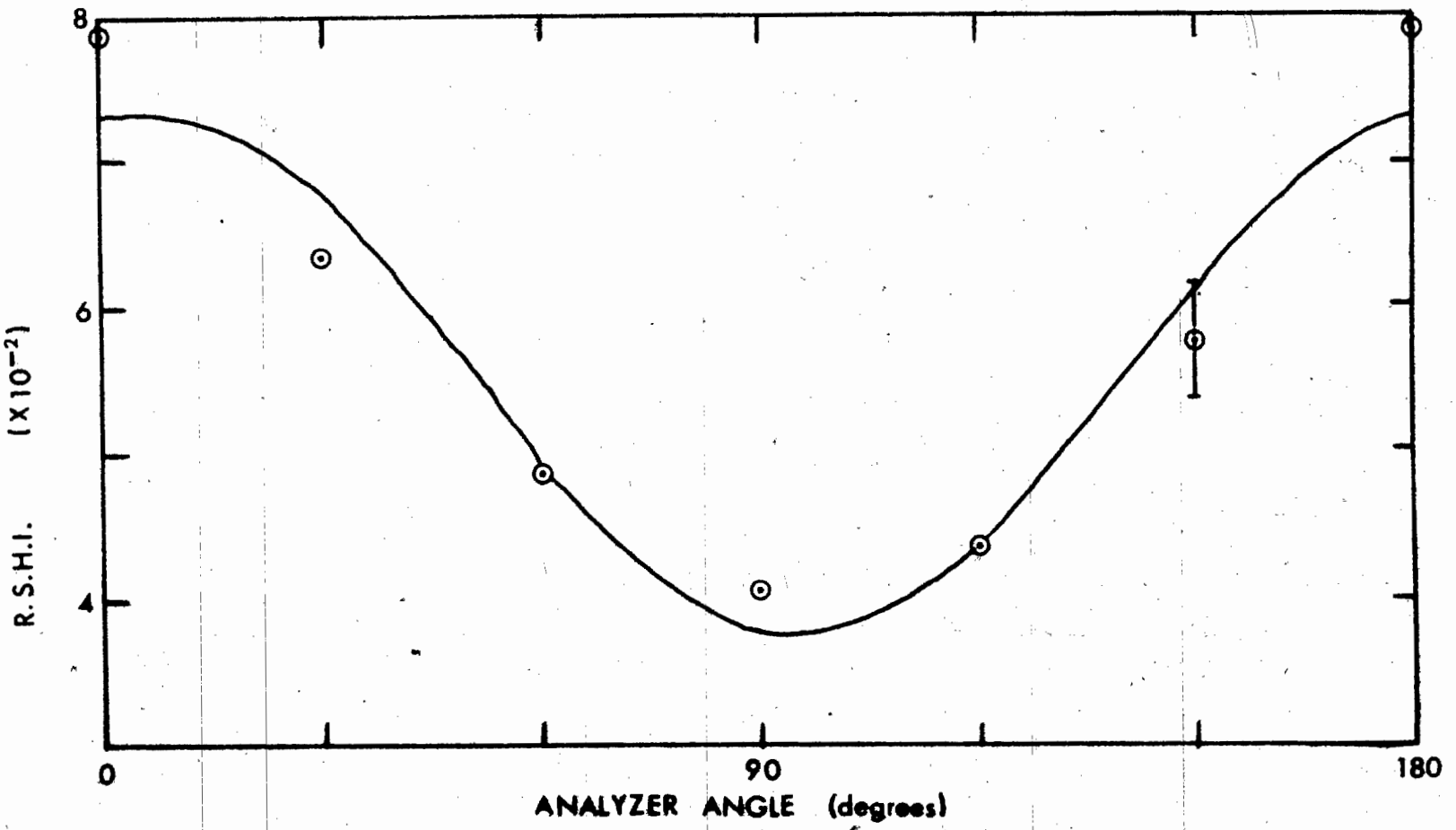

FIG. 4.9 (a) Polarization dependence of SH radiation from Ag. The relative second harmonic intensity is plotted as a function of the analyzer angle. $\theta = 70° \pm 1°$; $I_p = 7.32 \times 10^{-2}$; $I_s = 3.77 \times 10^{-2}$; $\phi = 0°$; $\theta_o = +6°$.

radiation whose value was determined from the least squares fit of the data. $I_s \propto E_s^2$, which is the s component of the radiation detected. θ_o is a measure of the ellipticity of the radiation detected. Typical error bars for I_p and I_s were approximately the same as $\sigma_m \sim \pm 5\%$, the standard error in the mean for each point.

In FIGS. 4.9 (b) and 4.9 (c), the results at $\theta = 70^\circ$, and $\phi = 45^\circ$ and 90° are presented. Contrary to theory, I_s was larger than I_p in each case. Theory also predicts that for an incident beam polarized perpendicular ($\phi = 90^\circ$) or parallel ($\phi = 0^\circ$) to the plane of incidence, no SH radiation I_s, oscillating perpendicular to the plane of incidence is generated. I_s was non-zero for both p and s polarized incident radiation.

The measurements were repeated at $\theta = 60^\circ$ to test the reproducibility of the results. As can be seen in FIGS. 4.9 (d), 4.9 (e), and 4.9 (f), I_p was greater than I_s for a p polarized incident beam. When the incident radiation contained an s component ($\phi = 45^\circ$ and 90°), I_s was greater than I_p. The observed behaviour of the SH radiation, excluding the magnitudes of the R.S.H.I.,

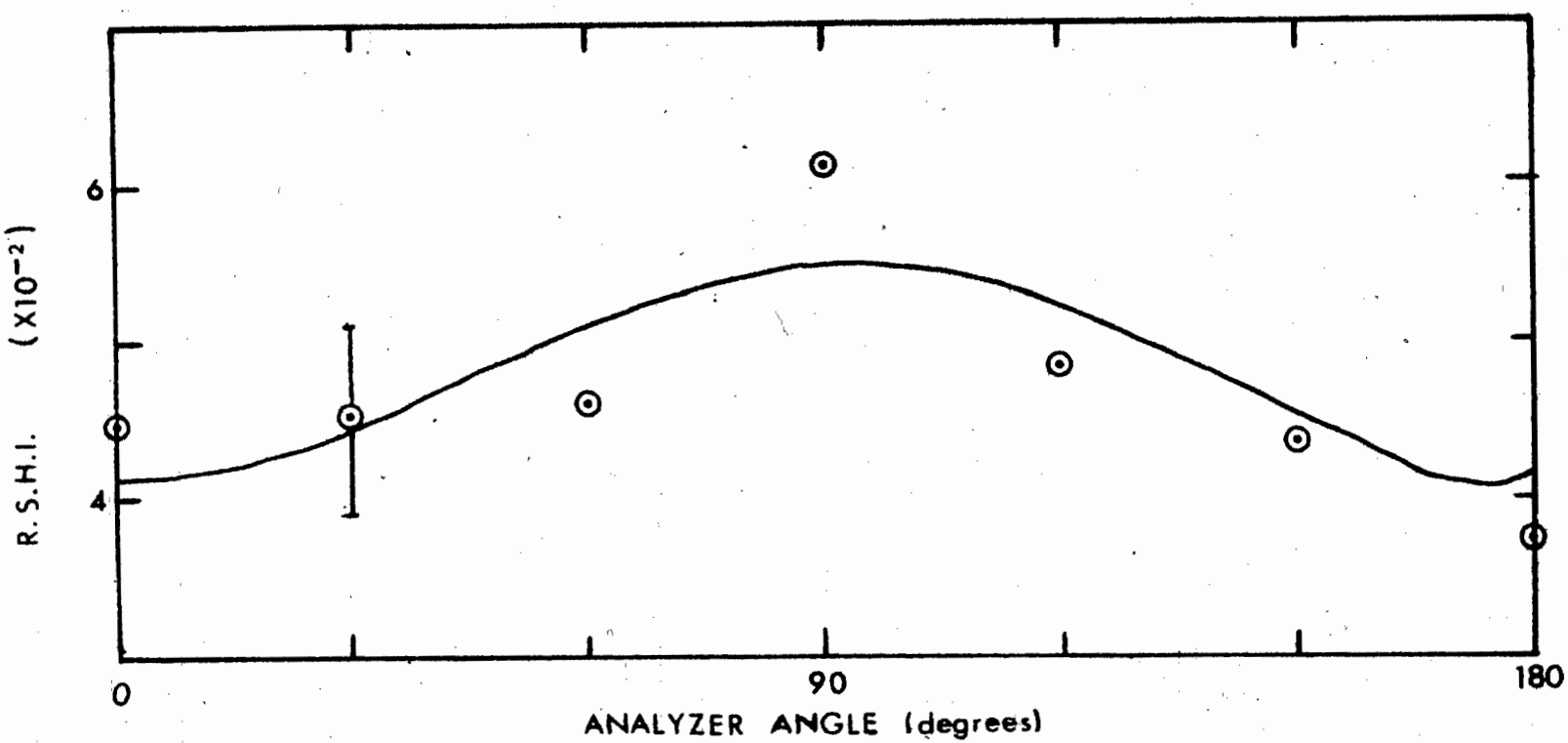

FIG. 4.9 (b) Polarization dependence of the SH radiation from Ag. The relative second harmonic intensity is plotted as a function of the analyzer angle. $\theta = 70° \pm 1°$; $\phi = 45°$; $I_p = 3.14 \times 10^{-2}$; $I_s = 4,45 \times 10^{-2}$; $\theta_o = +2°$.

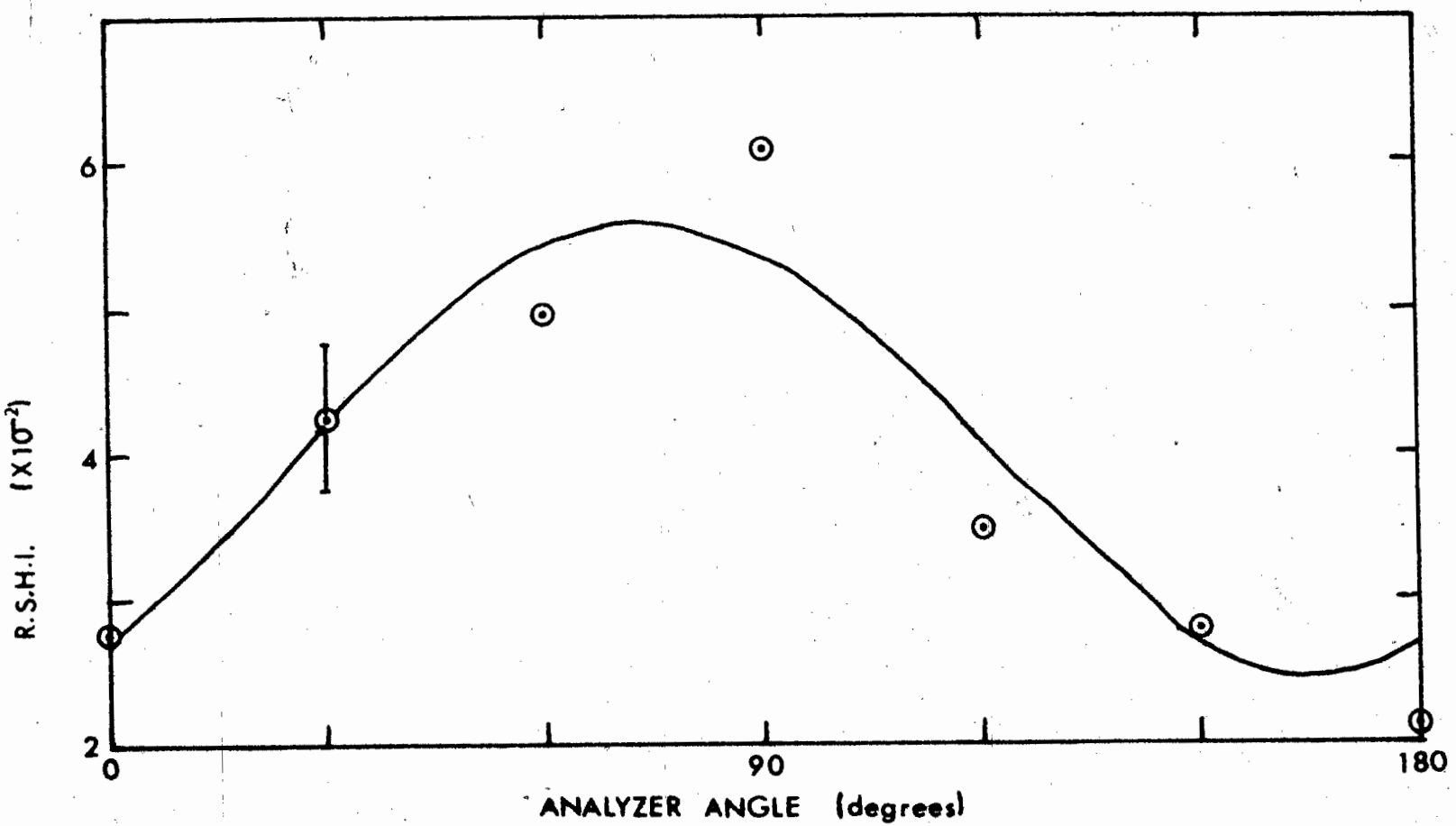

FIG. 4.9 (c) Polarization curve for the SH radiation from Ag. The relative second harmonic intensity is plotted as a function of the analyzer angle.
$\theta = 70^{o} \pm 1^{o}$; $\phi = 90^{o}$; $I_p = 2.73 \times 10^{-2}$; $I_s = 5.37 \times 10^{-2}$; $\theta_o = -16^{o}$.

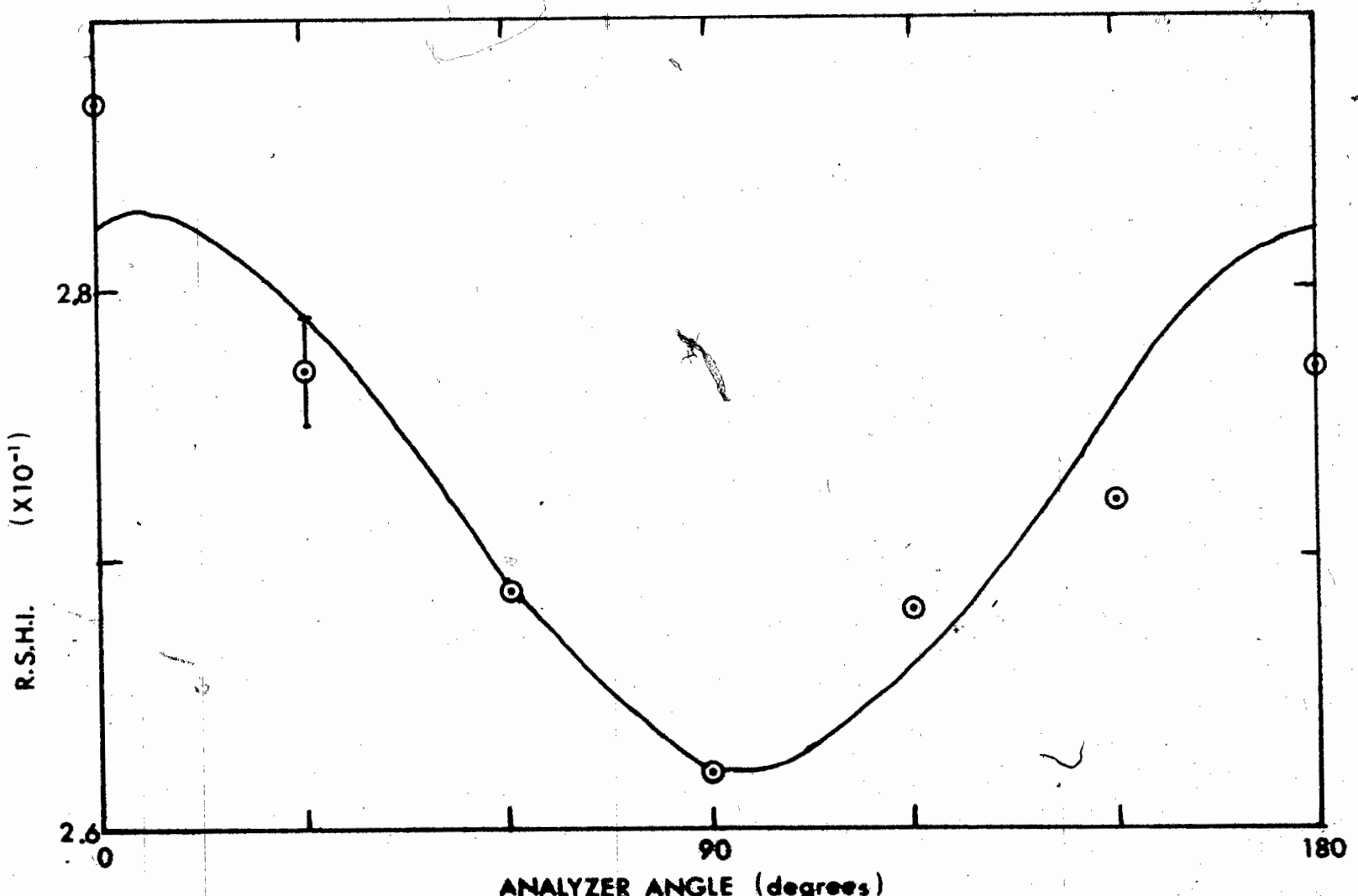

FIG. 4.9 (d) Polarization dependence of SH radiation from Ag. The relative second harmonic intensity is plotted as a function of the analyzer angle. $\theta = 60^{o} \pm 1^{o}$; $\phi = 0^{o}$; $I_p = 2.82 \times 10^{-1}$; $I_s = 2.62 \times 10^{-1}$; $\theta_o = +6^{o}$.

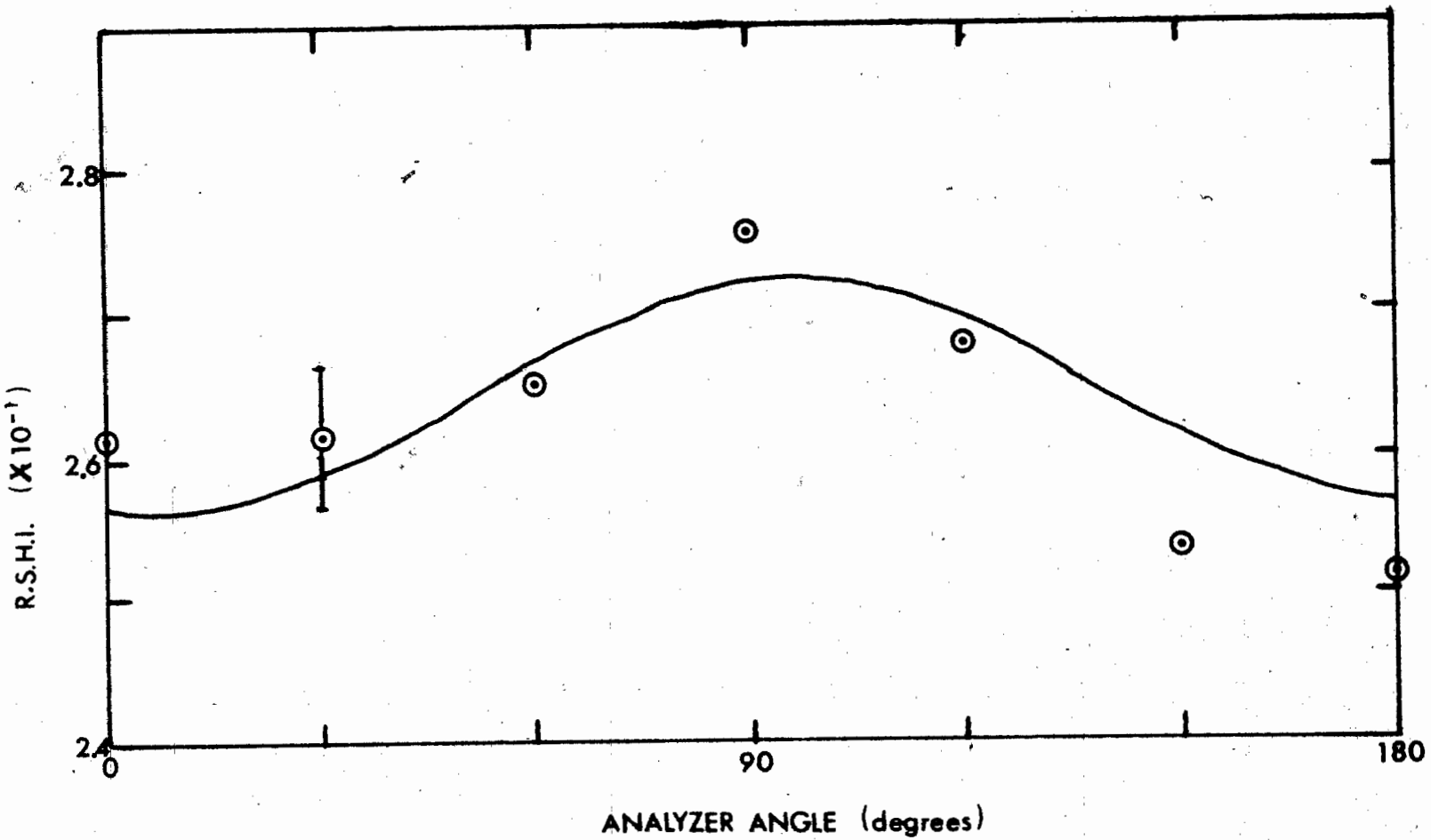

FIG. 4.9 (e) Polarization dependence of SH radiation from Ag. The relative second harmonic intensity is plotted as a function of the analyzer angle. $\theta=60^{\circ}\pm1^{\circ}$, $\phi=45^{\circ}$; $I_p=2.67 \times 10^{-1}$; $I_s=2.72 \times 10^{-1}$; $\theta_o = +6^{\circ}$.

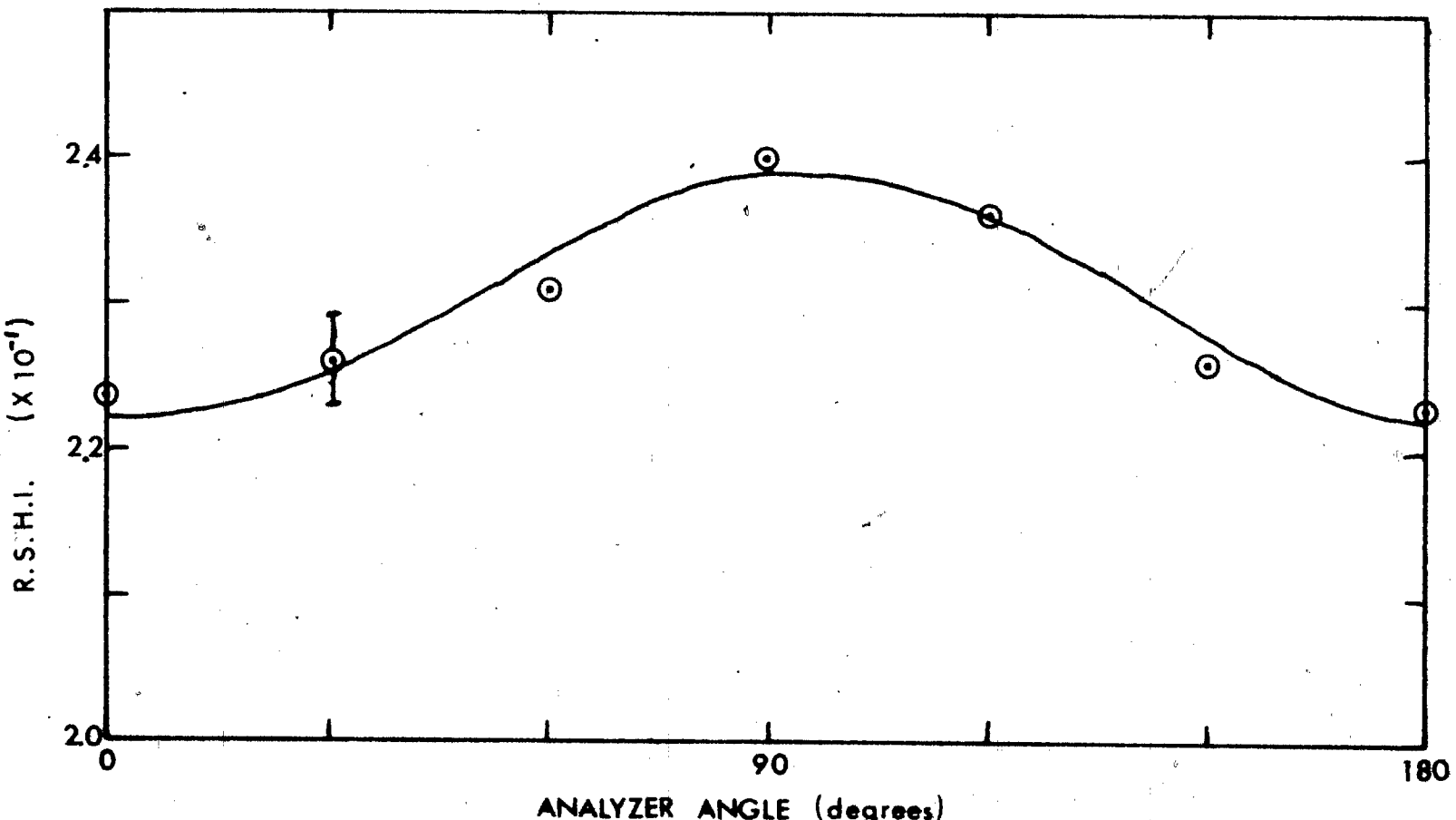

FIG. 4.9 (f) Polarization dependence of SH radiation from Ag. The relative second harmonic intensity is plotted as a function of the analyzer angle. $\theta=60^{o}\pm1^{o}$; $\phi=90^{o}$; $I_p=2.22 \times 10^{-1}$; $I_s=2.39 \times 10^{-1}$; $\theta_o=+6^{o}$.

was essentially the same at both angles of incidence. The results are discussed further in chapter 5.

The results for Cu, not presented graphically in this thesis were similar. For a p polarized incident beam, I_p was greater than I_s. When the incident beam contained an s component (ϕ=45° and 90°), I_s was greater than I_p. For both p and s polarized incident beams, I_s was non-zero. However, tests were not made to confirm that the radiation detected was SH radiation.

4-8 SHG INVESTIGATION OF LIQUID Hg

Investigations of SHG from liquid Hg surfaces were performed at angles of incidence θ in order, 60°, 74°, 76°, and 78°. A fresh Hg surface was distilled at each angle of incidence. Space limitations did not allow studies below 60° and above 78°. Tests for SH radiation were made by inserting Monopass narrow bandpass filters with peak transmission wavelengths in the range 438 nm. to 591 nm. in front of photomultiplier (b), the sample photomultiplier.

At θ= 60°, tests for SH radiation were made at two liquid Hg temperatures, 26°C and 11°C. The results are presented in FIG. 4.10. The incident radiation was p polarized and the analyzer was set

to select the p component of the radiation reflected from the sample. The relative intensity (R.I.) was calculated in the same manner as the R.S.H.I. (relative second harmonic intensity) in the previous section. No pronounced peaks in R.I. were observed at 531 nm., the second harmonic wavelength.

The R.I. decreased as the size of the incident beam projected on the Hg surface was increased from 0.3 cm^2 to 0.9 cm^2, with double concave lenses of focal lengths in the range -15 cm. to -30 cm. Since the threefold increase in the beam size did not enhance the R.I. at the SH wavelength, no further reduction in the incident power density was made.

The results have not been normalized with respect to the spectral response of the SH detector photomultiplier. With the additional normalizing factor included, the R.I. increases as the wavelength increases. It was concluded that background radiation was dominant for the light reflected from liquid Hg surfaces at $\theta = 60^{\circ}$.

At $\theta = 74^{\circ}$, tests for SH radiation were made at two liquid Hg temperatures of $20^{\circ}C$ and $-24^{\circ}C$. The R.I. did not peak at the second harmonic wavelength as shown in FIGS. 4.11 (a) and 4.11 (b).

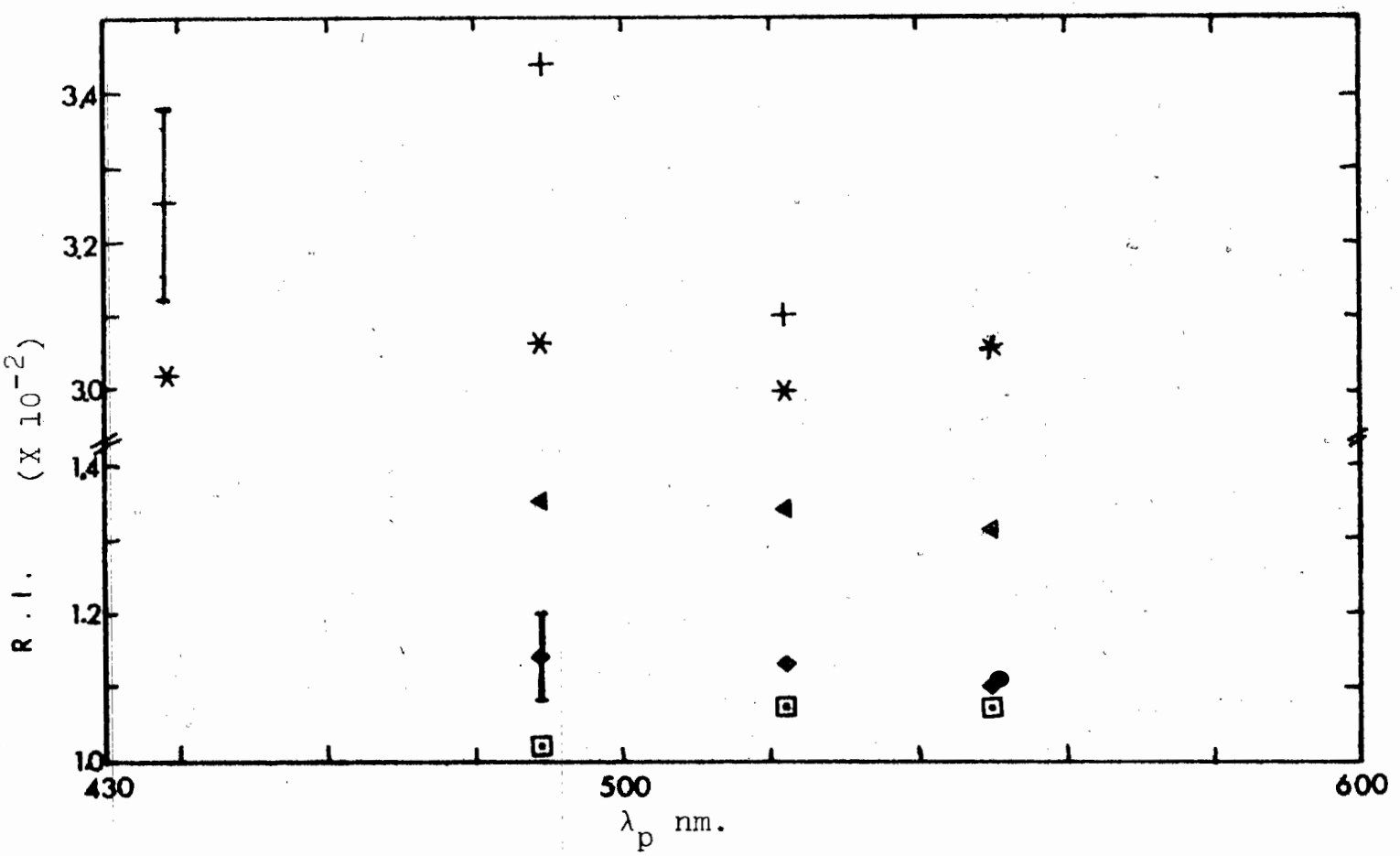

FIG. 4.10 Tests for SH radiation from solid and liquid Hg. The relative intensity is plotted as a function of the peak transmission wavelength of the narrow bandpass filter. $\theta=60^\circ \pm 1^\circ$; $\phi=0^\circ$; + temp=11° C ± 1° C; * temp= -40° C ± 10° C, beam size=0.9 cm^2; temp= 26° C ± 1° C, ⊡ beam size=0.9 cm^2, ◆ beam size=0.8 cm^2, ◀ beam size =0.3 cm^2 Typical error bars are shown.

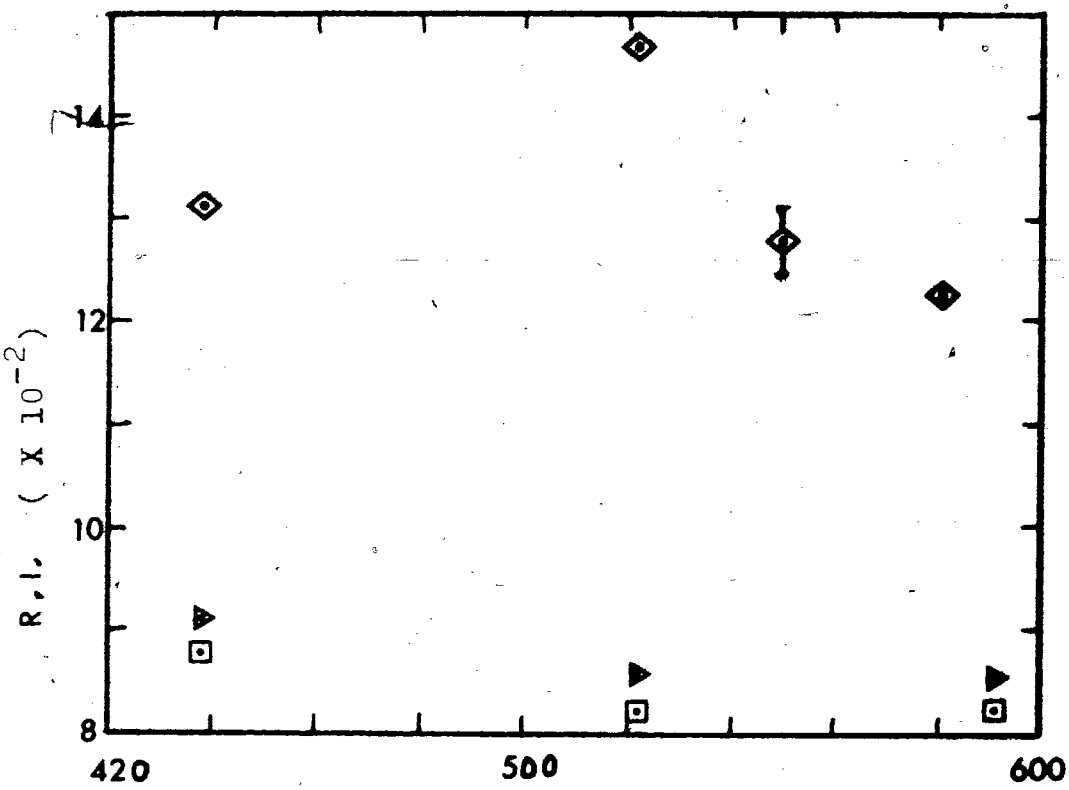

FIG. 4.11 (a) Tests for SH radiation from liquid Hg. The relative intensity is plotted against λ_p. $\theta = 74^\circ \pm 1^\circ$; temperature= 20 C $\pm$ 1 C; ◈ $\phi = 0^\circ$; ▶ $\phi = 45^\circ$; ⊡ $\phi = 90^\circ$. The R.I. has not been normalized with respect to the spectral response of the photomultiplier.

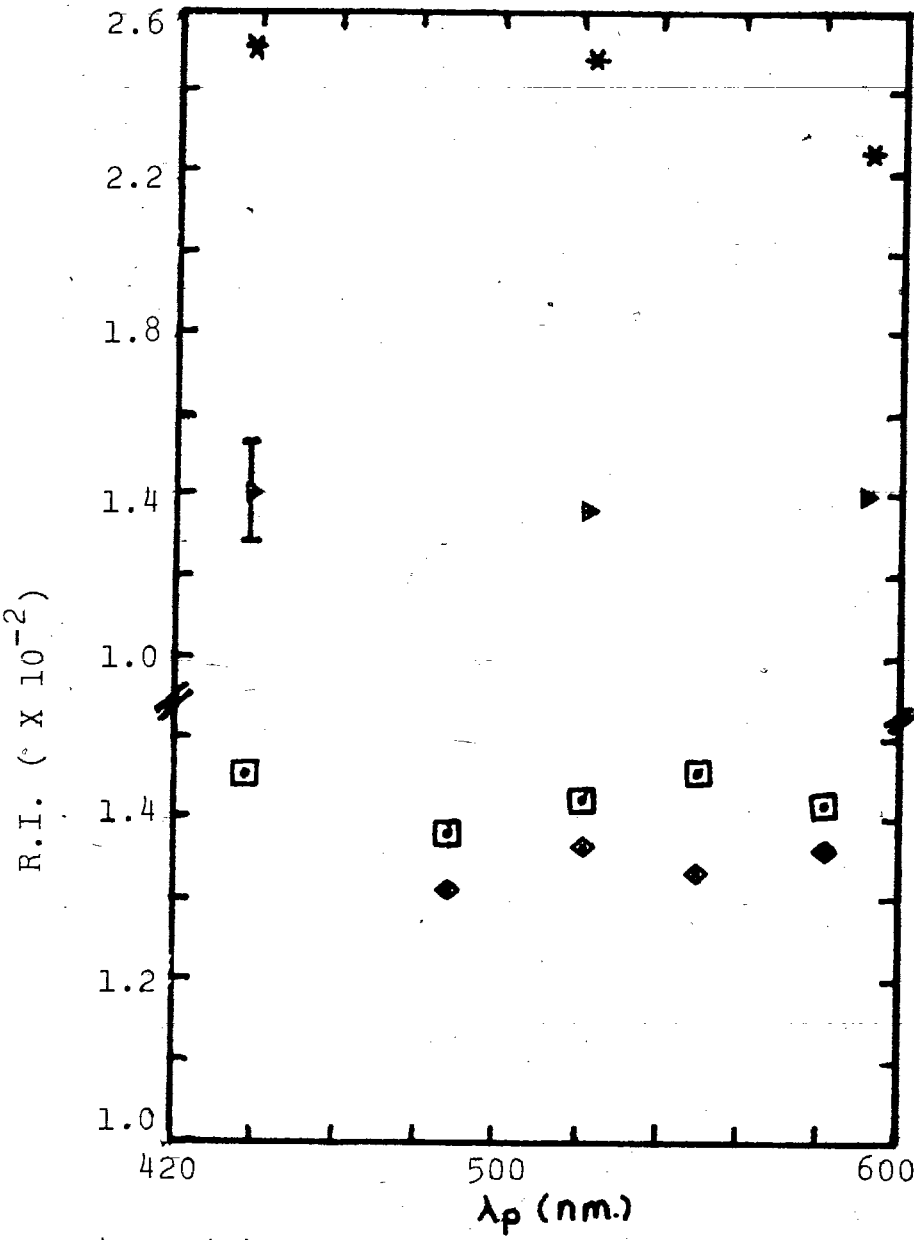

FIG. 4.11 (b) Tests for SH radiation from liquid and solid Hg. The R.I. is plotted against λ_p. $\theta = 74^\circ \pm 1^\circ$; temp.$= -24^\circ \pm 2^\circ$C, * $\phi = 0^\circ$, ▶ $\phi = 45^\circ$; temp.$= -91^\circ$C $\pm$ 16°C, ▣ $\phi = 0^\circ$; temp.$= -53^\circ$C $\pm$ 12°C, ◆ $\phi = 0^\circ$. The R.I. has not been normalized with respect to the spectral response of the photomultiplier.

SHG theories predict the SHG efficiency to decrease as the polarization angle of the incident radiation is changed from $\phi = 0^{\circ}$ to 90°. Therefore, the tests for SH radiation at $\theta = 74^{\circ}$ from liquid Hg suggest the generation of SH radiation as well as background radiation. Polarization studies were made at $\theta = 74^{\circ}$ and the results are presented in FIGS. 4.12 (a) and 4.12 (b). The R.I. is plotted as a function of the analyzer angle. The R.I. was found to be essentially constant as the analyzer angle was varied from 0° to 180°. Therefore the generation of background radiation dominated the generation of SH radiation.

No radiation was detected from liquid Hg at angles of incidence $\theta = 76^{\circ}$ and 78° when Monopass narrow bandpass filters were inserted in front of PM (b), the sample photomultiplier.

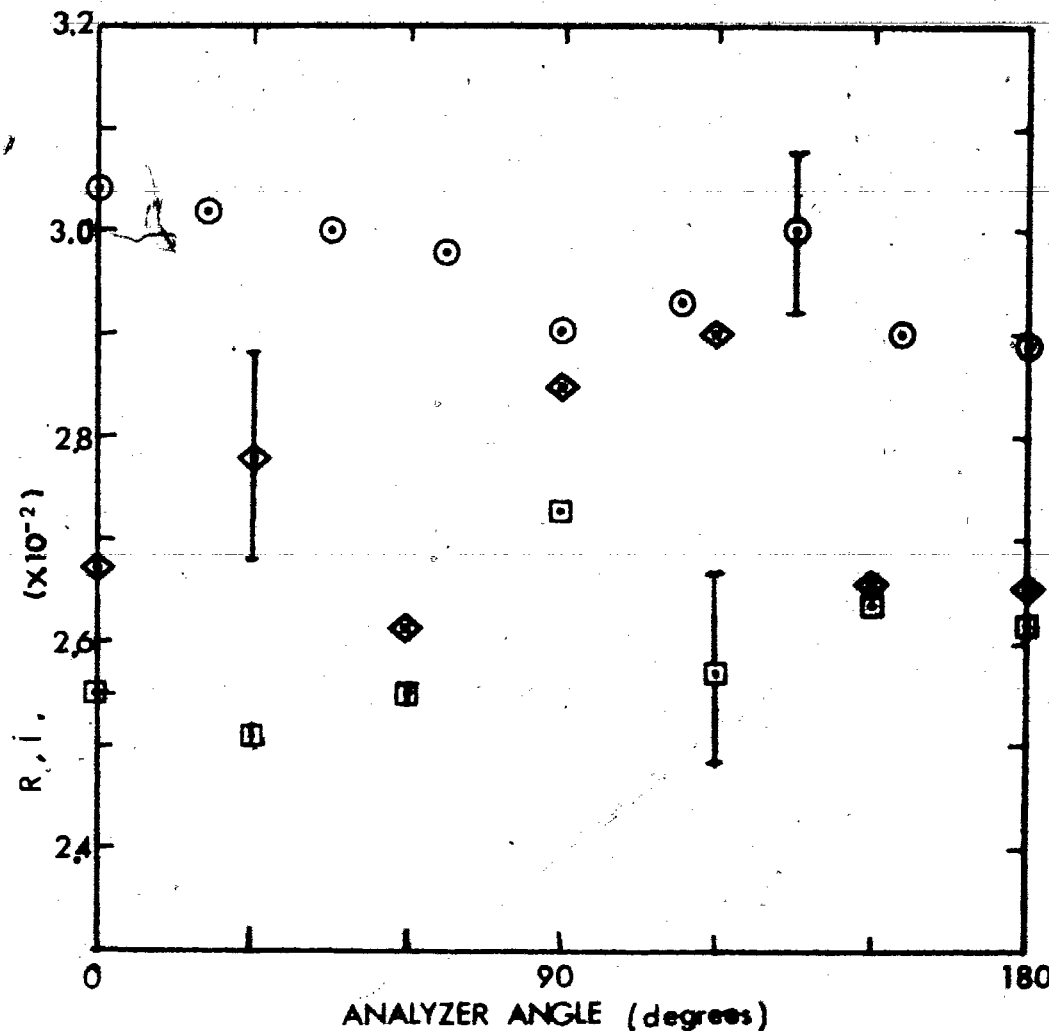

FIG. 4.12 (a) Polarization dependence of the light reflected from liquid Hg.
$\theta = 74^{\circ} \pm 1^{\circ}$; temperature= $20^{\circ}C \pm 1^{\circ}C$;
⊙ $\phi = 0^{\circ}$; ◈ $\phi = 45^{\circ}$; ⊡ $\phi = 90^{\circ}$.

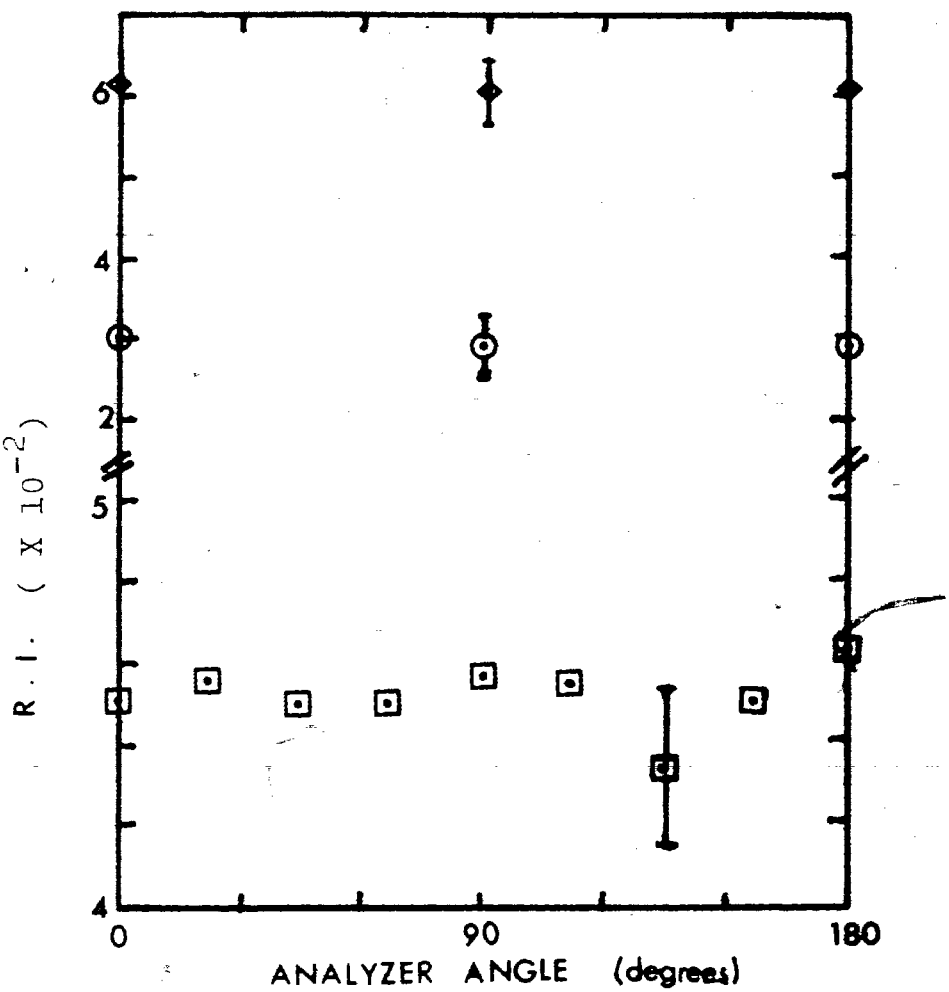

FIG. 4.12 (b) Polarization dependence of the light reflected from liquid and solid Hg. The relative intensity is plotted against the analyzer angle.
$\theta = 74^{\circ} \pm 1^{\circ}$; temperature= $-24^{\circ}C \pm 2^{\circ}C$,
◈ $\phi = 0^{\circ}$; ⊙ $\phi = 45^{\circ}$;
temperature= $-91^{\circ}C \pm 16^{\circ}C$, ⊡ $\phi = 90^{\circ}$.

4-9 SHG INVESTIGATION OF SOLID Hg

The light reflected from solid Hg surfaces was examined at angles of incidence in order 60°, 74°, 76°, 78°, and 71°.

At $\theta = 60^{\circ}$, tests for SH radiation were made at temperatures of $-40^{\circ}C \pm 10^{\circ}C$ and $-131^{\circ}C \pm 1^{\circ}C$. The results were similar to those for liquid Hg at the same angle of incidence in that the R.I. did not peak at second harmonic wavelength of 531 nm. The results are shown in FIGS. 4.10 and 4.13.

The radiation detected from solid Hg surfaces at $\theta = 74^{\circ}$ at temperatures of $-53^{\circ}C$ and $-91^{\circ}C$ was found to consist of background radiation of broad spectral width as shown in FIG. 4.11 (b).

Polarization studies made at $\theta = 74^{\circ}$ and at a temperature of $-91^{\circ}C \pm 16^{\circ}C$ revealed the radiation detected from solid Hg to be unpolarized. The results are shown in FIG. 4.12 (b). Therefore the radiation detected from solid Hg was dominated by background radiation as suggested by the results for tests for SH radiation.

The tests for SH radiation from solid Hg surfaces (at all solid Hg temperatures) revealed the existence of a peak in the R.I. near the SH wavelength at $\theta = 76^{\circ}$

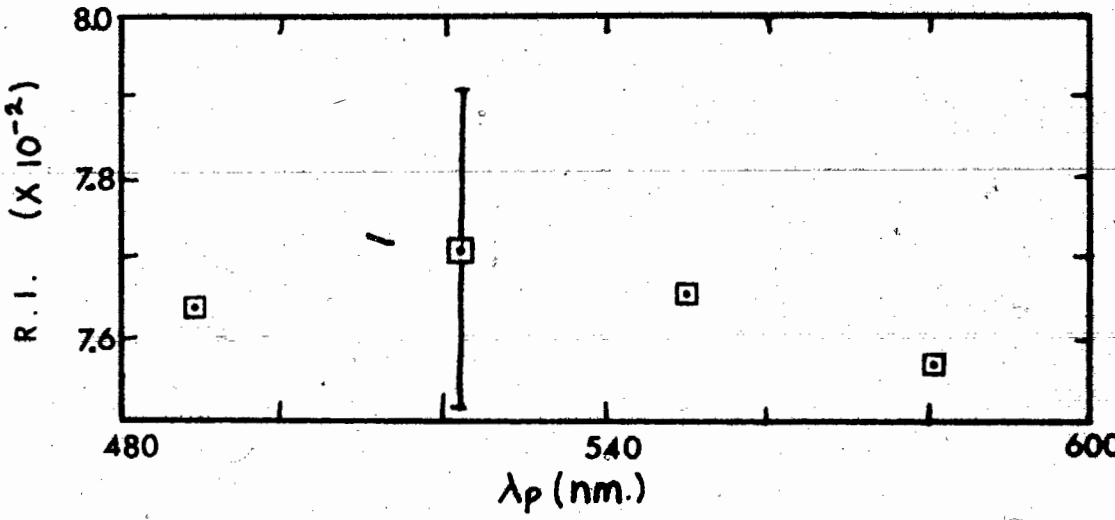

FIG. 4.13 Tests for SH radiation from solid Hg. The relative intensity is plotted as a function of the peak transmission wavelength of the narrow bandpass filter used.
$\theta = 60^{\circ} \pm 1^{\circ}$, $\phi = 0^{\circ}$, temperature= $-131^{\circ}C \pm 1^{\circ}C$., beam size= 0.9 cm^2.

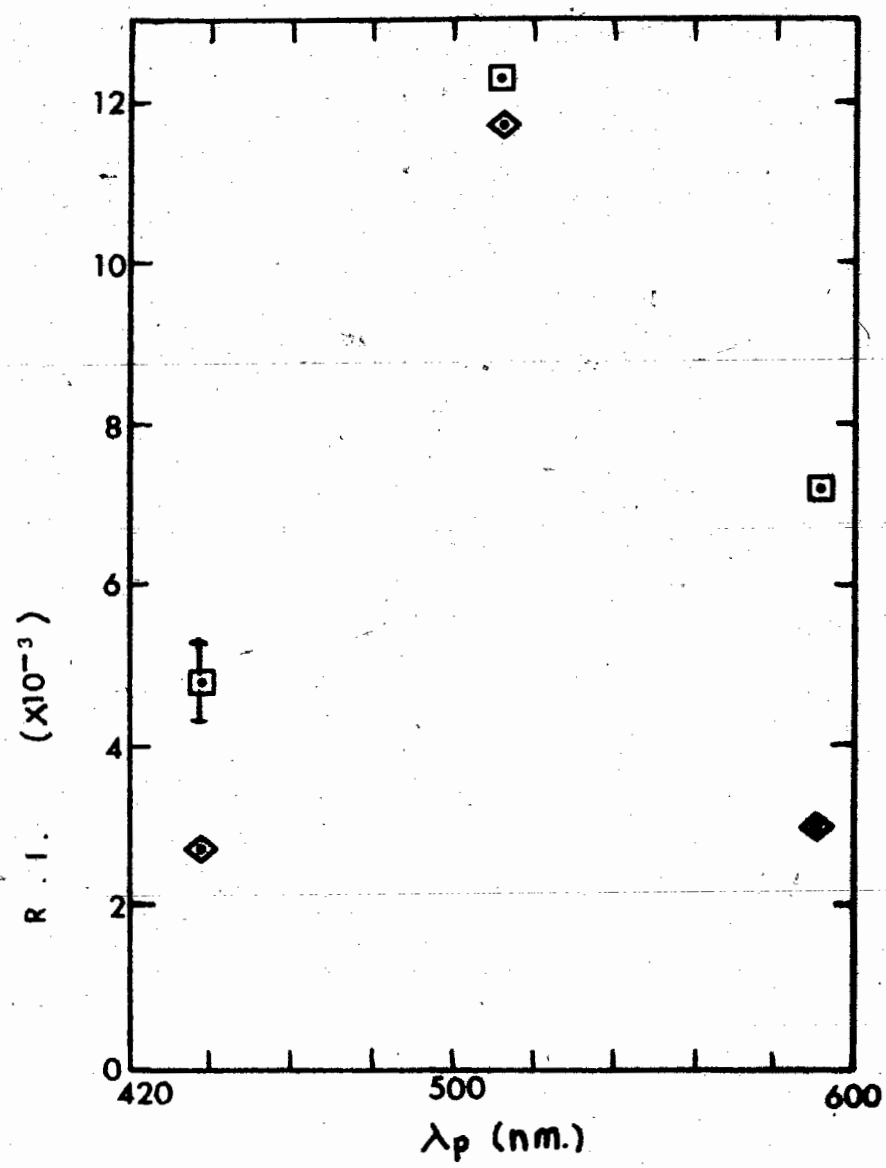

FIG. 4.14 Tests for SH radiation from solid Hg. The relative intensity is plotted against the peak transmission wavelength of the Monopass filter used.

$\theta = 76^{\circ} \pm 1^{\circ}$; temperature = $-79^{\circ}C \pm 10^{\circ}C$;

⊡ $\phi = 0^{\circ}$; ◈ $\phi = 45^{\circ}$.

as shown in FIG. 4.14. However, as at $\theta = 60^{\circ}$ and 74°, the inclusion of the spectral response of the photomultiplier in normalizing the R.I. leads to rise in the R.I. as the wavelength increased.

Polarization curves for incident radiation polarized at $\phi = 0^{\circ}$ and 45° with respect to the plane of incidence, are presented in FIGS. 4.15 (a) and 4.15 (b). In both cases, the R.I. at the analyzer angles of 0° and 180° were greater than the R.I. at 90° in accordance with SHG theory. However, contrary to SHG theory, the R.I. at the analyzer angle of 90° was non-zero. No signal was detected for incident beams polarized perpendicular to the palne of incidence for any analyzer angle.

Although there was a background of broad spectral width, the polarization curves were fitted with the least squares method.

At $\theta = 78^{\circ}$, SH radiation was detected from solid Hg surfaces (at all solid Hg temperatures). No radiation was detected when the peak transmission wavelength of the Monopass narrow bandpass filter used was away from the second harmonic wavelength. The results obtained at the solid Hg temperature of -69 C $\pm$ 7 C are shown in FIGS. 4.16 (a), 4.16 (b)

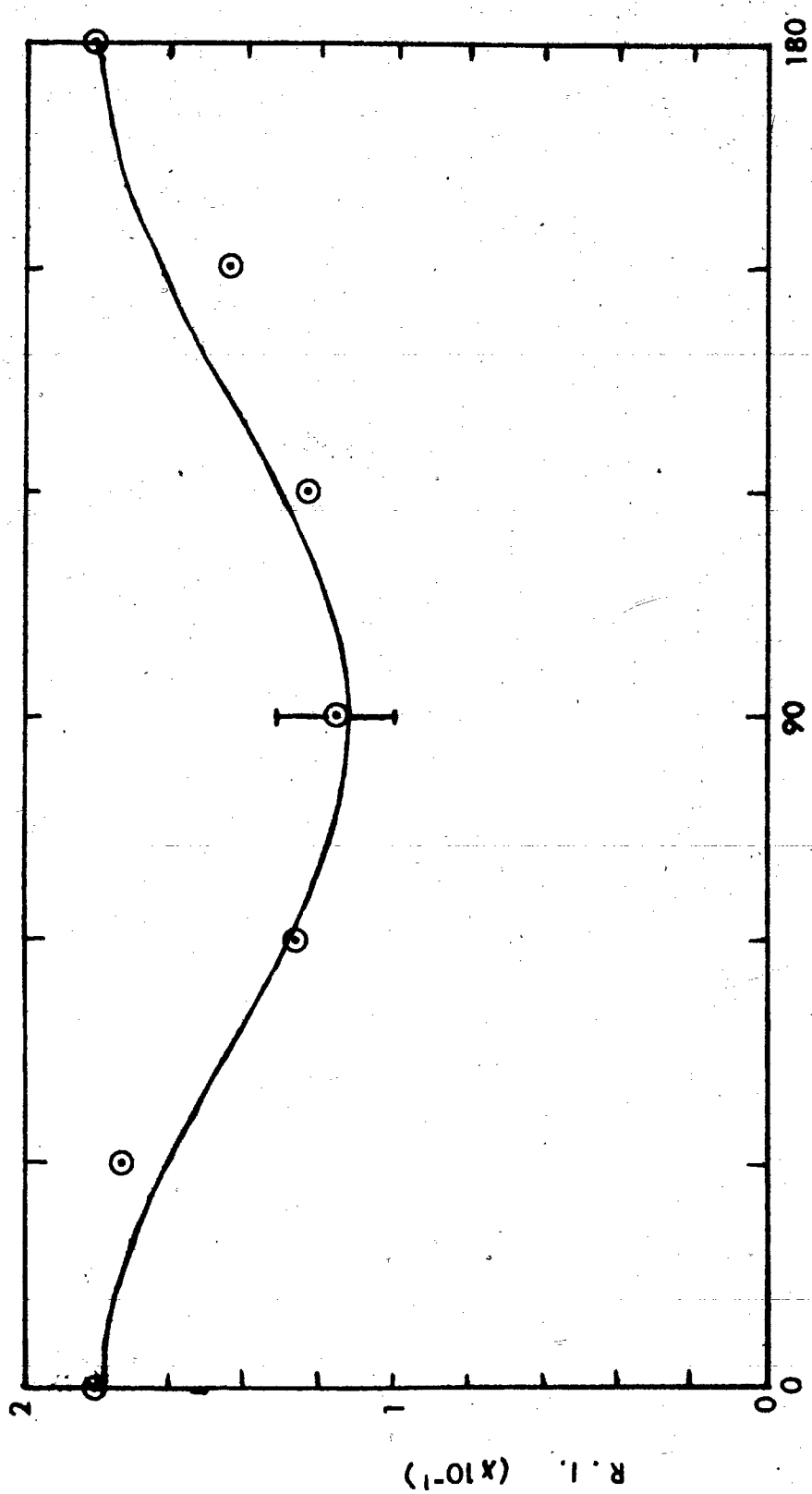

FIG. 4.15 (a) Polarization dependence of the light reflected from solid Hg. The relative intensity is plotted against the analyzer angle.
$\theta = 76^{o} \pm 1^{o}$; temperature= $-79^{o}C + 190^{o}C$; $\phi = 0^{o}$.
$I_p = 1.78 \times 10^{-1}$; $I_s = 1.12 \times 10^{-1}$; $\theta_o = +8^{o}$.

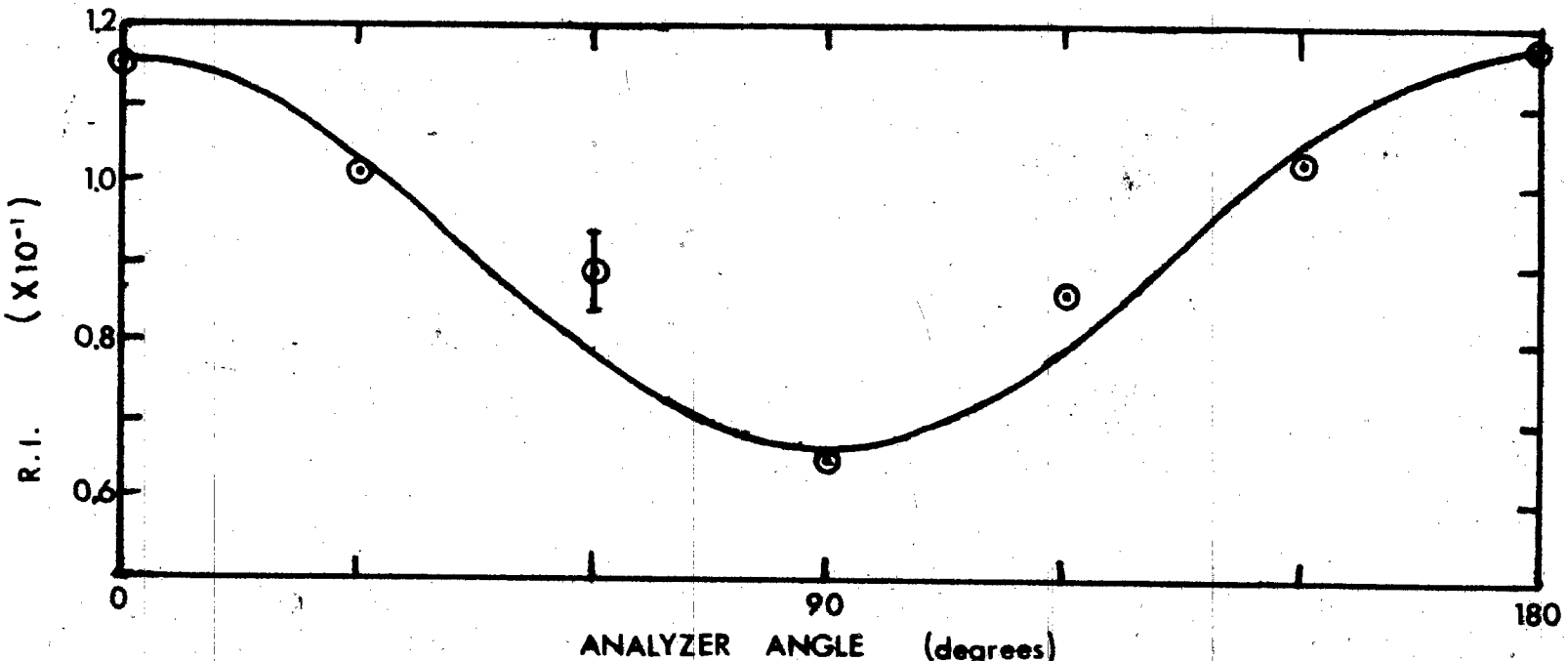

FIG. 4.15 (b) Polarization dependence of the light reflected from solid Hg. The relative intensity is plotted against the analyzer angle.

$\theta = 76^{\circ} \pm 1^{\circ}$; temperature $= -79^{\circ}C \pm 10^{\circ}C$; $\phi = 45^{\circ}$.

$I_p = 1.17 \times 10^{-1}$; $I_s = 6.65 \times 10^{-2}$; $\theta_o = +0.5^{\circ}$.

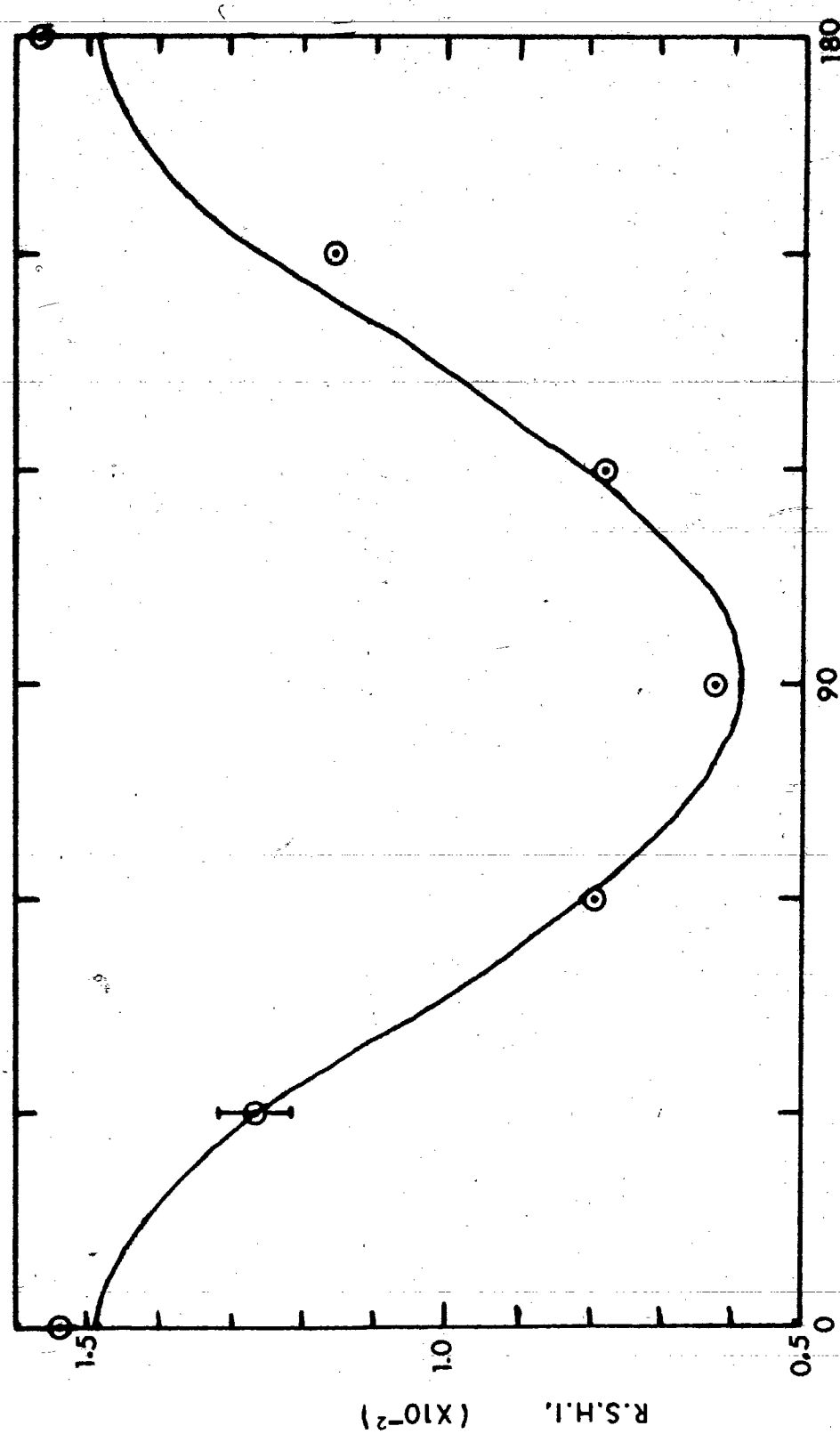

FIG. 4.16 (a) Polarization dependence of SH radiation from solid Hg.
$\theta = 78^{\circ} \pm 1^{\circ}$; temperature= $-69^{\circ}C \pm 7^{\circ}C$; $\phi = 0^{\circ}$.
$I_p = 1.48 \times 10^{-2}$; $I_s = 5.80 \times 10^{-3}$; $\theta_o = +2^{\circ}$.

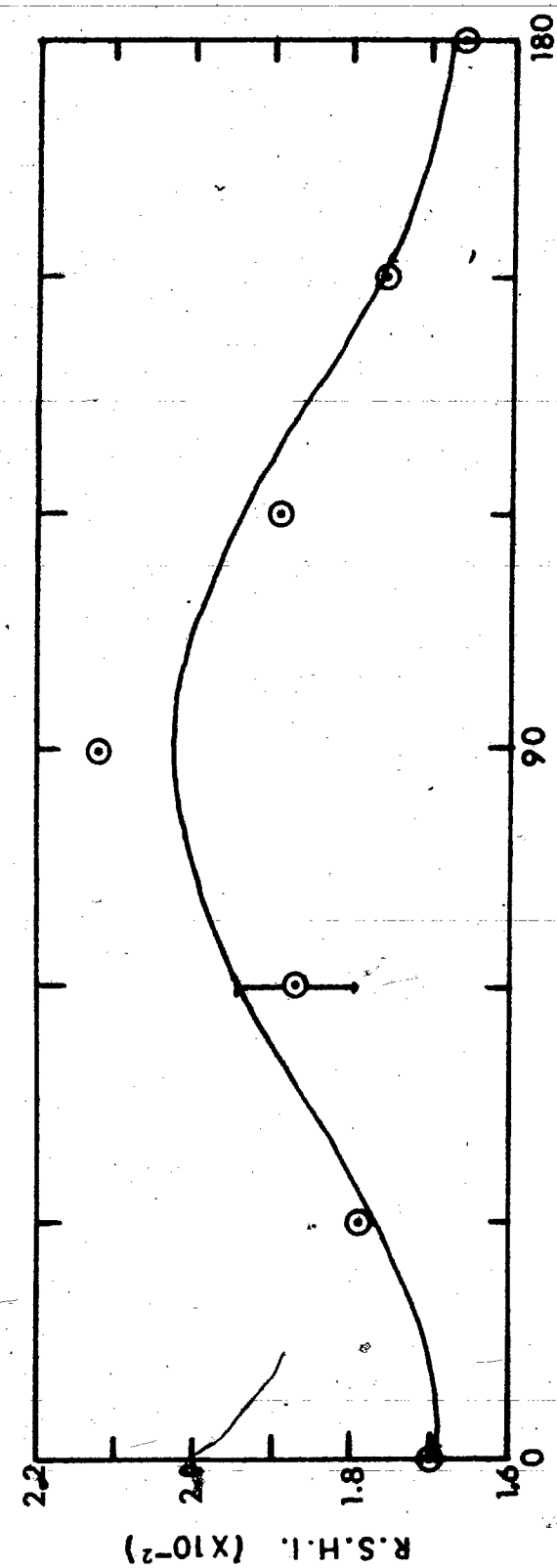

FIG. 4.16 (b) Polarization dependence of SH radiation from solid Hg. The relative second harmonic intensity is plotted against the analyzer angle. $\theta = 78^{\circ} \pm 1^{\circ}$; temperature= $-69^{\circ}C \pm 7^{\circ}C$; $\phi = 45^{\circ}$; $I_p = 1.68 \times 10^{-2}$; $I_s = 2.02 \times 10^{-2}$; $\theta_o = -0.5^{\circ}$.

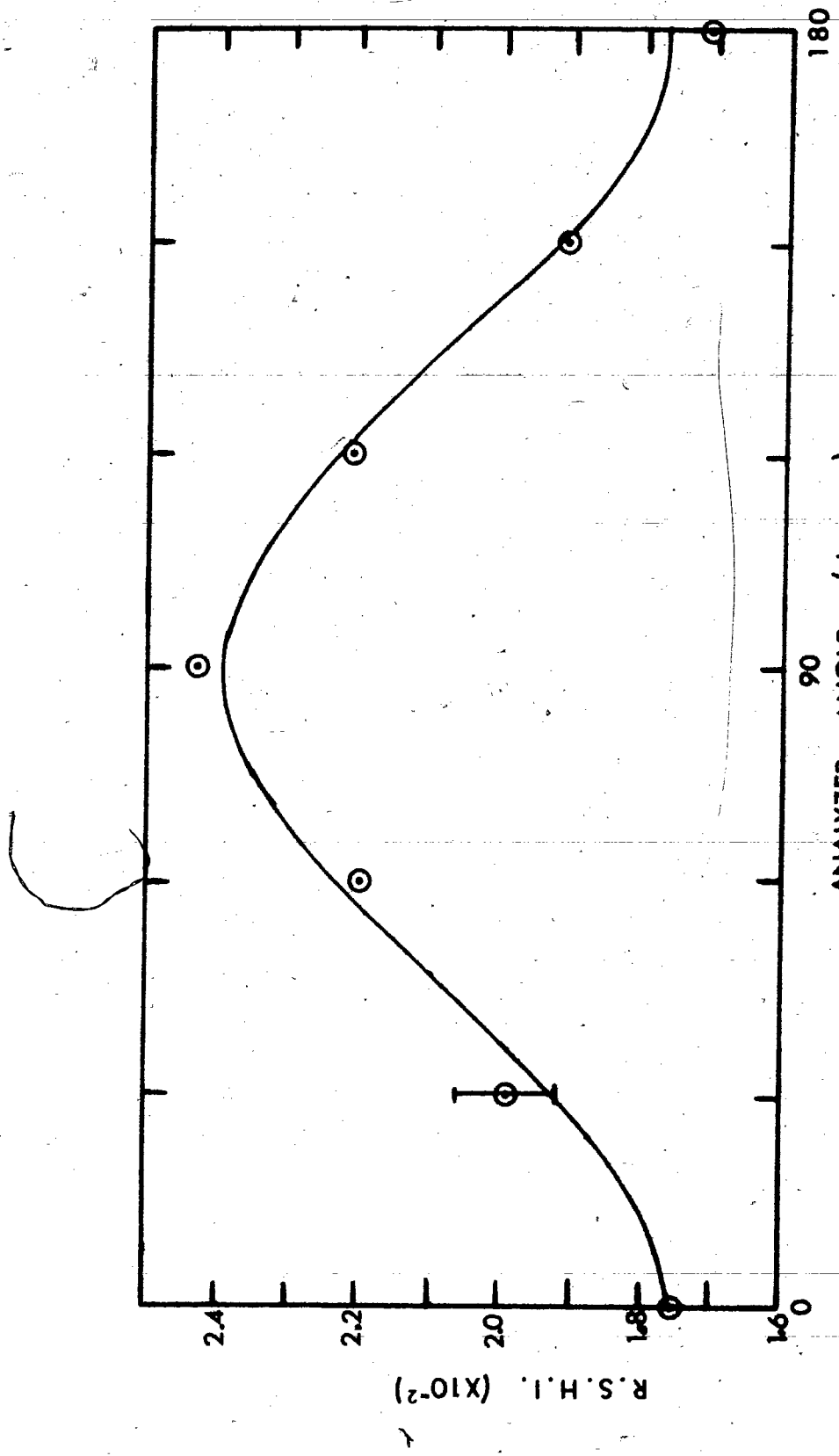

FIG. 4.16 (c) Polarization dependence of SH radiation from solid Hg. The relative SH intensity is plotted against the analyzer angle. $\theta = 78^{\circ} \pm 1^{\circ}$; temperature $= -69^{\circ}C \pm 7^{\circ}C$; $\phi = 90^{\circ}$; $I_p = 1.77 \times 10^{-2}$; $I_s = 2.39 \times 10^{-2}$; $\theta_o = -6^{\circ}$.

and 4.16 (c). The results obtained were similar to those for SHG from Ag surfaces. When a p polarized beam was incident on the solid Hg surface, I_p was greater than I_s in accordance with SHG theory. However when the incident radiation contained a component perpendicular to the plane of incidence ($\phi = 45^\circ$ and 90°), I_s was greater than I_p, contrary to SHG theory.

After distillation of a fresh Hg surface, the glass vacuum housing was found to be covered with Hg. Measurements were taken after the Hg had been evaporated off the glass housing, by heating the glass with a heat gun. The polarization curve for $\theta = 78^\circ$ and $\phi = 90^\circ$ with the $\lambda/2$ plate in the optical train is shown in FIG. 4.17 (a). FIG. 4.17 (b) shows the polarization dependence of the light detected from solid Hg under the same experimental conditions as in FIG. 4.17 (a) except for the exclusion of the $\lambda/2$ plate. Since the polarizer was set to transmit s polarized light ($\phi = 90^\circ$), FIGS. 4.17 (a) and 4.17 (b) should show the same behaviour. A separate test with a fundamental wavelength (1060 nm.) pyroelectric detector also confirmed that the $\lambda/2$ plate was indeed a $\lambda/2$ plate.

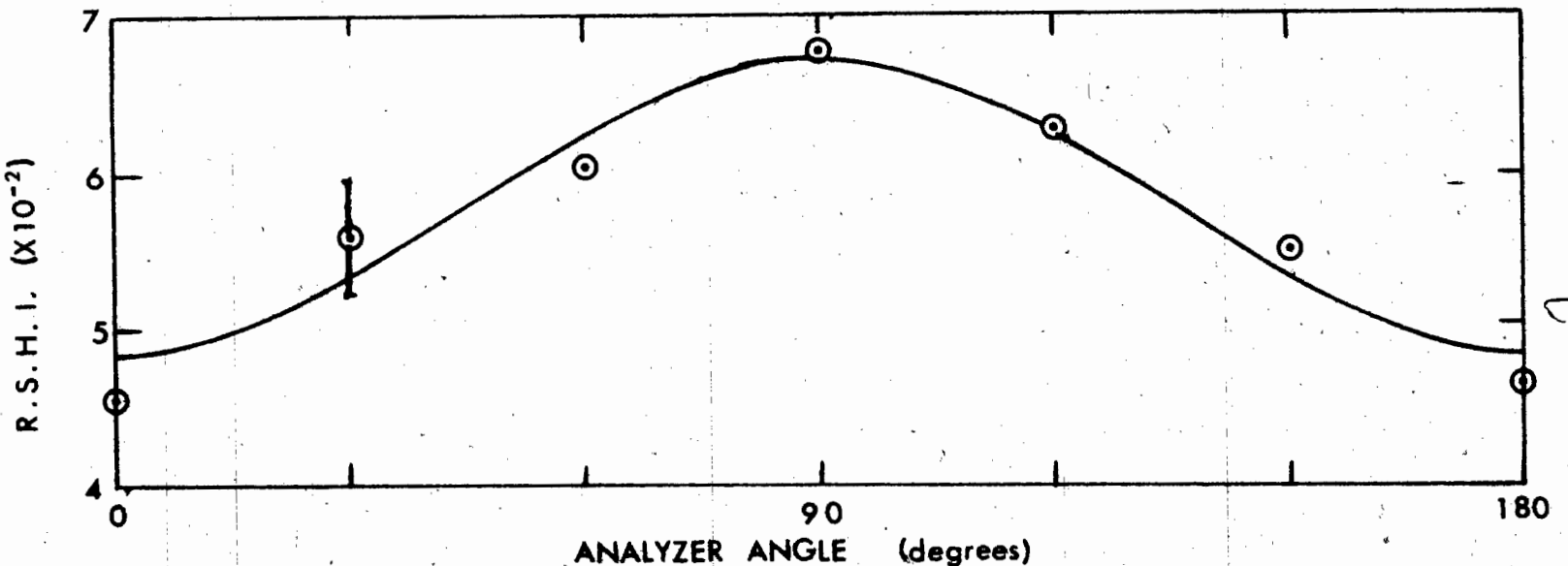

FIG. 4.17 (a) Polarization dependence of SH radiation from solid Hg after the glass housing was found to be covered with Hg. $\theta = 78^{\circ} \pm 1^{\circ}$; $\phi = 90^{\circ}$ with $\lambda/2$ plate; $I_p = 4.86 \times 10^{-2}$; $I_s = 6.74 \times 10^{-2}$; $\theta_o = +1^{\circ}$; temperature $= -69^{\circ}C \pm 10^{\circ}C$.

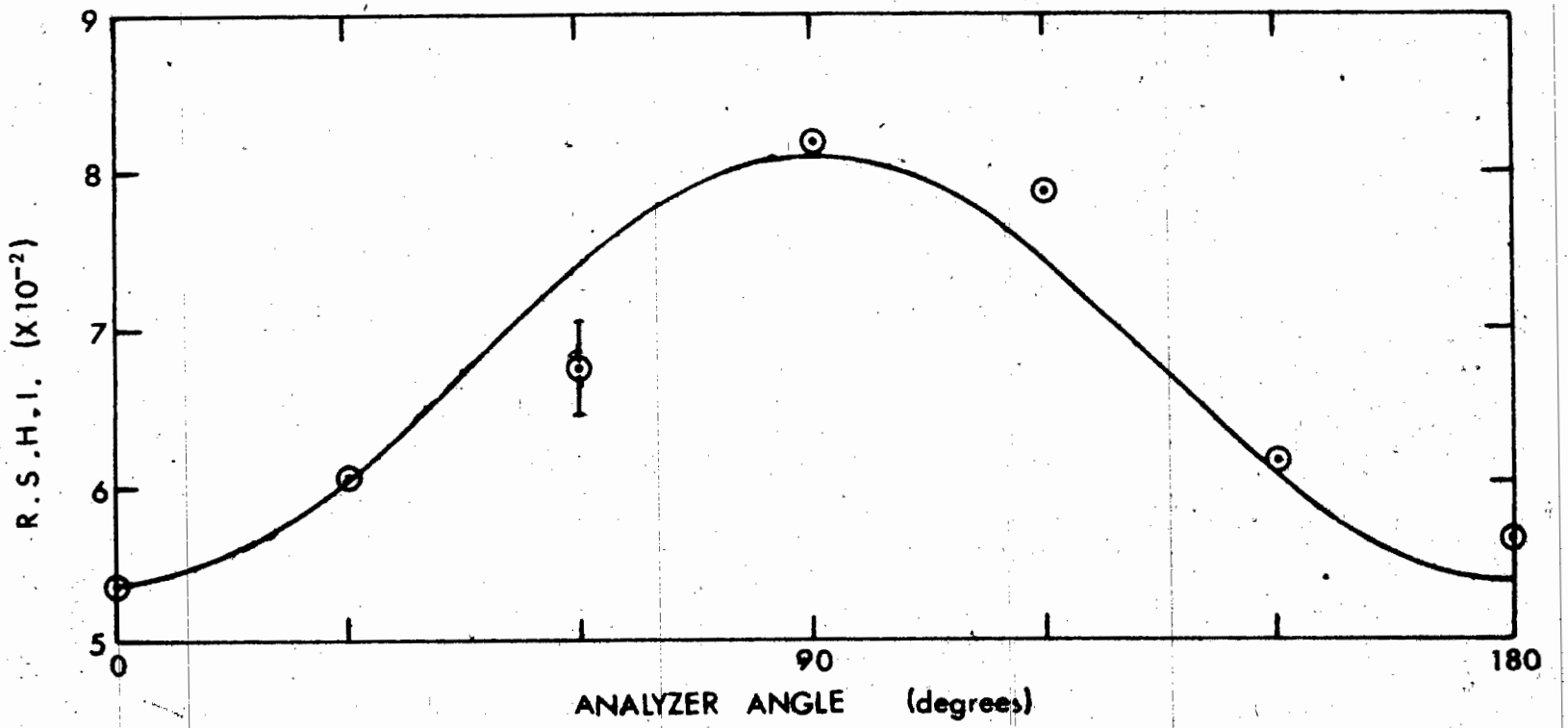

FIG. 4.17 (b) Polarization dependence of SH radiation from solid Hg without $\lambda/2$ plate in the optical train.
$\theta = 78^{\circ} \pm 1^{\circ}$; $\phi = 90^{\circ}$; temperature $= -69^{\circ}C \pm 10^{\circ}C$;
$I_p = 5.37 \times 10^{-2}$; $I_s = 8.11 \times 10^{-2}$; $\theta_o = +7^{\circ}$.

Having obtained the experimental conditions under which SH radiation was detected, the angle of incidence was changed to $\theta = 71^{\circ}$. Assuming a simple relationship

$$E_{71} A_{71} = E_{78} A_{78}$$

where E is the energy density and A the area of the incident beam projected onto the Hg surface, it was determined that the incident beam intensity at $\theta = 71^{\circ}$ should be attenuated to ~ 0.5 of the intensity at $\theta = 78^{\circ}$. A neutral density filter of optical density 0.3 or an attenuation factor of 0.5 was inserted between the ultrafast photodiode and the KDP powder in the optical train. No radiation was detected at all temperatures with Monopass narrow bandpass and Corning CS-494 filters in front of the sample photomultiplier.

The neutral density filter was removed and measurements were taken. No radiation was detected with Monopass and Corning CS-494 filters in front of the sample photomultiplier.

The radiation detected from solid Hg in absence of Monopass filters in the optical train, was found to be unpolarized. The results are shown in FIG. 4.18 for p and s polarized incident radiation. If SH radiation was generated at $\theta = 71^{\circ}$, it was of

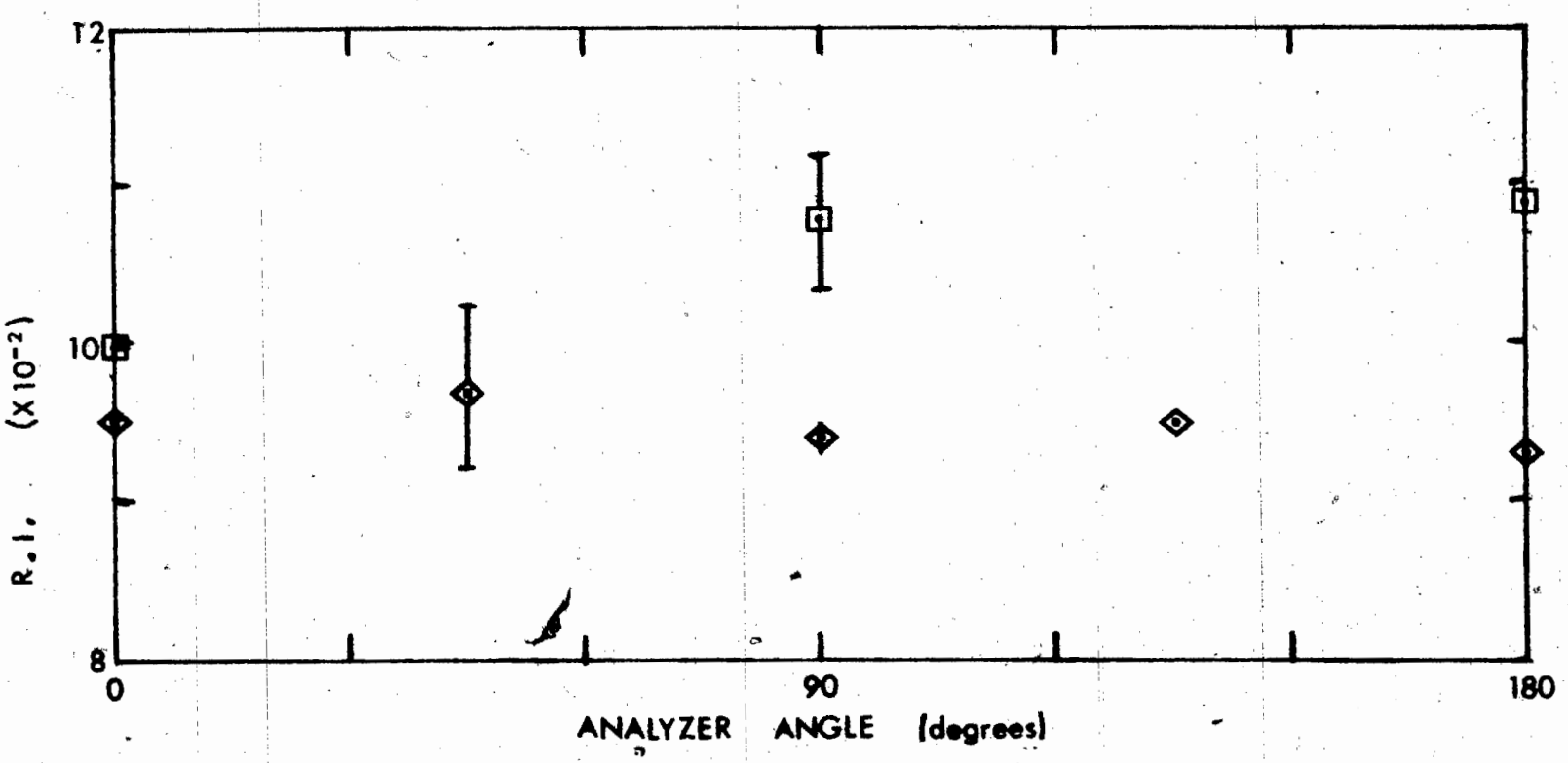

FIG. 4.18 Polarization dependence of light reflected from solid Hg. $\theta = 71^{\circ} \pm 1^{\circ}$; temperature= $-52^{\circ}C \pm 4^{\circ}C$; ⊡ $\phi = 0^{\circ}$; ◈ $\phi = 90^{\circ}$.

insufficient intensity to be distinguished from the broad background radiation.

CHAPTER 5

INTERPRETATION OF RESULTS

5-1 SUMMARY OF RESULTS

In the preceding chapters, the results of SHG (second harmonic generation) by reflection from Ag and Hg surfaces have been presented.

The interpretation of the results for Ag are presented in the following section. Second harmonic radiation was detected from Ag at both angles of incidence, $\theta = 70^{\circ}$ and 60°, investigated. For incident radiation polarized in the plane of incidence ($\phi = 0^{\circ}$), I_p, the p component of the SH radiation detected was found to be greater than I_s, the s component. However, when the incident beam contained an s component ($\phi = 45^{\circ}$ and 90°), I_p was less than I_s.

The system of main interest, Hg, was investigated in liquid and solid phases at temperatures between $26^{\circ}C$ and $-131^{\circ}C$.

The radiation detected from liquid Hg surfaces at angles of incidence $60^{\circ} \leq \theta \leq 74^{\circ}$, was found to be dominated by background radiation of broad spectral width. No radiation was detected at $\theta = 76^{\circ}$ and 78°, when Monopass narrow bandpass and Corning CS-494

SH pass filters were inserted in front of the sample photomultiplier. Liquid Hg results are discussed in section 5-3.

At angles of incidence $\theta = 60^{\circ}$ and 74°, tests for second harmonic radiation revealed the radiation generated at solid Hg surfaces to be dominated by background radiation as at liquid Hg surfaces. The tests for SH radiation from solid Hg surfaces at $\theta = 76^{\circ}$ revealed a peak in the relative intensity near 531 nm., the second harmonic wavelength. The relative intensities at $\lambda_p = 438$ nm. and 591 nm. were non-zero, indicating that background radiation as well as SH radiation was being generated. The broad band radiation detected in the absence of a Monopass narrow bandpass filter with λ_p near 531 nm. in the optical train, was found to be polarization dependent.

No background radiation was detected from solid Hg at $\theta = 78^{\circ}$. The SH radiation detected followed the pattern of behaviour exhibited by the SH radiation detected from Ag surfaces. For a p polarized incident beam, I_p was greater than I_s, whereas for incident radiation with polarization angles $\phi = 45^{\circ}$ and 90°, I_p was less than I_s.

In order to check experimental procedure, the

angle of incidence was altered to $\theta = 71^{\circ}$ and the incident beam power density adjusted to be the same as at $\theta = 78^{\circ}$. The radiation detected from solid Hg surfaces at $\theta = 71^{\circ}$ was broad in spectral width and showed no polarization dependence.

The results for solid Hg are discussed in section 5-4.

Suggestions for further experiments are discussed in section 5-5.

5-2 DISCUSSION OF Ag RESULTS

Second harmonic radiation was detected from Ag surfaces at $\theta = 70^{\circ}$ and 60°. The Ag surface was prepared by evaporating Ag onto a glass plate which was transferred to a high vacuum chamber. The vacuum chamber was pumped down to a pressure of 2×10^{-7} torr. During the transfer procedure from the evaporator to the vacuum chamber, the Ag surface was exposed to the atmosphere.

The s component of the second harmonic radiation was found to be non-zero for both p ($\phi = 0^{\circ}$) and s ($\phi = 90^{\circ}$) polarized incident beams contrary to SHG theory. In a study of SHG from Ag surfaces, McCardell[11] also observed non-zero I_s for p polarized incident radiation, but did not report data for incident beams with ϕ other than 0°. In the experi-

ments of McCardell, depositions of Ag were made directly in the chamber in which measurements were taken. According to McCardell, the non-zero values of I_s for p polarized incident radiation were due to a weak non-thermally produced background radiation which was quite broad in its spectrum and unpolarized.

The background radiation was taken by McCardell to be the difference between the reading when the peak transmission wavelength of a $NiSO_4$ SH pass filter was at 546 nm., and when it was rotated so that the peak in the transmission was at 530 nm. In the present study, the peak transmission wavelengths of the Monopass narrow bandpass filters used were 438 nm., 522 nm., and 591 nm. Signals were detected with the 522 nm. peak transmitting filter (FWHM=15 nm.) only. Since readings at $\lambda_p \sim 546$ nm. were not taken, it was possible that similar background radiation existed. On the other hand, if it is assumed that the radiation detected in the present study was SH radiation only, the observation that the radiation detected never reached zero for any analyzer setting indicates that the SH radiation generated by p and s polarized incident beams was elliptically polarized. In this case, the equations of Rudnick and Stern are inappropriate because they predict the SH radiation

to be linearly polarized for p and s polarized incident radiation. (See section 2-3)
The equations of Rudnick and Stern also predict that for incident radiation with $\phi = 0^{o}$ or 90^{o}, I_s is zero, in disagreement with the results of this thesis.

In the present study, for incident beams with $\phi = 45^{o}$ and 90^{o}, I_s was found to be greater than I_p. Indeed, the ratio I_s/I_p was several orders of magnitude greater than the theoretically predicted value. A comparison of the experimental results with theory, of the ratio I_s/I_p is given in table II. The equations of Rudnick and Stern were used to calculate the theoretical values. ε_1 and ε_2 of the dielectric constant for Ag, $\varepsilon = \varepsilon_1 + i\varepsilon_2$, used were $\varepsilon_1(\omega) = -46.6$, $\varepsilon_2(\omega) = -17.6$, $\varepsilon_1(2\omega) = -11.0$, and $\varepsilon_2(2\omega) = -3.65$.[26] Theoretically, I_s and hence the ratio I_s/I_p is equal to zero for p and s polarized incident beams. I_s/I_p was enhanced when the incident radiation contained an s component as evidenced by the results of table II.

The experimental ratio $I_{\pi/2}/I_o$ which provides a comparison of the bulk contributions relative to that of the surface contributions, to the SH

$\theta = 70^\circ$	ϕ	$[I_s/I_p]$ expt.	$[I_s/I_p]$ theory
	0°	0.524 ± 0.037	0
	45°	1.42 ± 0.10	5.68×10^{-3}
	90°	1.98 ± 0.14	0
$\theta = 60^\circ$	0°	0.929 ± 0.066	0
	45°	1.02 ± 0.07	2.00×10^{-2}
	90°	1.08 ± 0.76	0

Table II Comparison of experiment with theory of the ratio I_s/I_p, for Ag.

radiation, was found to be two orders of magnitude greater than the theoretical ratio. A comparison of the data is given in table III. $I_{\pi/2}$ is the p component of the SH radiation generated when incident radiation is polarized perpendicular to the plane of incidence. According to RS, when an incident beam is s polarized, the SH radiation generated is due entirely to bulk currents. I_o is the intensity of the p component of the SH radiation generated by an incident beam polarized in the plane of incidence. When the incident radiation is polarized in the plane of incidence, the SH radiation generated receives contributions from $E_{||p}$, $E_{\perp p}$, and E_{Bp}. Therefore, the ratio $I_{\pi/2}/I_o$ is useful for comparing the relative contributions of the bulk currents and the surface currents to the SH intensity.

Since theory predicts I_s to be equal to zero for p polarized incident beams, I_s for a p polarized incident beam was taken as the background in table III. The corrected ratios of $I_{\pi/2}/I_o$ are negative since at both angles of incidence, I_s for $\phi = 0^o$ is greater than I_p for $\phi = 90^o$. The background subtraction procedure is therefore inappropriate, in that the s component of the SH radiation generated by a p polarized incident beam cannot be interpreted

$\theta = 70^{\circ}$	$I_{\pi/2}/I_o$	pressure
theory	0.00122	
present expt.	0.373 ± 0.026	2×10^{-7} torr.
minus background	-0.293 ± 0.020	
$\theta = 60^{\circ}$		
theory	0.00534	
present expt.	0.787 ± 0.056	2×10^{-7} torr.
minus background	-2.00 ± 0.14	
McCardell	0.043 ± 0.003	at 10^{-10} torr.
Brown $\theta = 54^{\circ}$	0.046 ± 0.010	2×10^{-7} torr.

Table III A comparison of experiment with theory of the ratio $I_{\pi/2}/I_o$. The background was taken to be the s component of the SH radiation for an incident beam with $\phi = 0^{\circ}$.

as background radiation.

$I_{\pi/2}/I_o$ for the present experiment is ∿ one order of magnitude greater than the values obtained by other experimentalists. The measurements of McCardell[11] and Brown[10] were made for Ag surfaces that were subject to less contamination than the Ag surfaces used in the present experiment. Therefore, the increase in $I_{\pi/2}/I_o$ may be due to adsorbed gases.

As explained earlier, the s component of the SH radiation generated by p polarized incident radiation cannot be interpreted as background radiation. Hence the equations of Rudnick and Stern are not appropriate for the present experiment. To illustrate this point further, I_p and $I_p \cos^4\phi$ are listed in table IV. The I_p's have been normalized with respect to I_p at $\phi = 0^o$. The experimental values do not agree with the theoretical values.

5-3 DISCUSSION OF LIQUID Hg RESULTS

SHG from liquid Hg surfaces was investigated at four angles of incidence, 60^o, 74^o, 76^o, and 78^o. At $\theta = 60^o$ and 74^o, the radiation detected from liquid Hg surfaces was found to be dominated by broad band background radiation. No radiation was detected when Monopass narrow bandpass and Corning CS-494 SH pass filters were inserted in front of the sample

$\theta = 70^\circ$

ϕ	I_p	$I_p \cos^4\phi$
0°	1.00 ± 0.07	1.00 ± 0.07
45°	0.429 ± 0.030	0.250 ± 0.008
90°	0.373 ± 0.026	0.000

$\theta = 60^\circ$

ϕ	I_p	$I_p \cos^4\phi$
0°	1.00 ± 0.07	1.00 ± 0.07
45°	0.947 ± 0.067	0.250 ± 0.017
90°	0.787 ± 0.056	0.000

Table IV Examination of the $\cos^4\phi$ dependence of the radiation detected from Ag.

photomultiplier.

The background radiation was found to be essentially independent of the angle of incidence for $\theta = 60^{\circ}$ and 74°. A comparison of the R.I. at the angles of incidence is shown in table V. The R.I. for p polarized incident beams and an analyzer setting of 0° are listed in column 3. Since $I(2\omega) \propto I^2(\omega)$ or $I(2\omega) \propto (\text{beam size})^{-2}$ for an assumed constant input energy, the product of the R.I. and the square of the beam size was listed in column 5.

At $\theta = 60^{\circ}$ and a temperature of $26^{\circ}C$, the R.I. decreased as the incident beam size was increased. However, the product P of the R.I. and the square of the incident beam size increased as the incident power density was decreased. If the radiation detected was SH radiation only, P should have remained constant. Hence, the results of table V confirm that the radiation generated at the sample surface at $\theta = 60^{\circ}$ was dominated by background radiation.

P also increased as the temperature of the Hg was lowered. Since the tests for SH radiation revealed the radiation detected to be dominated by background radiation, it must be concluded that for $\theta = 60^{\circ}$ and 74°, the generation of background radiation

θ	temperature	R.I.	beam size ($cm.^2$)	P=R.I. X (beam size)^2
60°	26°C ± 1°C	0.0134 ± 0.0005	0.3 ± 0.05	0.00121 ± 0.00390
		0.0113 ± 0.0006	0.8 ± 0.1	0.00723 ± 0.00185
		0.0107 ± 0.0005	0.9 ± 0.1	0.00867 ± 0.00197
	11°C ± 1°C	0.0310 ± 0.0016	0.3 ± 0.05	0.00279 ± 0.00094
	-40°C ± 10°C	0.0300 ± 0.0015	0.9 ± 0.1	0.0243 ± 0.0055
	-131°C ± 1°C	0.0771 ± 0.0019	0.9 ± 0.1	0.0625 ± 0.0139
74°	20°C ± 1°C	0.00145±0.00005	2.2 ± 0.2	0.00702 ± 0.00130
	-24°C ± 1°C	0.0248 ± 0.0008	0.8 ± 0.1	0.0159 ± 0.0040
	-53°C ± 12°C	0.0136 ± 0.0009	2.2 ± 0.2	0.0658 ± 0.0127
	-91°C ± 16°C	0.0142 ± 0.0010	2.2 ± 0.2	0.0687 ± 0.0134
76°	-79°C ± 10°C	0.0125 ± 0.0013	1.4 ± 0.1	0.0245 ± 0.0043

Table V R.I. as a function of beam size and angle of incidence. The R.I. listed are the readings at λ_p=522 nm., ϕ= 0°, and analyzer angle= 0°.

increased as the temperature of the Hg was lowered. The same claim cannot be made for $\theta = 76^{\circ}$, at which signals were detected from solid Hg and not from liquid Hg.

On the basis of the experimental evidence, no definitive statement concerning the mechanism by which the background radiation is generated, can be made.

5-4 DISCUSSION OF SOLID Hg RESULTS

Solid Hg was investigated at five angles of incidence, 60°, 74°, 76°, 78°, and 71°. The results for solid Hg at $\theta = 60^{\circ}$ and 74° were similar to those for liquid Hg at the same angles of incidence in that the radiation detected was found to be dominated by background radiation. SH radiation was detected from solid Hg surfaces at $\theta = 76^{\circ}$ and 78°. When the incident power density at $\theta = 71^{\circ}$ was adjusted to be the same as the power density at $\theta = 78^{\circ}$ in order to check experimental procedure, the radiation detected was found to be broad in spectral width and unpolarized.

At $\theta = 76^{\circ}$, the tests for SH radiation revealed a peak in the R.I. at $\lambda_p = 522$ nm. for incident beams with $\phi = 0^{\circ}$ and 45°. No signal was detected for an s polarized incident beam. This is consistent with

the theory of Rudnick and Stern since they predict the generation efficiency of an s polarized beam at $\theta = 76^\circ$ to be ~ 4 orders of magnitude less than the generation efficiency of a p polarized incident beam.

A comparison of the experimental data with the $\cos^4\phi$ dependence of the SH intensity predicted by SHG theory is given in table VI. Normalized I_p's are listed. The background radiation was assigned the value of I_s at $\phi = 45^\circ$ for the following reasons. For pure SH signals, RS predict I_s to be zero for incident radiation with $\phi = 0^\circ$. However, I_s for a p polarized incident beam was found to be $\sim I_p$ for an incident beam polarized 45° with respect to the plane of incidence. The background was calculated from the following relationship for the data at $\phi = 45^\circ$.

$$\frac{I_s(\text{expt.}) - \text{background}}{I_p(\text{expt.}) - \text{background}} = \frac{I_s(\text{theory})}{I_p(\text{theory})}$$

The background was calculated to be the same as the experimental I_s at $\phi = 45^\circ$. The fit of the experimental data for solid Hg at $\theta = 76^\circ$ although poor, was comparable to that for the SH radiation detected from Ag at $\theta = 70^\circ$ and 60°. Therefore it is reasonable to conclude that SH radiation dominated the radiation

$\theta = 76^\circ$	ϕ	I_p(raw data)	I_p(minus background)	$\cos^4\phi$
	0°	1.00 ± 0.13	1.00 ± 0.21	1.00
	45°	0.646 ± 0.384	0.443 ± 0.130	0.25
	90°	0.00	0.00	0.00

Table VI A comparison of experiment with theory of Rudnick and Stern for the SH radiation detected from solid Hg. Normalized I_p's are listed. The background was taken to be I_s at $\phi = 45^\circ$, for reasons given in the text. The background was not subtracted from I_p for $\phi = 0^\circ$.

reflected from solid Hg at $\theta = 76^{\circ}$.

Unlike the data for Ag and for Hg at $\theta = 78^{\circ}$, I_s was found to be less than I_p for the radiation detected from solid Hg at $\theta = 76^{\circ}$ for incident radiation polarized at 45° with respect to the plane of incidence. A comparison of the experimental data with theory of the ratio I_s/I_p for the radiation detected from solid Hg is given in table VII. The theoretical ratios were calculated by inserting the dielectric constants for single crystal solid Hg obtained by Choyke, Vosko, and O'Keefe[17] into the equations of Rudnick and Stern. Experiment does not agree with theory.

From solid Hg surfaces at $\theta = 78^{\circ}$, signals were detected at $\lambda_p = 522$ nm., whereas no signals were detected at $\lambda_p = 438$ nm. and 591 nm. Unlike data at other angles of incidence, I_p increased as ϕ was changed from 0° to 45° to 90°. A comparison of experimental data with theory of the $\cos^4\phi$ dependence of the intensity of the SH radiation is given in table VIII. As in previous cases, the I_p's have been normalized with respect to I_p for $\phi = 0^{\circ}$. The background radiation was assigned the value of I_s at $\phi = 0^{\circ}$, since according to theory I_s

$\theta = 76^\circ$	ϕ	$[I_s/I_p]$expt.	$(I_s-BG)/(I_p-BG)$	$[I_s/I_p]$theory
	0°	0.663 ± 0.084	0.469 ± 0.127	0
	45°	0.565 ± 0.072	0.000	0.00155

Table VII A comparison of experiment with theory of the ratio I_s/I_p for the radiation detected from solid Hg. The dielectric constants for single crystal solid Hg obtained by Choyke, Vosko, and O'Keefe[17] from normal incidence reflectivity measurements were substituted into the equations of Rudnick and Stern in order to calculate the theoretical ratios.

$\theta = 78^\circ$	ϕ	I_p	I_p - BG	$\cos^4\phi$
	0°	1.00 ± 0.07	1.00 ± 0.13	1.00
	45°	1.14 ± 0.07	1.22 ± 0.14	0.25
	90°	1.20 ± 0.07	1.32 ± 0.15	0.00

Table VIII A comparison of the experimental data with theory, of the $\cos^4\phi$ dependence predicted for the SH intensity. The background was assigned the value I_s for p polarized incident beams. Normalized I_p's are listed. Temperature of Hg= $-69^\circ C \pm 7^\circ C$.

is zero. As for the SH data from Ag surfaces, it is apparent that theory does not apply to SHG from solid Hg surfaces.

The polarization dependence of the SH radiation from solid Hg at $\theta = 78^{\circ}$ was similar to that of the SH radiation from Ag. For p polarized incident radiation, I_s was non-zero and smaller than I_p. For incident beams with polarization angle $\phi = 45^{\circ}$ and 90°, I_s was greater than I_p contrary to theory.

The experimental ratio I_s/I_p is compared with theory in table IX for the SH radiation detected at $\theta = 78^{\circ}$. The theoretical ratios were calculated by inserting the dielectric constants for single crystal solid Hg obtained from normal incidence reflectivity measurements into the equations of Rudnick and Stern. The results are comparable to that of Ag in that I_s/I_p increased as ϕ was changed from 0° to 45° to 90°.

In the equations of Rudnick and Stern, it is assumed that for p and s polarized incident radiation, I_s is zero. Experimentally I_s was non-zero for p and s polarized radiation incident on Ag and Hg surfaces. There is no satisfactory method by which the non-zero I_s may be subtracted which yields consistent results. Problems with negative I_p's

$\theta = 78^\circ$	ϕ	$[I_s/I_p]$(raw data)	$(I_s - BG)/(I_p - BG)$	$[I_s/I_p]$theory
	0°	0.392 ± 0.026	0.00	0.00
	45°	1.20 ± 0.076	1.31 ± 0.12	0.00105
	90°	1.35 ± 0.076	1.52 ± 0.13	0.00

Table IX A comparison of the experimental data with theory of the ratio I_s/I_p. The equations of Rudnick and Stern were used to calculate the theoretical ratios. BG was assigned the value of I_s at $\phi = 0^\circ$.

arise if the s components of the SH radiation generated by p and s polarized radiation are designated as background radiation. Therefore the experimental ratios do not agree with the theoretical ratios.

The contribution of the bulk currents relative to that of the surface currents, to the SH intensity was $I_{\pi/2}/I_o = 1.20 \pm 0.07$ as compared with the theoretical value of 1.22×10^{-4}. $I_{\pi/2}$ is the p component of the SH radiation generated by s polarized incident radiation. I_o is the p component of the SH radiation generated by p polarized incident radiation. The comments made in the previous section with regard to the non-zero I_s and I_s being greater than I_p for incident radiation polarized 45° and 90° with respect to the plane of incidence, also apply here.

The relative magnitudes of I_p for Ag and Hg are compared with theory in table X. The ratio $I_p(Ag)/I_p(Hg)$ is compared with theoretical ratios calculated from the equations of Rudnick and Stern. The dielectric constants used were expressed as $\varepsilon(\omega) = \varepsilon_1(\omega) + i\varepsilon_2(\omega)$ and $\varepsilon(2\omega) = \varepsilon_1(2\omega) + i\varepsilon_2(2\omega)$. The values of ε_1 and ε_2 for Ag reported earlier in

$\theta(Ag) = 70^\circ$ $\quad \theta(Hg) = 78^\circ$			
ϕ	$[I_p(Ag)/I_p(Hg)]_{expt.}$	$[I_p(Ag)/I_p(Hg)]_{theory}$	$I_p(Hg)$
0°	4.95 ± 0.35	0.325	0.0148 ± 0.0007
45°	1.97 ± 0.13	0.342	0.0168 ± 0.0008
90°	0.648 ± 0.46	3.24	0.0177 ± 0.0009
$\theta(Ag) = 60^\circ$ $\quad \theta(Hg) = 78^\circ$			
0°	19.1 ± 1.35	0.173	0.0148 ± 0.0007
45°	15.9 ± 1.12	0.197	0.0168 ± 0.0008
90°	12.5 ± 1.06	7.65	0.0177 ± 0.0009

Table X A comparison of the SHG efficiencies from Ag and Hg surfaces.

section 5-2 were used. For Hg, $\varepsilon_1(\omega)= -41.0$, $\varepsilon_2(\omega)= -17.0$, $\varepsilon_1(2\omega)= -17.0$, and $\varepsilon_2(2\omega)= -14.0$. The experimental ratios decreased as ϕ was changed from 0° to 45° to 90° in opposite behaviour to the theoretical ratios. This was due to the increase in I_p(Hg) as ϕ was changed from 0° to 45° to 90°.

The project described in this thesis was undertaken in an effort to resolve the difference in the dielectric constants of liquid Hg obtained by ellipsometry and reflectivity measurements, and also in order to investigate the nature of the proposed transition layer. However, the radiation detected from liquid Hg surfaces was found to be dominated by unpolarized background radiation. Therefore no comments can be made regarding the different dielectric constants obtained in the linear optical experiments.

Evidence of SH generation as well as background generation was seen at $\theta= 76^\circ$ from solid Hg surfaces. The bulk contribution ($\phi= 90^\circ$) to the SH intensity was too weak to be detected. At $\theta= 78^\circ$, in contrast to SHG from alkali metals,[14] where the surface contribution to the SH intensity was one to two orders of magnitude greater than the bulk

contribution, the bulk contribution to the SH radiation generated at solid Hg surfaces was found to be the same order as the surface contribution.

At both angles of incidence $\theta = 76^{\circ}$ and 78°, the theory of Rudnick and Stern predicted values of I_s/I_p which were several orders of magnitude smaller than the experimental results. In addition, the p component of the SH radiation did not follow the $\cos^4\phi$ dependence predicted by SHG theory.

In the analysis of the SH data for solid Hg, a conductivity profile of the type introduced in chapter 1 was not used. It was shown in chapter 2 that the ratio $I_{\pi/2}/I_o$ is greater for the two layer model of Hg than for the model in which there is no surface transition layer. In view of the poor agreement between experiment and theory of the ratio $I_{\pi/2}/I_o$, the use of separate dielectric constants for the surface, ε_s, and for the bulk, ε_B, seemed warranted. However it can also be seen from FIGS. 2.2 and 2.3 that the ratio of the s component of the SH radiation to the p component, I_s/I_p decreases when a transition zone is introduced, worsening the agreement between experiment and theory.

In conclusion, the SHG theory of Rudnick and Stern was found to be inappropriate when applied to the experiment described in this thesis.

5-4 SUGGESTIONS FOR FURTHER EXPERIMENTS

The SHG investigation of Hg surfaces reported in this thesis should be regarded as a preliminary investigation. The results suggest that further measurements of SHG from Hg at and around $\theta = 78^{\circ}$ are in order.

Surface conditions were found to affect the SHG efficiency from Hg surfaces. For example, Crozier, Ninnis and Rieckhoff detected SH radiation from liquid and solid Hg surfaces maintained at 2×10^{-6} torr. at $\theta = 72^{\circ}$ and 74°. In the present experiment, SH radiation was distinguished from background radiation generated at solid Hg surfaces maintained at $\theta \cong 78^{\circ}$ only. It is conceivable that differences in the results of ellipsometry, reflectivity, and surface plasmon excitation measurements made at $\sim 10^{-6}$ torr. and $\sim 10^{-10}$ torr. may exist. These measurements should be repeated for clean Hg surfaces, namely for Hg maintained at ultrahigh vacuum pressures $\sim 10^{-10}$ torr.

APPENDIX 1

LEAST SQUARES FIT

The p and s components of the radiation detected were extracted by fitting the polarization data to a finite fourier series which has been shown by Buckingham[27] to be equivalent to a least squares technique.

An expression for the intensity of the light exiting from the polarizer/analyzer configuration

$$I(\alpha)= Re(E_pE_p^*\cos^2\alpha + E_sE_s^*\sin^2\alpha + E_pE_s^*\cos\alpha\sin\alpha + E_p^*E_s\cos\alpha\sin\alpha \quad (A1)$$

was equated to a finite fourier expansion of the form

$$I(\alpha)= a_o/2 + a_1\cos\alpha' + b_1 \sin\alpha' \quad (A2)$$

where α=analyzer angle and $\alpha'= 2\alpha$.

However, an intermediate form of $I(\alpha)$ was required.

$$I(\alpha)= A^2 \cos^2(\alpha - \theta_o) + B^2 \sin^2(\alpha - \theta_o) \quad (A3)$$

The cross terms in eq. A1 were incorporated into

eq. A3 by including an offset angle θ_o.

Using the trigonometric identity,

$$\sin^2\beta = 1 - \cos^2\beta$$

equation A3 becomes

$$I(\alpha) = (A^2 - B^2)\cos^2(\alpha - \theta_o) + B^2 \qquad (A4)$$

But $\cos^2\beta = \frac{1 + \cos 2\beta}{2}$

Therefore

$$I(\alpha) = \frac{A^2 + B^2}{2} + \frac{A^2 - B^2}{2}\cos 2(\alpha - \theta_o) \qquad (A5)$$

Since $\cos(\alpha - \beta) = \cos\alpha\cos\beta + \sin\alpha\sin\beta$

$$I(\alpha) = \frac{A^2 + B^2}{2} + \frac{A^2 - B^2}{2}\cos 2\alpha \cos 2\theta_o + \frac{A^2 - B^2}{2}\sin 2\alpha \sin 2\theta_o \qquad (A6)$$

Comparing eq. A6 with eq. A2 gives

$$a_1 = \frac{A^2 - B^2}{2}\cos 2\theta_o \quad (A7); \quad b_1 = \frac{A^2 - B^2}{2}\sin 2\theta_o \quad (A8)$$

$$\alpha' = 2\alpha \quad (A9); \quad a_o = A^2 + B^2 \quad (A10)$$

By putting eq. A1 in the same form as eq A2, expressions for $I_p = E_p^2$, $I_s = E_s^2$, and θ_o can be

derived in terms of the experimental parameters a_o, a_1, and b_1 whose exact expressions are given later in this section. Since

$2 \sin \beta \cos \beta = \sin 2\beta$, $\sin^2 \beta = 1 - \cos^2 \beta$, and

$$\cos^2 \beta = \frac{\cos 2\beta + 1}{2}$$

equation A1 becomes

$$I(\alpha) = \frac{E_p^2 - E_s^2}{2} \cos 2\alpha + \frac{E_p^2 + E_s^2}{2} + \mathrm{Re}\,(E_p E_s^* + E_p^* E_s) \frac{\sin 2\alpha}{2} \qquad (A11)$$

Equating eq. A11 to eq. A6 gives

$$E_p^2 + E_s^2 = (A^2 - B^2) \cos 2\theta_o \qquad (A12)$$

and

$$E_p^2 + E_s^2 = A^2 + B^2 \qquad (A13)$$

Substituting eq. A13 into eq. A12 and solving for E_s^2 gives

$$E_s^2 = \frac{A^2 + B^2}{2} - \frac{A^2 - B^2}{2} \cos 2\theta_o = \frac{a_o}{2} - a_1 \qquad (A14)$$

Similarly solving for E_p^2 gives

$$E_p^2 = \frac{A + B}{2} + \frac{A - B}{2} \cos 2 = \frac{a_o}{2} + a_1 \qquad (A15)$$

To solve for θ_o, eq. A8 is divided by eq. A7.

$$\frac{b_1}{a_1} = \frac{\sin 2\theta_o}{\cos 2\theta_o} \qquad (A16)$$

or

$$\theta_o = \frac{1}{2} \tan^{-1} \frac{b}{a} \qquad (A17)$$

The constants a_o, a_1, and b_1 were extracted from the experimental data in the following manner.

Franklin[28] has shown that for a function $I(\alpha)$ of period p, the interval 0,p can be divided into 2r + 1 equal intervals with end points $0 = x_o, x_1, x_2, \ldots, x_{2r} = p$. $I(\alpha)$ can be approximated by a Fourier series of the form

$$I(\alpha) = \frac{a_o}{2} + \sum_{k=1}^{r} a_k \cos k\omega x + \sum_{k=1}^{r} b_k \sin k\omega x \qquad (A18)$$

with $\omega = \frac{2\pi}{p}$

In equation A2, the Fourier series expansion is carried out to k=1 only. The constants a_o, a_1, and b_1 are given by

$$a_o = \frac{1}{r} \sum_{q=0}^{2r-1} I_q \qquad \text{(A19)}$$

$$a_1 = \frac{1}{r} \sum_{q=0}^{2r-1} I_q \cos \omega x_q$$

$$b_1 = \frac{1}{r} \sum_{q=0}^{2r-1} I_q \sin \omega x_q \qquad \text{(A21)}$$

LIST OF REFERENCES

1. T. E. Faber, Introduction to the Theory of Liquid Metals, Cambridge University Press, London, 1972.

2. E. G. Wilson and S. A. Rice, Phys. Rev. 145, 55 (1966).

3. J. Boiani and S. A. Rice, Phys. Rev. 185, 931 (1969).

4. A. N. Bloch and S. A. Rice, Phys. Rev. 185, 933 (1969).

5. E. D. Crozier and E. Murphy, Can. J. Phys. 50, 1914 (1972).

6. D. Guidotti and S. A. Rice, Phys. Rev. B 15, 3796 (1977).

7. O'Schell, Ann. Physik 6, 932 (1930).

8. F. Brown, R. E. Parks, and A. M. Sleeper, Phys. Rev. Lett. 14, 1029 (1965).

9. E. D. Crozier, R. M. Ninnis, and K. E. Rieckhoff, The Properties of Liquid Metals, Proceedings of the Second International Conference, Tokyo (1972). Taylor and Francis, London, 1972.

10. F. Brown and M. Matsuoka, Phys. Rev. 185, 985 (1969).

11. P. D. McCardell, The Effect of the Surface on the Generation of Second Harmonic Light By Silver, Ph.D. Thesis, University of Washington (1972).

12. H. Cheng and P. B. Miller, Phys. Rev. 134, 683 (1964).

13. S. S. Jha, Phys. Rev. 140, 2020 (1965).

14. C. S. Wang, J. M. Chen, and J. R. Bower, Opt. Commun. 8. 275 (1973).

15. J. Rudnick and E. A. Stern, Phys. Rev. B 4, 12, 4274 (1971).

16. W. Koechner, Solid-State Laser Engineering, Springer-Verlag, 1976.

17. W. J. Choyke, S. H. Vosko, and T. W. O'Keefe, Solid State Commun. 9, 361 (1971).

18. N. Bloembergen and P. S. Pershan, Phys. Rev. 128, 606 (1962).

19. R. M. Ninnis, Design and Performance Characteristics of a Modelocked Neodymium-Glass Laser, M.Sc. Thesis, Simon Fraser University (1972).

20. J. A. Fleck Jr., J. Appl. Phys. 39, 7, 3318 (1968).

21. O. Svelto, Principles of Lasers, translated by D. C. Hanna, Plenum Press, New York, 1976.

22. K. H. Drexhage and G. A. Reynolds, Opt. Commun. 10, 1, 18 (1974).

23. R. Harrach and G. Kachen, J. Appl. Phys. 39, 2482 (1968).

24. N. C. Barford, Experimental Measurements: Precision, Error and Truth, Addison-Wesley, London, 1969.

25. F. Reif, Fundamentals of Statistical and Thermal Physics, McGraw-Hill, New York, 1965.

26. D. E. Gray, ed., American Institute of Physics Handbook, 2d ed., McGraw-Hill, 1963.

27. R. A. Buckingham, Numerical Methods, Sir Isacc Pitman and Sons Ltd., 1962.

28. P. Franklin, An Introduction to Fourier Methods and the Laplace Transformation, Dover, New York, 1949.